Insights into Pressure-Temperature Induced Morphology and Mesophase Formation in the Non-Mesogenic Polymer Polyethylene Oxide

By

Tobias Clevinger

B.S., University of Maryland, Baltimore County, 2015

Thesis

Submitted in partial fulfillment of the requirements for the
Degree of Master of Science in Biomedical Engineering at Brown University

PROVIDENCE, RHODE ISLAND

MAY 2020

AUTHORIZATION TO LEND AND REPRODUCE THE THESIS

As the sole author of this thesis, I authorize Brown University to lend it to other institutions for the purpose of scholarly research.

Date 3/31/2021

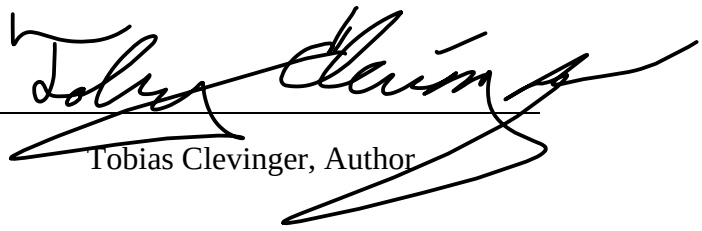

Tobias Clevinger, Author

I further authorize Brown University to reproduce this thesis by photocopying or other means, in total or in part, at the request of other institutions or individuals for the purpose of scholarly research.

Date 3/31/2021

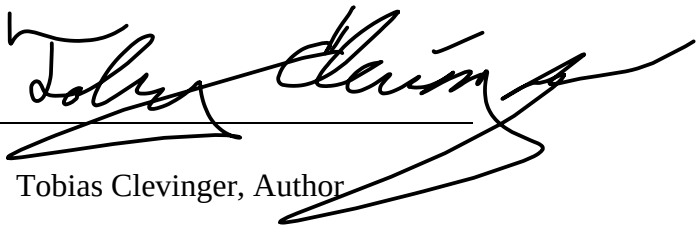

Tobias Clevinger, Author

This thesis by Tobias B. Clevinger is accepted in its present form by the Center of Biomedical Engineering as satisfying the thesis requirement for the degree of Master of Science.

Date 3/26/2021 Signature:

Edith Mathiowitz PhD, Advisor

Recommended to the Graduate Council

Date 3/26/21 Signature:

Dr. Vikas Srivastava, Reader

Date 3/25/21 Signature:

Dr. Marissa Gray, Reader

Approved by the Graduate Council

Date 3/25/21 Signature:

Dr. Marissa Gray, Biomedical Engineering Master's Program Director

Vita

Tobias B. Clevinger

Education

Brown University
Providence, Rhode Island
August 2019 – Present
Program: M.Sc. Biomedical Engineering

University of Maryland, Baltimore County
Baltimore, Maryland
August 2011 – May 2015
Programs: B.S. Chemical, Biochemical, and Environmental Engineering
B.S. Biochemistry and Molecular Biology

Frederick Community College
Frederick, Maryland
August 2010 – May 2011
Program: Supplemental Coursework (High School)

Research

Brown University | Dr. Edith Mathiowitz's Lab
Providence, Rhode Island
September 2019 – Present
- Studying the effects of pressure and temperature on polymer morphology
- Devising and improving methods for manipulating polymer samples

University of Maryland, Baltimore County | Dr. Elsa Garcin's Lab
Baltimore, Maryland
June 2012 – May 2015
- Studied the importance of various genes for protein expression
- Devised and tested a novel blood sugar measurement process using human glucokinase enzyme

Work

Pfizer | Research Co-op Intern
Cambridge, Massachusetts
July 2020 – December 2020
- Quantified and analyzed RNA, DNA, and protein from mouse models
- Investigated potential drug targets for cancer cachexia treatment

AstraZeneca | Quality Analyst
Frederick, Maryland
June 2018 – February 2019
- Collected and tested environmental monitoring and utility samples
- Conducted raw material, in-process, finished product, and stability testing
- Inspected samples for contamination and product quality

Acknowledgements

First, I would like to thank Dr. Edith Mathiowitz for her guidance, suggestions, insights, and moral support during my time in the program. Her expertise in the field of polymer science was essential to my success, and her inquisitive attitude toward data analysis resulted in several epiphanies that led to further developments in my research. I also want to thank her for her positivity and can-do attitude, which helped keep me going during times of stress or uncertainty.

I would next like to thank Cameron Baptista for taking time out of his own work to train and instruct me in the basic principles that would eventually serve as the foundation for this thesis. Without his assistance, much of the data presented here would not exist. Additionally, his prior experience in Brown University's biomedical engineering program was incredibly helpful when navigating the administrative side of my work.

I would also like to thank Sheila Velagapudi for producing some of the raw data I would later analyze in this work. X-ray diffraction analysis is a vital part of polymer analysis, and due to equipment issues I was unable to do such analysis on my own samples. Having similar samples from previous work to analyze helped supplement the analysis of my samples to provide a more in-depth understanding of the phenomena I witnessed in the material.

I would like to thank the entire Mathiowitz lab for their friendship and collaboration during my time at Brown University: Kosta Milovanovic, Aharon Azagury, Stacia Furtado, Carder Jones, Rachael Schmidt, El Hadji Arona Mbaye, Tyler Maxwell, Hyeseon Shin, Raj Sharan, and Anyaa Shah.

I would like to thank the members of my thesis committee, Dr. Marissa Gray and Dr. Vikas Srivastava, for providing key insight and feedback on my thesis material and presentation.

And of course, I would like to thank my friends and family for their support during my time at the program, and especially during the troubling times of the COVID-19 pandemic.

Table of Contents

List of Figures

Appendix Figures

List of Tables

Appendix Tables

Abstract

This work aimed to identify the morphological effects of heat and pressure on high molecular weight (300,000 kDa) polyethylene oxide, with a specific focus on identifying evidence of mesophase formation in the material. Polarized microscopy, differential scanning calorimetry, Fourier-transform infrared spectroscopy, and x-ray diffraction analysis were all performed for this purpose.

Samples processed at 60°C showed a linear relationship between pressing force and the resulting pressure on the samples. Polarized microscopy showed the development of birefringence in samples processed at 60°C and pressures above 1900 psi, as well as in samples that had no pressure applied. Differential scanning calorimetry demonstrated that heat and pressure caused samples to increase in melting and crystallization temperature. Additionally, sample heat of fusion and crystallinity increased proportionally to the pressure applied during treatment. However, the material's glass transition could not be seen, nor any phenomena associated with mesophase formation. Infrared spectroscopy showed several characterizing phenomena between samples: blue shifting and peak broadening of the 1050-1150 cm^{-1} band, peak intensity at 840 cm^{-1}, and peak intensity/ratio at 940 and 960 cm^{-1}. These phenomena varied much more widely in birefringent sample regions than non-birefringent center regions. Finally, x-ray diffraction analysis of samples processed at varying temperatures and high pressures (over 10,000 psi) showed no characteristic evidence of mesophase formation but did show a change in the prevalence of different crystalline planes in the material structure, suggesting that reorientation occurred.

Overall, no evidence of mesophase formation was seen. Evidence instead suggests an increase in crystallinity and a change in crystal orientation.

Introduction

Polymers have taken the world by storm. With their ease of production, wide variety of physical properties, and extensive adaptability, it should come as no surprise that these materials continue to see increasing use in most fields. In fact, polymers are ubiquitous in society, such that listing the industries and sectors that use or rely on polymers would be substantially more difficult than listing those that do not, if any still exist. The biomedical field is no different, with polymers being feverishly researched to produce advancements in biomaterials and medical devices. Polymers have found use as implants, sutures, syringes, catheters, and even as vehicles for drug delivery. In all of these applications, one of the greatest strengths that polymers have are their wide range of mechanical, thermal, and chemical properties, that are determined not only by their composition, but by their manufacturing.

One vital element of studying the properties of a polymer is to study its morphology, as this characteristic is strongly linked to many of the end-use properties the material will exhibit. The effects of manufacturing or processing on a polymer's morphology can be as complicated as they are extensive, which makes it important to consider each element of the process in isolation. Prior work has demonstrated the mesogenic effects of heated compression on several non-mesogenic polymers, as well as shown some of the morphological effects of this procedure on another non-mesogenic polymer, polyethylene oxide. This work aims to further investigate the potential for mesophase induction in this material by broadening the range of pressures applied and utilizing several new analytical approaches.

Polymer Morphology

At the most basic level, polymers are large chains of repeating units, or monomers. The way these long chains are arranged in the material when solid determines their solid phase, either crystal or glass/amorphous. Crystal polymers are highly ordered, densely packed arrangements of the polymer chains, and are commonly seen in a "spherulite" configuration, a radial arrangement of lamellae (Figure 1). [1] Amorphous polymers, on the other hand, are loose jumbles of polymer chain with no order or specific orientation. Polymers can typically be described as crystalline, amorphous, or semi-crystalline, which is a mixture of both. However, relatively few polymers are truly crystalline; most polymers with crystalline characteristics are semi-crystalline. Semi-crystalline polymers undergo both the glass transition and melting events under heat. The glass transition is the gradual change of a polymer's amorphous phase from being a brittle solid to a rubbery fluid, while melting is the relaxation of the crystal phase's ordered configuration into a liquid state. These changes both contribute to a polymer's fluidity under heat.

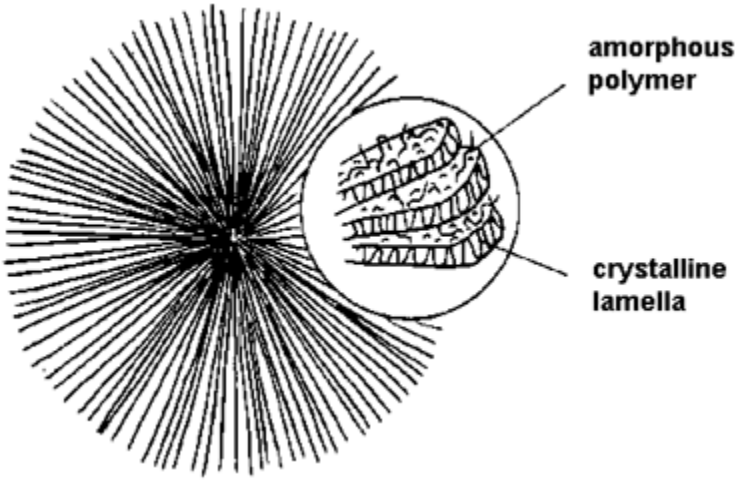

Figure 1. A spherulite formation. Spherulites are comprised of crystalline lamellae linked by amorphous regions in a radial arrangement. [2]

While the chemical composition of a given polymer will determine the temperatures at which glass transition and melting occur, the material's thermal and mechanical history will

determine its solid phase composition. For example, a polymer which slowly cools below its melting point will have plenty of time for the chains to align into a crystalline configuration before solidifying, while a flash-frozen polymer would instead be forced to solidify in its disordered fluid state, resulting in a more amorphous polymer. Interestingly, simply leaving a polymer to rest will also have an effect: semi-crystalline polymers develop more crystallinity over time as the chains slowly orient to achieve their lowest-energy state. [3] Melting the polymer acts as a "reset" for its conformation, effectively rejuvenating the material and allowing it to adopt a new configuration upon solidifying.

In addition to the traditional solid and liquid phases, another set of phases exist: the mesophases. The three commonly accepted mesophases are liquid crystal, plastic crystal, and condis crystal. These phases are hybrid phases between the crystalline and amorphous solid phases. They can be defined by the orientation of their polymer chains relative to the orientations of the crystal and amorphous phases. Crystal polymers have both positional and orientational order, amorphous polymers are entirely disordered, and mesophase polymers have some positional and/or orientational order, acting as a half-measure between the two solid phases. [4]

Mesophase Induction

Mesophases are found in "mesogenic" polymers: polymers with a rigid component in their backbone or attached as a side chain. These rigid groups, or mesogens, include moieties composed of benzene rings or double/triple bonds, but many other compounds and groups can act as mesogens. These groups encourage the polymer chains to orient under certain conditions, such as annealing, giving the phase pseudo-crystalline properties without the orientation expected of crystalline phases. [4]

While mesogenic polymers naturally lend themselves to mesophase formation, non-mesogenic polymers have been discovered to also produce mesophases under certain processing conditions. This has most commonly been done by applying tension or shear stress to the polymers under heat, forcing their chains to align in response to the mechanical force. One famous example of these processes is Kevlar, formed by spinning fibers of poly(p-phenylene terephthalamide). [5] While these processes can engender beneficial properties to the polymers through the mesophase, they also limit the materials' applications to fibers and films. However, this same phenomenon has recently been seen in non-mesogenic polymers using heated compression annealing, which would allow for mesomorphic polymers to be manufactured in a wider variety of forms. [6]

Polyethylene Oxide

Polyethylene oxide (PEO) is a semicrystalline thermoplastic comprised of a repeating monomer of C_2H_4OH, forming a repeating ether backbone with no side chains. At low molecular weights, this polymer is instead referred to as polyethylene glycol. Like many polymers, the glass transition and melting temperatures of PEO are dependent on the average molecular weight of the material. At a molecular weight of 300,000 kDa, the glass transition is -67°C and the melting point is 65°C. [7]

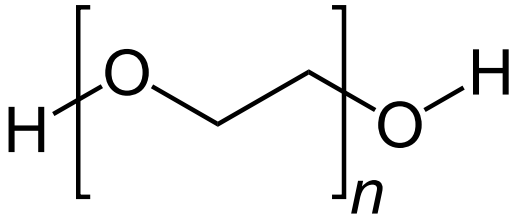

Figure 2. The structure of polyethylene oxide.

PEO has been investigated for use in a wide variety of applications. In biomedicine it has been used as an extended-duration drug delivery vehicle, while in electronics it has shown potential for battery construction. In all of these use-cases, the phase composition of the material is crucial. For drug delivery, phase composition can determine the material's drug release profile, allowing different drugs to have tuned drug delivery vehicles. [8] Meanwhile, the morphology also influences conductivity in the case of battery manufacturing. [9]

Prior Work in the Mathiowitz Lab

The Mathiowitz lab has been investigating the morphological profiles of biomedically suitable polymers for several years, including PLA, PCL, and PEO, with a particular focus on the mesogenic effects of heated compression techniques, as opposed to tension or flow techniques.

Heat and pressure treatment has been demonstrated to generate mesophases in PLA and PCL at temperatures near the melting point and under high pressure. [6] [10] Meanwhile, PEO has been shown to develop birefringence and an elevated degree of crystallinity under similar conditions, which may hint at a potential for mesophase formation in the polymer.

While PLA and PCL have both been analyzed after processing with a wide range of both pressures and temperatures, PEO has thus far only been investigated using variable temperature and fixed pressure. Expanding this data with a range of applied pressures, as well as several new analytical techniques, may prove key to determining mesophase formation.

Motivation

As previously mentioned, polymers are being extensively researched for their utility in various industries and applications, including in the biomedical field. A key element of this utility lies in the material's morphological response to manufacturing processes. Better understanding these responses in PEO could open new avenues or research or application in the future.

In addition to better understanding the polymer's morphology, it would also be helpful to better understand the effects of compression on PEO's ability to potentially form a mesophase. Non-mesogenic polymers are traditionally formed into a mesophase via tension or flow processing methods, which limits their utility to materials composed of fibers and films. A consistent, effective method for generating a mesophase on bulk polymers would prove highly beneficial for applications that could benefit from them, such as drug delivery.

Background

Hydraulic Press

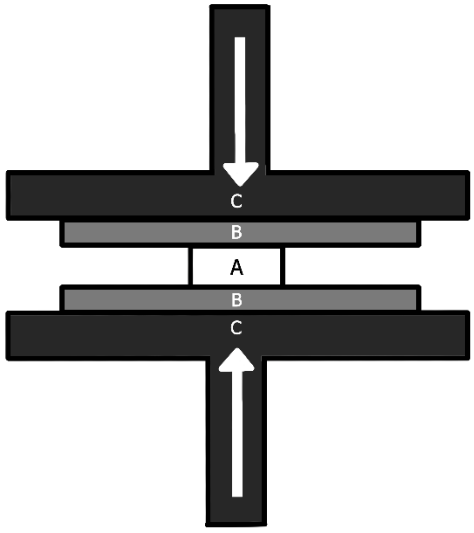

Figure 3. A scheme depicting the compression technique used in this work. A) The sample itself. B) The plates used to move and process samples in the press. C) The heated press blocks, capable of heating and cooling the plates and sample.

A hydraulic press is a device that uses the power of hydraulics to generate large amounts of force, specifically for the purpose of applying pressure to objects. These machines are commonly used to process materials that would otherwise be too resilient to process. For example, hydraulic presses can be used in forging metals, shaping metal and polymer parts, or punching.

The press used in this study was also capable of applying heat and maintaining temperatures, as well as quenching whatever is being pressed through heat exchange with cold water. This allowed for samples to not only be pressed with large amounts of force, but pressed at various temperatures, as well.

Polarized Light Microscopy

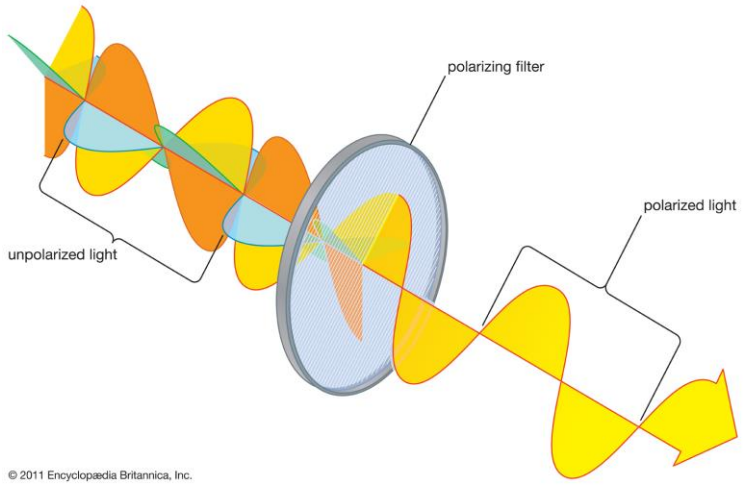

Figure 4. Visual representation of polarized light. [11]

Under almost all normal circumstances, the light that enters a person's eye or a machine's sensor will be coming from many directions, due to the sheer quantity of photons and the chaotic nature of photon emission and reflection. However, some materials are capable of blocking light based on its direction, such that only light travelling upon a specific plane can pass. These materials act as filters that "polarize" the light. By polarizing light twice with perpendicular filters, no light can emerge from the second filter. This is referred to as "extinction".

Normally with two perpendicular filters, no light would be visible through them due to this extinction. However, some materials, like polymers, can also affect the direction light travels. Placing these materials between cross-polarized filters can cause light to successfully travel through, resulting in the materials being visible. For example, crystalline polymers will cause light to rotate as it travels through them due to refraction, allowing some of the light to successfully cross the second filter, which gives the material a bright white appearance.

Crystalline polymers also have anisotropic optical properties, meaning that light will travel through them differently depending on which direction they are going. This can result in what is called "birefringence": if the light gets rotated enough times as it crosses the material, it will

separate similarly to the rainbow made by a prism. Some of this multicolored light then passes through the second filter and can be seen, denoting a high crystal content. Birefringence can also act as an indicator for the formation of a mesophase in the material, as well as for mechanical stress or strain. [10] An example of birefringence is shown in Figure 5 below. By viewing samples under polarized light at high magnification, various crystal formations and optical properties can be investigated.

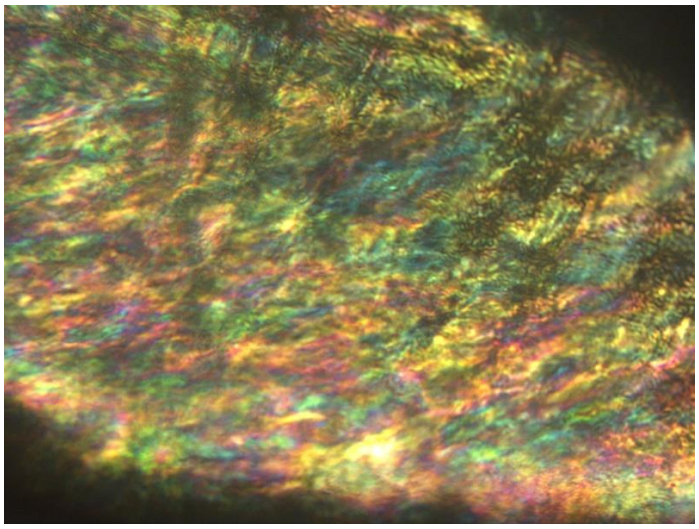

Figure 5. Example of birefringence under polarized light. Sample was untreated polyethylene oxide at 100X magnification.

Differential Scanning Calorimetry (DSC)

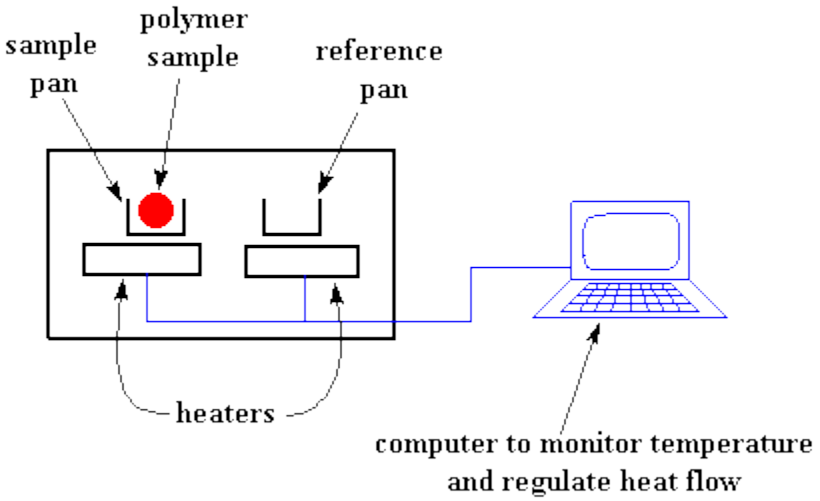

Figure 6. Basic scheme for DSC. [12]

Materials require energy in the form of heat to raise in temperature, as well as to change to a higher-energy phase. Inversely, materials must lose energy to lower in temperature and revert to lower-energy phases. Differential scanning calorimeters quantify this process by heating up and cooling down samples while tracking the heat required to do so. In this way, the thermal properties of a material can be viewed as a function of temperature.

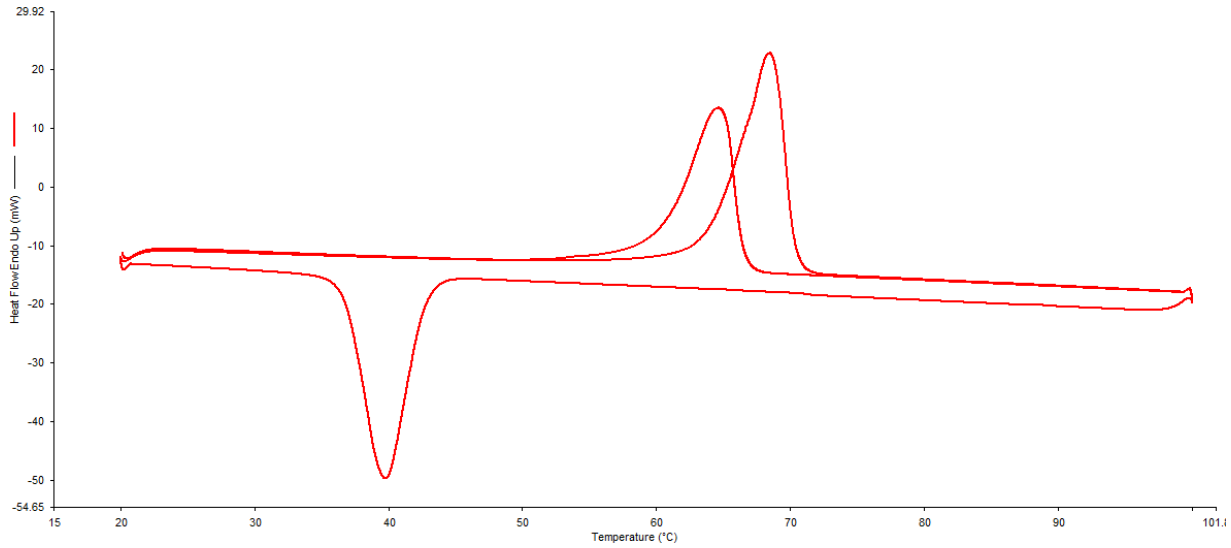

Figure 7. Example DSC result for a sample processed at 60°C and 1924 psi, showing two heating curves and one cooling curve. Note the change in heating curve characteristics between melts.

Figure 7 shows a typical DSC test result for two heating curves and one cooling curve: the material was heated to above its melting point (one "melt"), then cooled to below the crystallization point (one "cooling"), and then finally heated to above melting again. The straight lines represent the material being heated or cooled based on its heat capacity (a perfectly calibrated DSC would have a completely flat line, denoting a constant heat capacity), while the large bumps or peaks denote the material melting. The area of a given peak can be calculated and represents the material's heat of fusion under those conditions, while the exact temperature of the peak is the material's melting point.

Polymers are highly adaptive materials that can adopt various configurations based on their conditions. For example, as polymers age, they slowly crystallize, even without external stimuli. This crystallization results in a higher melting temperature and a greater heat of fusion, as demonstrated by Figure 7: the right-hand melting peak was the material's first melt, while the smaller, left-hand peak was the material's second melt. Because the material had been freshly melted and re-solidified, it had a lower crystal content. The second melt's properties can change depending on how the DSC cools the polymer. Slower cooling typically results in more crystal content, while faster cooling prevents crystallization and creates a more amorphous polymer.

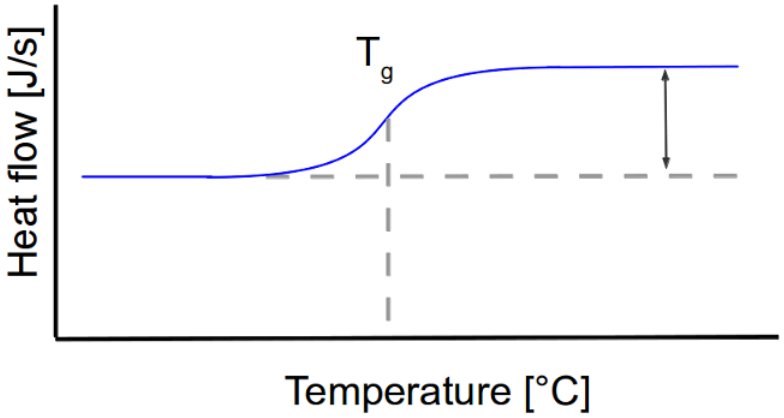

Figure 8. An example of a material undergoing glass transition, as seen in DSC results. T_g is the glass transition temperature. [13]

Figure 8 shows a material that undergoes a glass transition. Polymers with a high amorphous content will show a significant change in heat capacity as they undergo this transition, characterized by an s-curve.

Examining the curves of a polymer undergoing DSC can reveal many facets of the material's structure, including crystal content and the potential existence of a mesophase.

Fourier-Transform Infrared Spectroscopy

Molecular compounds are composed of bonds between atoms, and these bonds have characteristic vibrational frequencies. When exposed to infrared light, many of these bonds will absorb the light at their specific frequency, resulting in less light exiting the sample than entering. FTIR takes advantage of this principle by shining infrared light through a sample and measuring how much light is absorbed at each wavelength. This absorption data can then be used to generate a unique spectrum of peaks and bands for the sample. The location, shape, and intensity of a spectrum's peaks reveals the nature of the material's chemical structure.

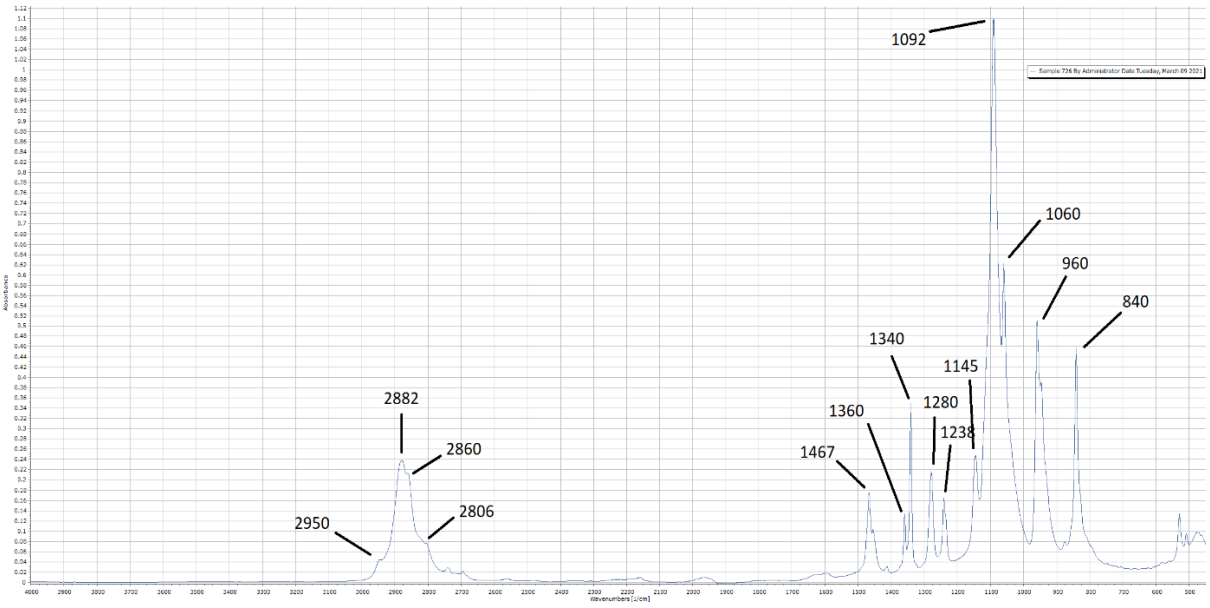

Figure 9. Example FTIR spectrum, using the center of a sample processed at 60°C and 9779 psi. Peak wavenumbers are marked.

The spectrum shown in Figure 9 measures the absorbance of the material at different "wavenumbers". Higher absorbance means that the material absorbed more of the incoming infrared light at that wavenumber, which indicates the existence and prevalence of a bond with that characteristic frequency. The wavenumber represents a given infrared wavelength's spatial frequency and is typically measured in cm^{-1}.

Interpretation of FTIR spectra requires other analytical methods to confirm findings. For example, nothing about a peak at 2800 cm^{-1} can inform an analyst that that peak is specifically for an alkyl C-H stretching bond. Rather, once that peak has been confirmed to correspond to that bond using other methods, future work can make the assumption that this is still true when measuring new materials. This is commonly done in FTIR using "peak tables", which provide many common FTIR peaks and the bonds they correspond to.

For this work, an FTIR method called "Attenuated Total Reflection" (ATR) was used. In FTIR-ATR, the infrared beam is passed through a crystal with a high refractive index before hitting the sample at an angle. The beam should then reflect off the sample and back into the crystal, where it either reflects off a backing material to repeat the process or exits the crystal for measurement. This process only works if the crystal has a higher refractive index than the sample; otherwise, the infrared beam will enter the sample, reducing the amount of light that can be measured.

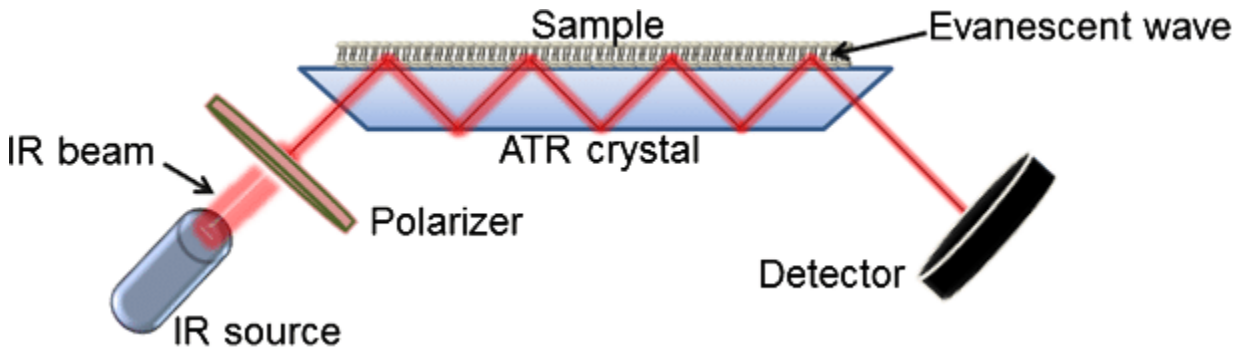

Figure 10. Scheme of FTIR-ATR. [14]

X-Ray Diffraction

When x-rays hit materials, they can be scattered by the electrons surrounding the material's atoms. When a material is crystalline, its atoms are ordered in such a way that they have specific arrangements, which form crystal faces. These faces will scatter x-rays in a consistent pattern that, after accounting for destructive and constructive interference between the scattered waves, form strong waves at specific angles to the material, and no waves anywhere else. Meanwhile, disordered materials, such as liquids or amorphous polymers, will scatter x-rays in an irregular pattern, resulting in weaker waves propagating in many directions.

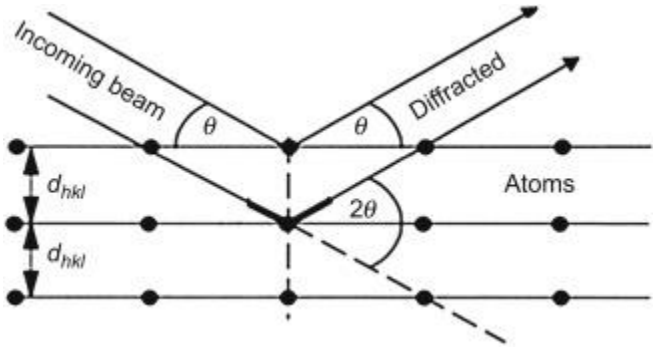

Figure 11. Scheme of x-ray diffraction by crystalline atoms. [15]

In XRD, a material is exposed to x-rays and the angles of the resulting scattered waves are recorded as a function of the angles at which they propagate, resulting in a spectrum of peaks that correspond with the sample's conformation. A crystalline sample would produce several thin, tall peaks, while an amorphous sample would produce a wide, low peak. The spectrum can then be "deconvoluted" for analysis. Deconvolution is the breaking down of a spectrum's shape into its individual component peaks. This process requires an assumption that these component peaks of a sample will conform to a given shape; most commonly, the peaks are assumed to be gaussian.

This technique is a powerful tool for determining the phase composition of polymers. By deconvoluting a sample's XRD spectrum, the relative amounts of crystal and amorphous regions

can be calculated based on the amounts of thin crystal peaks and wide amorphous peaks in the deconvolution. Additionally, the presence of peaks too wide for crystals and too thin for amorphous regions could be evidence for the development of a mesophase, as these phases have less order than crystals but more order than amorphous regions.

Specific Aims

The goal of this work was to establish the significance of pressure on the morphological changes induced in PEO by heat and pressure treatment, as well as to characterize these changes. To do so, samples were treated at one temperature but a range of pressures.

In addition to general characterization, this work also attempted to identify evidence of mesophase formation in the non-mesogenic PEO material.

Materials and Methods

Materials

The primary material of interest was polyethylene oxide. A polyethylene oxide powder with an average molecular weight of 300,000 kDa, originally purchased from Sigma Aldrich, was used for this investigation. This material has a reported melting temperature of 65°C and a reported glass transition temperature of -67°C. [16] [7]

In constructing the tray used to produce PEO pellets for processing, two materials were used. Firstly, the mold used to produce the tray was 3D printed using AMZ3D brand PLA. Secondly, the tray itself was cast using Smooth-On brand Platinum Silicone.

Methods

Tray Production via Casting

In order to produce pellets of PEO that could be worked, a silicone tray was created. This tray was made by first 3D printing a mold for the cups of the tray. Then, the mold was suspended over an empty petri dish. The dish was then filled with Smooth-On brand Platinum Silicone and left to set. The resulting tray was then left in a Cole Parmer StableTemp oven at a high temperature (>100°C) to evaporate any volatile compounds, such as un-reacted silicone monomers, left in the tray. This prevented the PEO from being contaminated by other compounds during pellet production.

The resulting tray had seven cups that were each 15 mm in diameter and 6 mm deep.

Pellet Production via Oven Melting

PEO powder was formed into pellets by melting in a Cole Parmer StableTemp oven. 350 mg of 300,000 MW PEO were placed in each cup of the silicone tray and left in the oven at 75 - 90°C for 1 hour. The tray was then left to cool at room temperature. It was important that the pellets always cool at the same temperature to avoid inconsistent phase compositions between samples, as the cooling rate can affect the crystallinity. Once cooled, the resulting pellets were removed and stored for future work.

Hydraulic Press

When pressing samples, a Carver Auto Series NE hydraulic press was used. Samples were pressed between heated plates with varying amounts of force, between 1,000 lb_f and 15,000 lb_f, using the following protocol:

1. Press heated to 60°C
2. Sample placed between plates of press
3. Press closed until both plates made good contact with sample
4. Waited 10 minutes for sample to reach 60°C
5. Press closed with prescribed force for 15 minutes
6. Press cooled to room temperature through heat exchange with water
7. Press opened, relieving pressure on sample
8. Sample removed from press

The time and temperature were chosen due to prior work in the lab establishing 15 minutes and 62°C as optimal parameters for inducing the desired morphological changes, such as birefringence and crystallization. 60°C was chosen instead of 62°C due to concerns with the press

overshooting its setpoint temperature by several degrees. Reaching the melting point was not desired for this procedure, so the operating temperature was reduced slightly to compensate.

Optical Polarized Microscopy

Samples were imaged after pressing using polarized light at varying magnifications. For visual inspections with the naked eye, samples were sandwiched between a pair of polarized sheets, oriented for light extinction, and placed over a bright light. For magnified viewing, a Laxco SeBa Pro4B Series Digital Microscope was used, with samples placed flat on a glass microscope slide. Due to their size, unprocessed PEO pellets had to be cross sectioned for microscope viewing.

Differential Scanning Calorimetry

Calorimetry was performed using a Perkin Elmer DSC 8500. 5 mg of each sample were removed and placed in an aluminum pan and crimp-sealed before placement in the machine. Samples were analyzed following the provided protocol:

1. Sample placed in machine at room temperature
2. Temperature reduced to -75°C
3. Temperature held at -75 C for 1 minute
4. Temperature raised to 100 C at 10°C/min
5. Temperature held at 100 C for 1 minute
6. Temperature reduced to -75 C at 10°C/min
7. Temperature held at -75 C for 1 minute
8. Temperature raised to 100 C at 10°C/min

Once the protocol was completed, the sample was disposed of and analysis of the DSC curve was performed.

In some cases, different lower temperatures were used for the DSC procedure. In those cases, the lower temperature would be higher: for example, 20 C instead of -75 C. These temperatures were chosen for different logistical reasons. -75 C was chosen to investigate the glass transition of the material, while 20 C was chosen for expedient results when the glass transition was not being considered.

Fourier-Transform Infrared Spectroscopy (FTIR)

For FTIR analysis, a Perkin Elmer Spectrum Two was used. A Universal Attenuated Total Reflectance Accessory was attached to the machine to allow for Attenuated Total Reflectance (ATR) FTIR analysis.

Samples were placed on the ATR plate with the region of interest over the crystal. The samples were then pressed by the pressure arm until the machine displayed an applied force of 100-110 units before scanning. A background scan was performed beforehand every day the samples were to be scanned, to ensure accurate background readings.

The resulting spectra obtained from these scans were then analyzed using Spectragryph, a free software for academic use. [17]

X-Ray Diffraction Deconvolution

XRD data was obtained for separate samples of 300,000 kDa PEO by Sheila Velagapudi in 2020. These samples were processed using the same “Hydraulic Press” method listed earlier in this section, with an operating force of 20,000 lb_f and a temperature of 62°C. XRD was performed using a Bruker D-8 Advance X-Ray Diffraction System. The machine’s copper x-ray tube was set to 40 kV and 40 mA for this procedure.

The resulting XRD spectra were then analyzed via deconvolution using Fityk, a free software program. XRD files were first converted from the ".raw" filetype to the ".xy" filetype, and then converted again to the ".txt" filetype, using PowDLL Converter, another free software. Once files were readable in Fityk, the XRD spectra for the samples were broken down into a series of discrete gaussian peaks for analysis by hand.

Results and Discussion

Processing Force and Pressure Relationship

When malleable materials are pressed, they change shape in response. In the case of the pellets produced for this work, they spread out into a thin film. As the material spread out, it increased in surface area. Meanwhile, the press slowly increased in force until the prescribed amount for that sample (for example, 2,000 lb_f). Once the press had reached this force, and once the film had stopped spreading out in response to that force, an equilibrium was reached. At this point, a stable pressure was being exerted on the material. Since materials are affected by pressure rather than absolute force, it was important to understand the relationship between the force exerted by the press and the pressure experienced by the samples. Table 1 shows the calculated pressures exerted on each sample during processing, using the final dimensions of the film produced at that force.

Table 1. Conversion table for samples processed at various absolute force values, to determine the exerted pressure.

Force (lb_f)	Surface Area (in^2)	Pressure (psi)
0	0.26934	0
1000	0.83816	1193.09
2000	1.03963	1923.76
5000	1.36498	3663.06
10000	1.24172	8053.35
15000	1.53388	9779.12

These calculated pressure values were then compared to the forces applied during processing, as shown in Figure 12. Samples showed a linear relationship between applied force and resulting pressure values, indicating that increasing the processing force on the material has a consistent mechanical effect on the resulting films.

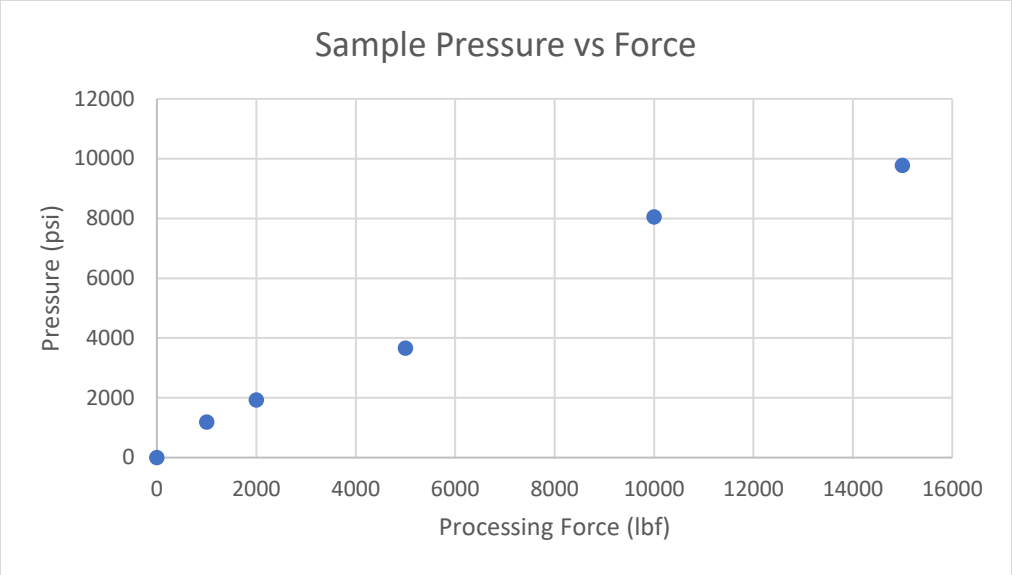

Figure 12. Comparison of processing forces used on samples and the resulting pressure exerted at equilibrium.

Polarized Microscopy

It was previously established that processing high molecular weight PEO at high pressures and temperatures near the melting point could induce spherulite formation and increased birefringence in the material. In order to determine the effect of processing pressure on these phenomena, images were taken of the samples at high magnification through polarized light.

When viewed through polarized light without magnification, birefringence was noted in all samples except for those processed at 1,000 lb_f, equivalent to 1193 psi. Table 2 shows representative images of each type of sample produced.

Table 2. Polarized images of PEO samples. Images not to scale. Note the development of a cross pattern in the birefringence as pressure increases. Birefringence was seen in all samples processed at or above 1924 psi, even if not visible in these images.

Unprocessed	1193 psi	1924 psi
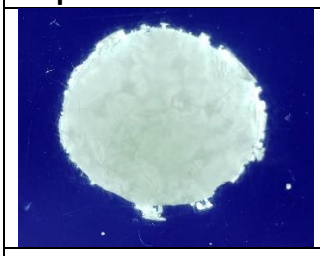		
3663 psi	**8053 psi**	**9779 psi**
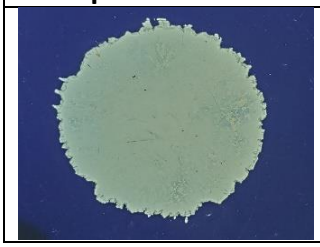	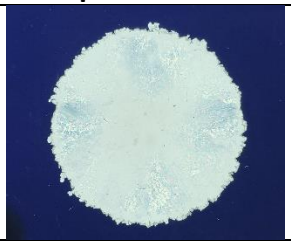	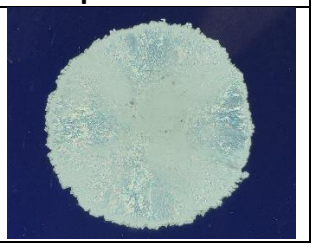

These birefringent sections were primarily found toward the edges of the samples, arranged in a cross or four-leaf-clover shape. Curiously, this pattern is reminiscent of an established optical pattern in spherulites, known as a “Maltese Cross Pattern”. To better visualize this birefringence, and to inspect spherulite density in the samples, a polarized microscope was used to inspect both the non-birefringent centers of the samples and the birefringent edges.

Table 3. 40X polarized magnification of representative center and edge sections of samples at varying pressures.

Pressure (psi)	Center	Edge
1193		
1924	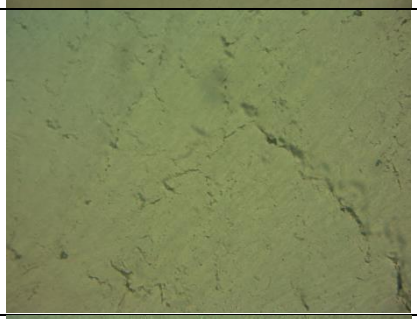	
3663		
8053	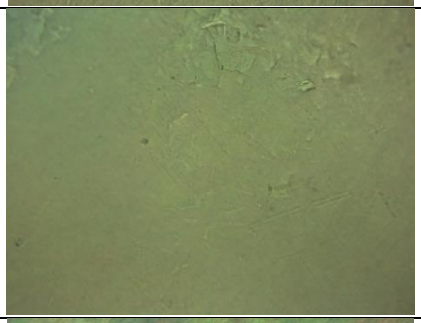	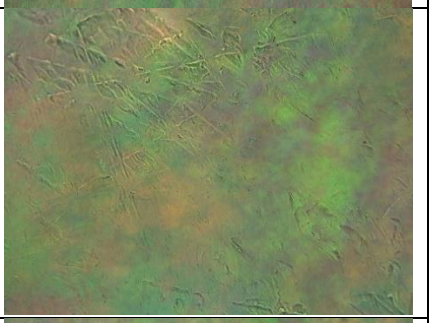
9779	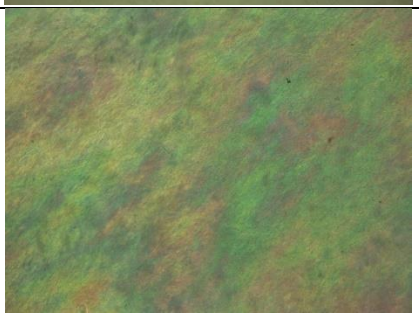	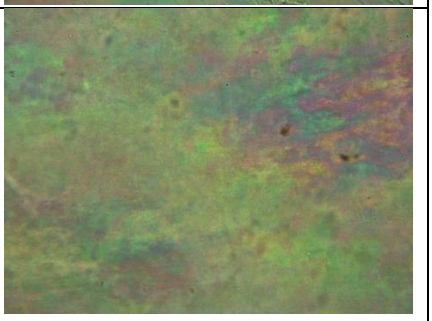

Table 3 shows the magnified images taken of these sections of the samples. Amorphous regions of PEO present as dark sections due to light extinction, while crystalline regions allow all colors of light through, resulting in a basic white color. The rainbow coloration is the result of birefringence in the sample. Interestingly, while none of the samples demonstrated birefringence at the center of the film with the naked eye, 40X magnification revealed significant birefringence in the center of samples processed at 9779 psi, suggesting that the higher pressure may even induce morphological changes in the thicker sections of the films.

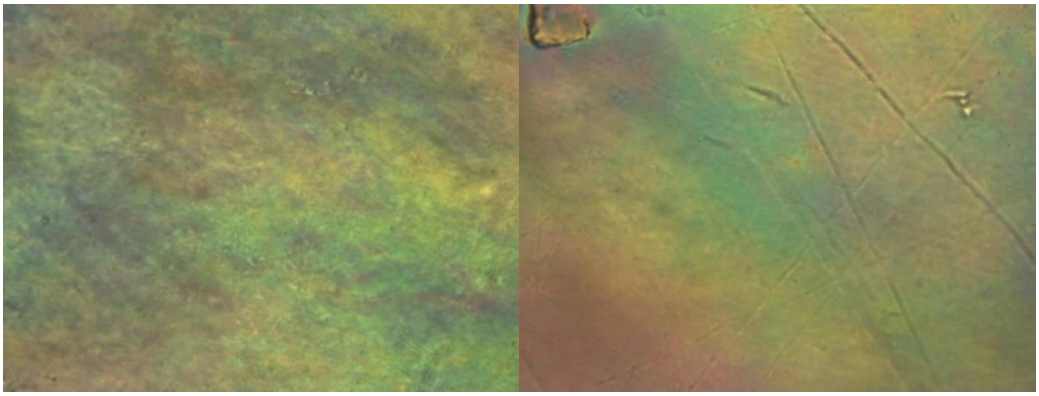

Figure 13. 100X polarized magnification of 9779 psi samples. Center (left) and edge (right).

Despite the clear presence of birefringence, no spherulites were visible under magnification, even at 100X magnification (Figure 13). This may be due to the thickness of the films; large amounts of birefringence caused by crystals below the focal point could be masking the individual crystals at the focal point. Spherulites are a well-documented feature of annealed PEO and are typically seen in tandem with birefringence. [18]

To compare these processed samples to unprocessed PEO, a vertical cross-section of one of the unused PEO pellets was taken and imaged (Figure 14).

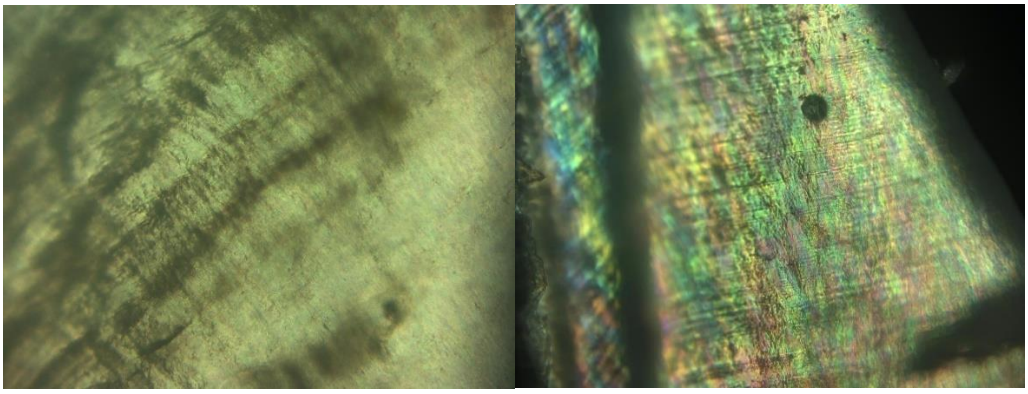

Figure 14. 40X polarized magnification of a vertical cross-section of unprocessed PEO. Center (left) and edge (right).

While the center of the cross-section in Figure 14 shows the expected semi-crystalline structure (as seen in the alternating white and black banding), the edge of the cross-section also demonstrates birefringence, similarly to the processed samples. Additionally, Figure 15 shows polarized microscope images of a flake of PEO. This flake was gently removed from the edge of an unprocessed PEO pellet and shows bright birefringent coloration.

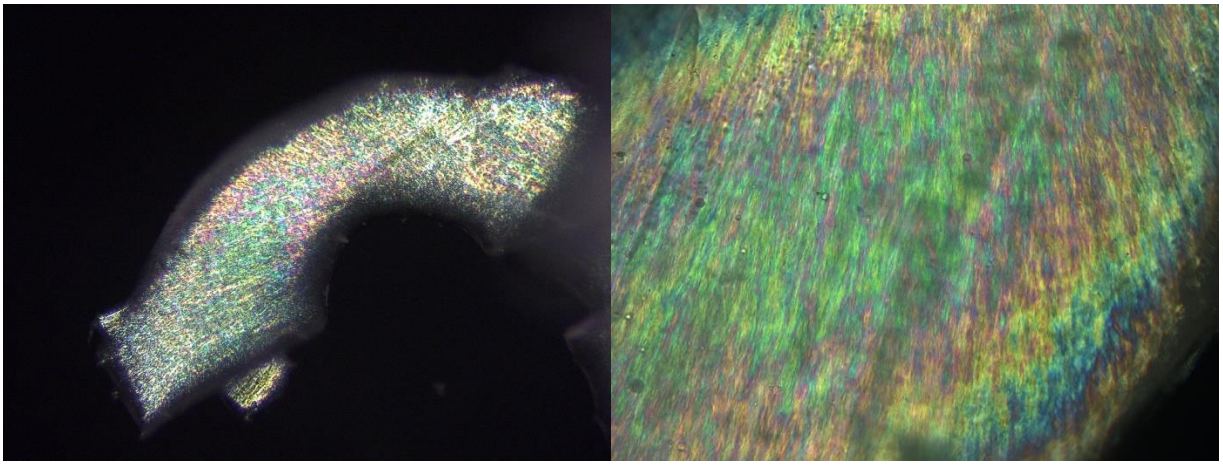

Figure 15. Polarized microscope images of flakes of unprocessed PEO material. 10X magnification (left) and 40X magnification (right).

Overall, these images confirm that the heat- and pressure-based compression process for inducing anisotropic birefringence in high molecular weight PEO still produces birefringent samples at significantly lower pressures than previously investigated. However, the absence of birefringence from the 1193 psi-processed samples when even unprocessed PEO has clear

birefringence raises questions about the interaction between pressure and morphology in the polymer.

Differential Scanning Calorimetry

Melting and Crystallization Temperatures

The temperatures at which the processed samples melt, cool, and undergo glass transition, in addition to the heats of melting and cooling, could help better characterize the samples and determine the impact of pressure on the resulting films.

Table 4. The melting and crystallization temperatures of the unprocessed and processed samples.

Sample (lb_f)	First Melt (°C)	Second Melt (°C)	Crystallization (°C)
0	66.96	64.46	38.26
1000	69.41	65.2	40.11
2000	68.46	64.61	39.79
5000	69.59	64.74	39.17
10000	70.75	65.7	40.38
15000	69.23	64.82	40.35

As outlined in Table 4 and visualized in Figure 16, the melting point of the processed samples shows a clear increase of a few degrees Celsius compared to the unprocessed samples. This elevation in melting point can sometimes be an indicator of increased crystalline content in a polymer. [19] This difference in melting temperature ceases after the first melt of the calorimetry procedure. Since all samples melted and were then cooled at the same rate (10°C/min), they then underwent the same morphological changes, resulting in the samples having similar morphologies. As a result, the second melting point for the samples is the same, hovering around 65°C. Since all samples experienced identical conditions aside from heat and pressure treatment, the initial change in melting point must be a result of this processing. It is interesting to note that a similar change occurs in the crystallization temperature (Figure 17). This shift is slightly lower in magnitude than the first melt shift, but is equally consistent. Additionally, the second melting temperature is

equivalent between unprocessed and processed samples, which confirms that rejuvenation took place. Since crystallization happens post-rejuvenation, it is unclear why the material would still display a temperature shift at that point in its thermal history.

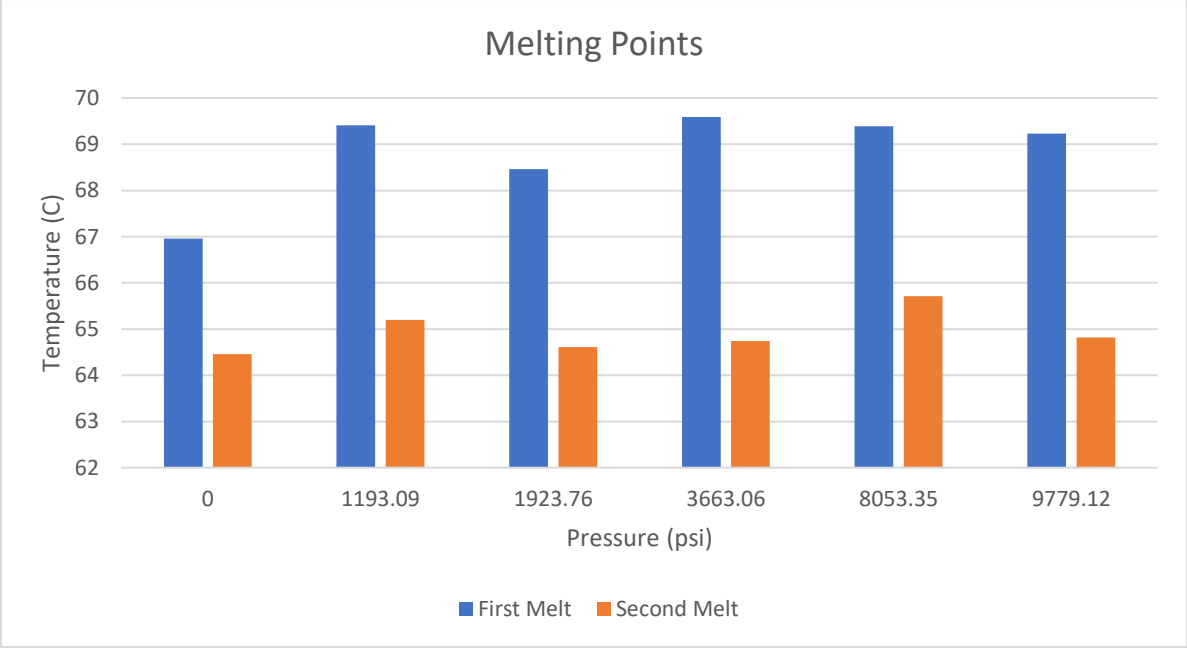

Figure 16. Melting points of samples by pressure. Blue bars represent the first melting, orange bars the second.

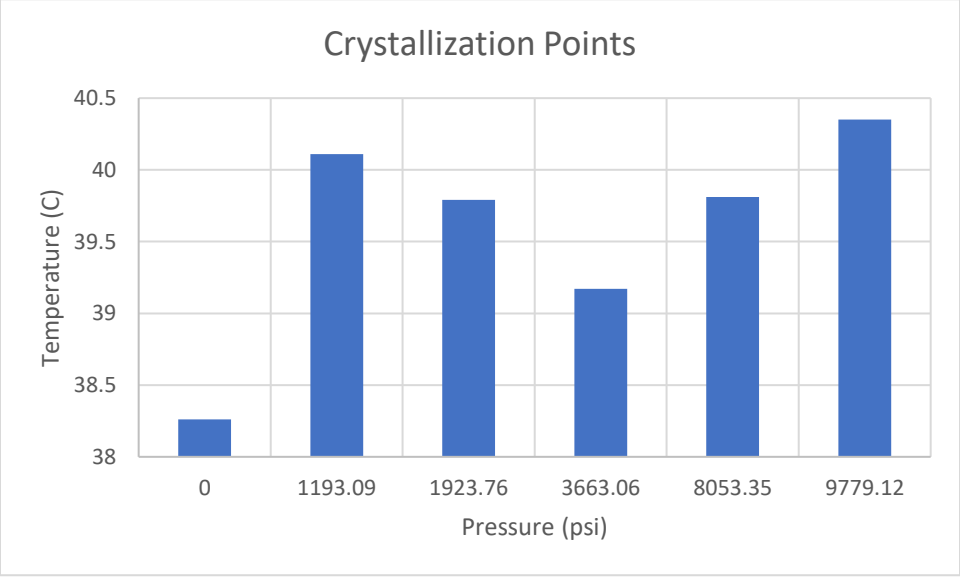

Figure 17. Crystallization temperatures of the samples.

Melting and Crystallization Enthalpies

Table 5. Enthalpies of melting and crystallization in the samples.

Pressure (psi)	First Melt ΔH (J/g)	Second Melt ΔH (J/g)	Crystallization ΔH (-J/g)
0	175.0543	157.3868	148.4075
1193	184.2173	153.3253	150.5828
1924	181.1657	147.3338	151.0021
3663	183.3616	147.933	146.0526
8053	186.3231	158.0216	150.8146
9779	189.2385	159.2195	150.6224

Table 5 shows the calculated enthalpies for each of the transitions seen under DSC. As previously noted with first melting temperatures, there is an upward shift in melting enthalpy between unprocessed and processed samples that does not carry over to the second melting. A higher melting enthalpy (or "heat of fusion") typically indicates a higher crystal content in polymers. [20] As visualized by Figure 18, this first melt enthalpy increases with increasing pressure, suggesting a relationship between processing pressure and crystallinity, with higher pressure resulting in more crystallinity. Enthalpy values for the second melt and crystallization do not display any sort of trend in response to changing pressure. This can be explained by the melting and cooling process the material undergoes in the calorimeter. Since all samples followed the same melting and cooling protocol, they all melted and cooled identically, which resulted in the samples all having the same morphology post-melt.

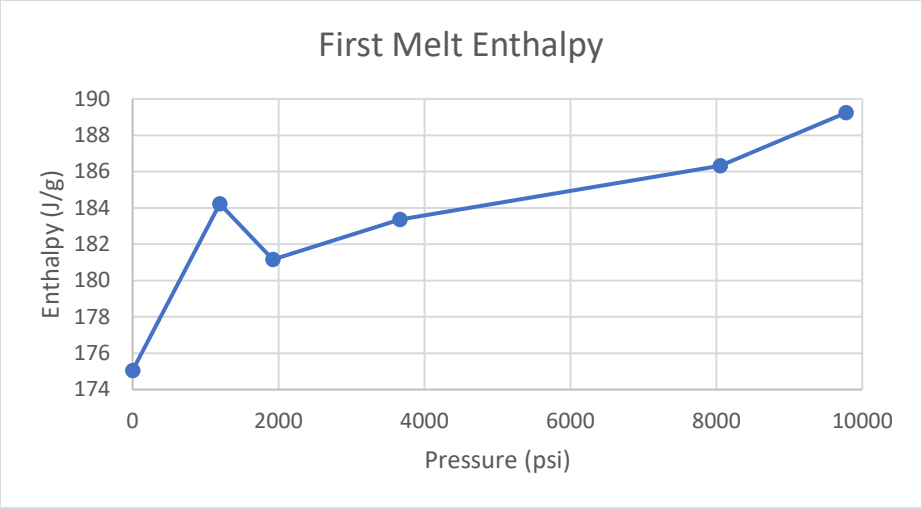

Figure 18. First melting enthalpy of each sample. Note the upward trend with increasing pressure.

Degree of Crystallinity via Heat of Fusion

One way to consider the change in morphology of the material is by considering the degree of crystallinity (DOC) of the samples. To accomplish this, there is a simple equation that can be used to calculate a material's crystallinity using the heat of fusion:

$$DOC = 100 \times \frac{\Delta H_f}{\Delta H_f^c}$$

For equation (1), DOC is the degree of crystallinity, ΔH_f is the heat of fusion of the sample, and ΔH_f^c is the heat of fusion of a 100% crystalline sample of the material. [20] Using a reference value of 216 J/g, each sample's crystallinity could be calculated. [21]

Table 6. Crystallinity of samples as calculated using the heat of fusion.

Pressure (psi)	First Melt DOC	Second Melt DOC
0	81.04366	72.86426
1193	85.28579	70.98394
1924	83.87301	68.21009
3663	84.88963	68.4875
8053	83.33282	69.78782
9779	87.61042	73.71273

The resulting crystallinities are shown in Table 6. Following the trend established by the melting points and melting enthalpies, the processed samples show a clear increase in crystallinity over the unprocessed samples.

In considering these metrics (melting temperature, melting enthalpy, and crystallinity) to determine a change brought about through processing, only the melting enthalpy shows a trend with increasing pressure. While a change always occurs when the samples are processed, the specific importance of pressure is not clearly demonstrated.

Glass Transition

The reported glass transition temperature of 300,000 kDa PEO is -67°C. [7] Since the DSC used for these tests is reported as capable of reaching -80°C, several samples were tested at low temperatures to analyze this transition in unprocessed and processed samples. However, there were complications. For example, the DSC was only able to cool down to about -75°C at the coldest, and only after a significant amount of time. Still, this was potentially cold enough to demonstrate the glass transition. Figure 19 shows an example DSC test run using a sample processed at 9779 psi, through a temperature range of -75°C to 100°C.

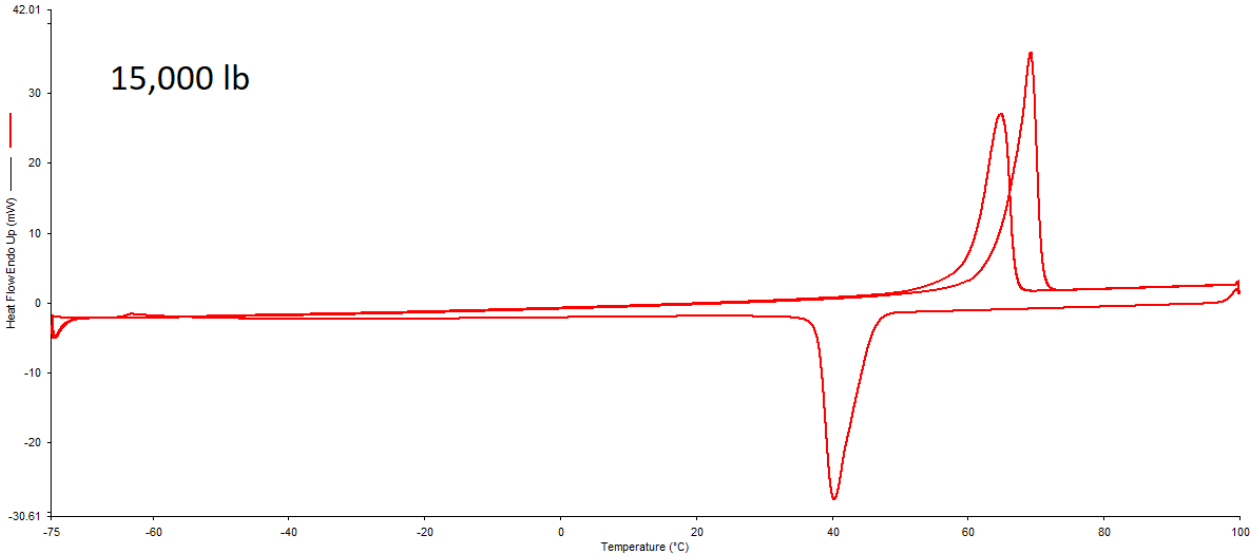

Figure 19. DSC run of a 9779 psi sample, scanned from -75°C to 100°C.

The looping shape seen at -75°C is expected as part of how the machine operates. A variant of this is also visible at the upper end of the range, near 100°C. This means that the first few degrees of any DSC run are not usable for analysis, and the upper bound has the same limitation. However, even after accounting for this, the glass transition was expected to be visible. The glass transition of a material as seen through DSC tends to adopt an S-shape, as previously shown in Figure 8. This curve denotes a smooth step increase in the polymer's heat capacity. [22]

While that was the expectation, Figure 20 displays the actual DSC result near the glass transition temperature for these samples:

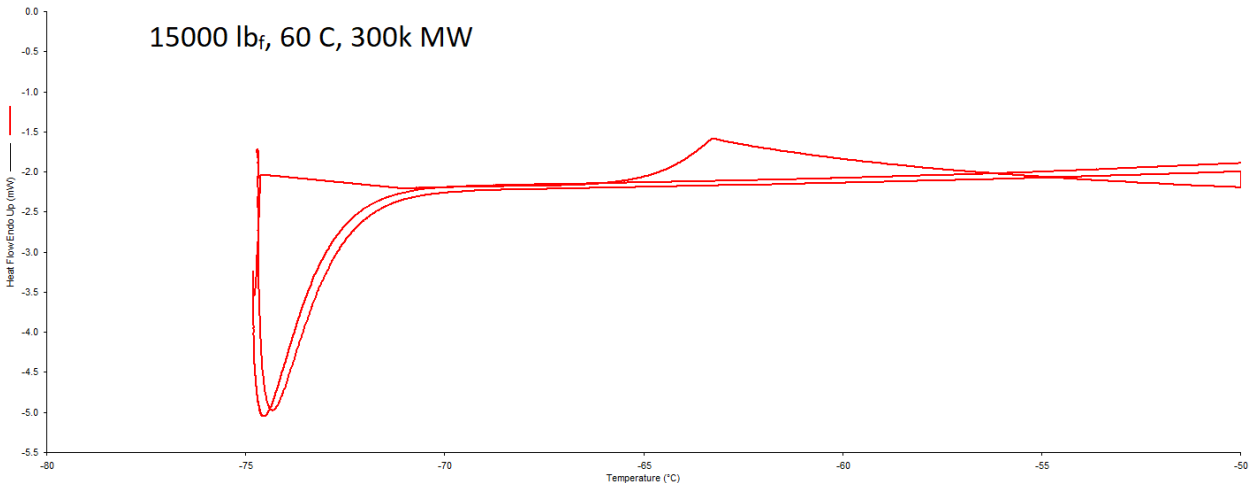

Figure 20. The cold end of the DSC test shown in Figure 19. Note a) the lack of two s-shaped curves on the heating curves, and b) the presence of a sharp spike near -63°C on the cooling curve.

Instead of a characteristic s-shape, both heating curves in this example show a smooth, gentle upward slope that extends across the whole range. This is typically seen in samples that heat up with no change in form, which is not what was expected here. Additionally, there was another unexpected result from these DSC tests: a sharp spike was observed in the cooling curve of the sample. This spike does not conform with any of the phenomena expected from these samples. The sharpness of the spike is reminiscent of sudden changes in heating or cooling when running the machine outside of protocol; for instance, when setting the machine to a certain temperature before initiating a protocol. Combined with the previously mentioned difficulty in cooling the machine below -60°C, it is possible that this phenomenon is the result of the machine attempting to cool the sample faster than it can at those low temperatures.

Table 7. Temperatures at which the unexpected cooling spike appears during the samples' cooling curve.

Pressure (psi)	Cooling Spike Temperature (°C)
0	-63.37
8053	-60.96
9779	-63.25

To see if this spike may be related to a physical property of the material, each DSC test performed at -75°C was compared, with calculated peak temperatures presented in Table 7. These peaks appear at around -63°C, and no pattern could be determined.

To determine if the cooling rate of the DSC may be responsible for this phenomenon, an equivalent sample of 9779 psi PEO was examined following an identical DSC protocol, with one change: instead of cooling the sample at 10°C/min, the calorimeter cooled the sample at 1°C/min. Figure 21 shows the resulting DSC graph, and Figure 22 shows a close-up of the cold range of that graph. These figures clearly show that cooling the sample at a slower rate results in no spike appearing. While the cooling rate for semicrystalline polymers does influence the resulting crystallinity, the material's glass transition would still occur and have a measurable impact on heat capacity. Since changing the cooling rate removes the cooling spike completely, it can most likely be concluded that this phenomenon was due to the calorimeter's cooling system, and not a structural or thermal property of the material.

Regardless of the origin of the unexpected cooling spike, these samples still showed no trace of the expected glass transition. This may have been a result of the high crystallinity; the glass transition is a property of amorphous polymers specifically, and between the polarized microscopy and DSC results, little amorphous polymer can be seen in these samples. However, even polymers with high crystallinity should show a weak glass transition rather than none at all, making these results curious.

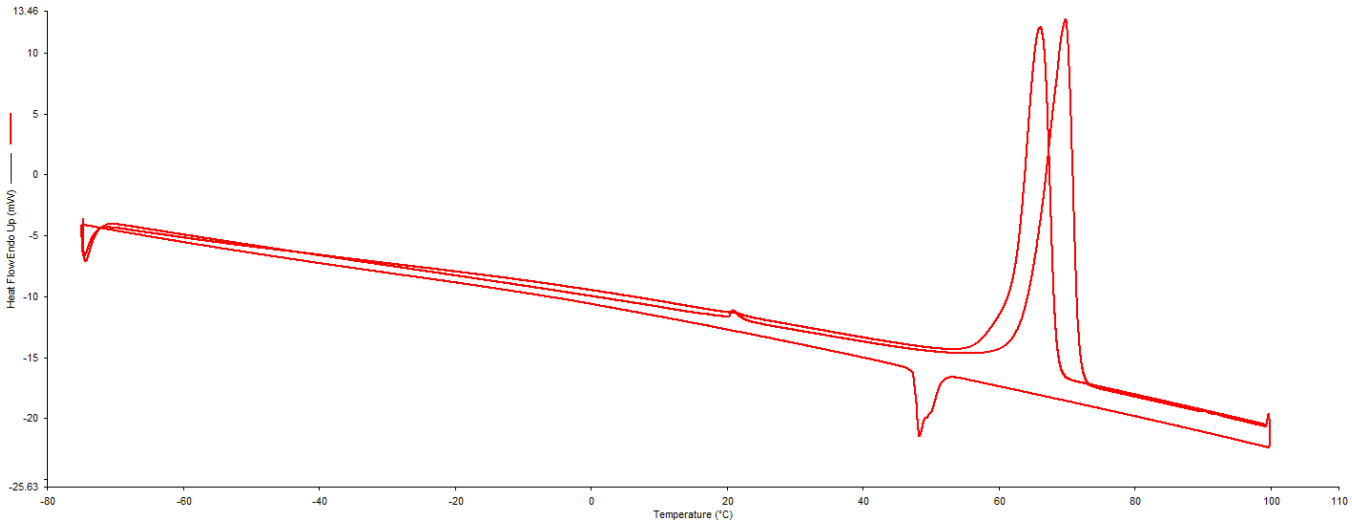

Figure 21. DSC of a 9779 psi PEO sample with cooling set to 1°C/min.

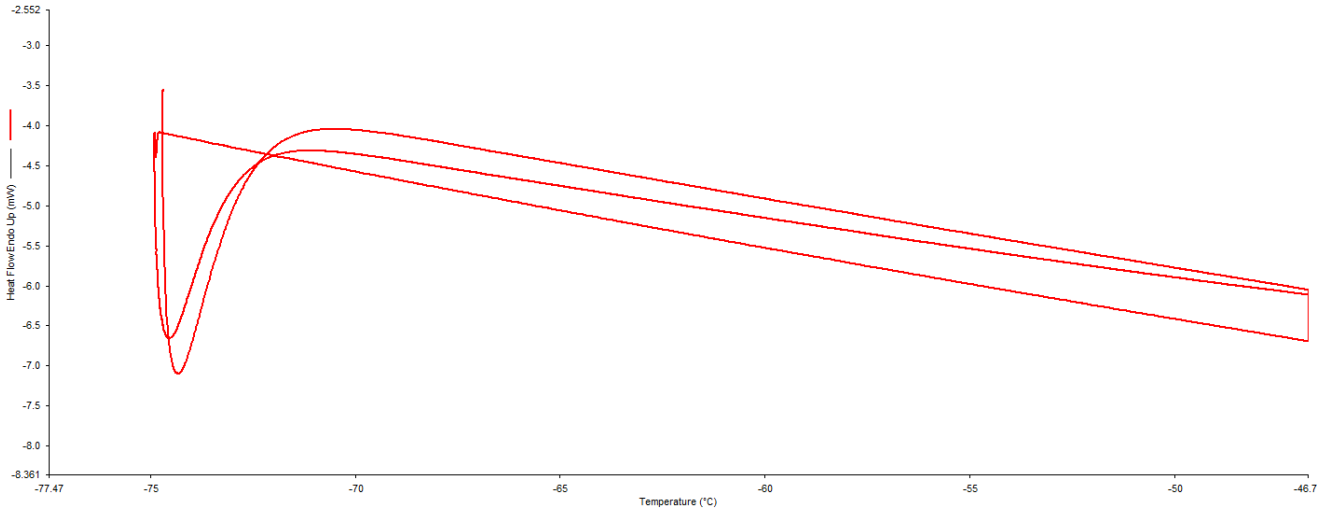

Figure 22. The cold range of the DSC graph from figure 21. Note the completely straight cooling line along the bottom of the three lines, with no spike or change.

Fourier-Transform Infrared Spectroscopy

The processed films were each examined via FTIR at three sites: the center of the film, an edge of the film that presented birefringence on visual inspection, and an edge of the film that did not present birefringence. For samples that had no birefringence visible when viewed through polarized sheets, only one edge reading was taken.

Table 8. FTIR peaks for the processed PEO films.

Peak	Cause	Moiety
2950	C-H Stretching	Alkanes
2882	C-H Stretching	
2860	C-H Stretching	
2806	C-H Stretching	
1467	C-H Bending	
1360	CH2 Wagging	
1340	C-H Bending	
1280	CH2 Twisting	
1238	CH2 Twisting	
1145	C-O Stretching	Ethers
1092	C-O Stretching	
1060	C-O Stretching	
960	CH2 Rocking	Alkanes
840	CH2 Rocking, C-O Stretching	Alkanes, Ethers

All samples showed consistent spectra via FTIR, with peaks outlined in Table 8. [23] [24] [25] [26] Every peak was associated with either C-H or C-O single bonds, which was expected. PEO is a polymer composed of repeating chains of two carbons and an oxygen, so the only bonds that should appear in FTIR are carbon-hydrogen, carbon-carbon, and carbon-oxygen single bonds.

Figure 23 shows an example of the spectra produced. The peaks of each spectrum vary widely in intensity for each sample, which would make it difficult to analyze them. This disparity was caused by the different thicknesses of each sample. A thicker sample absorbs more of the infrared due to

the larger amount of material the infrared must pass through. To rectify this, peak normalization was required.

Normalization was attempted using several peaks, but the most consistent results were obtained by normalizing with the 1090 C-O peak, which was also the strongest peak in every sample. This method resulted in the smallest disparity in peak intensities across the spectrum. A composite of every center region sample is shown in Figure 24 to demonstrate the effect of this normalization method.

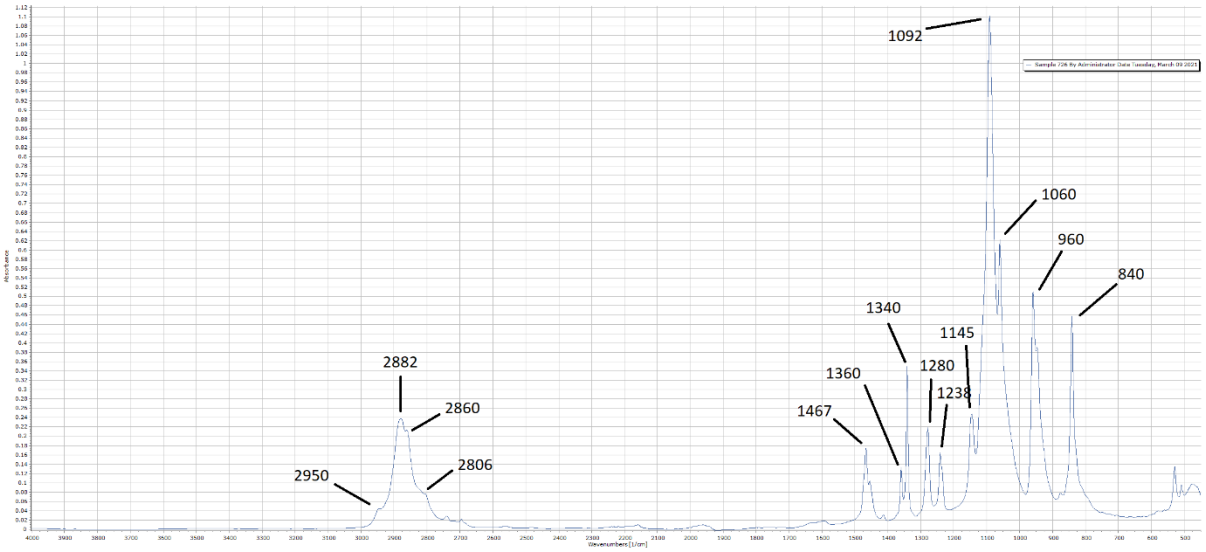

Figure 23. Full FTIR spectrum of the center region of a 9779 psi sample. Peaks are marked.

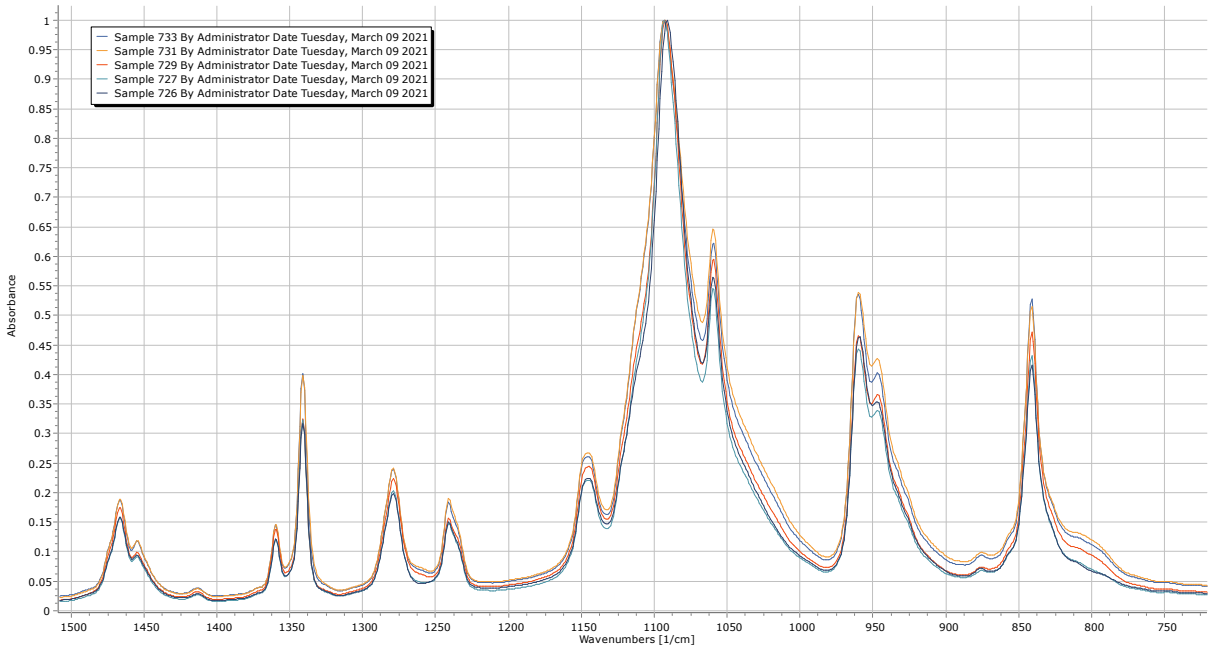

Figure 24. Composite of center region sample fingerprint regions. Center regions showed minimal differentiation between processing forces.

When examining FTIR spectra, it is always important to identify the differences between sample spectra. FTIR readings provide a general indication of the prevalence of different atomic bonds in a material, so it would be logical to assume that these spectra would only provide information about the material's chemical structure. However, a polymer's morphology can influence the bands in an FTIR reading in various ways. For example, certain copolymers containing PEO can experience peak broadening and blue shifts in the triple-peak region from 1050 to 1150 cm^{-1} when they become more amorphous. Peak broadening causes a given band to widen, potentially overlapping or even masking nearby peaks, while blue shifting causes a given band to peak at a slightly higher wavenumber. [27] However, drawing conclusions like these requires other analytical methods for confirmation, such as XRD.

The PEO samples showed two major regions with differences between sample spectra: the alkane bands from 2800 to 3000 cm^{-1}, and the fingerprint region, from 500 to 1500 cm^{-1}. An example of the differences found in the alkane bands is provided in Figure 25. These peaks

primarily showed a uniform change in intensity between samples with no broadening or shifting. The uniformity of the change in intensity could imply that this is an artifact of the differences in thickness between samples and the resulting peak normalization. In contrast, the changes in the fingerprint region were much less consistent, which could prove significant.

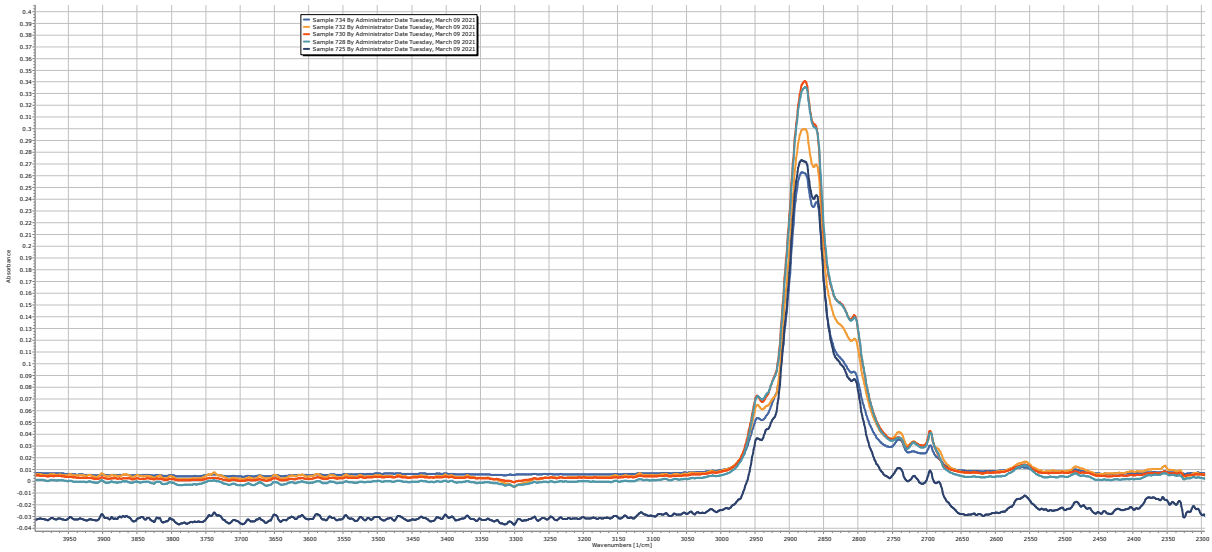

Figure 25. Composite of the 2800 - 3000 cm^{-1} alkane band in birefringent edge samples processed at all investigated pressures.

The fingerprint region showed several interesting variations between samples. The largest variation was seen in the C-O triple peak mentioned previously, with both peak broadening and blue shifting present in various samples. Examples of peak broadening and blue shifting are provided in Figures 26 and 27. Additionally, the following peaks showed variations in intensity between samples with minimal change in shape: 1467, 1360, 1280, 1238, and 840 cm^{-1}. All but one of these peaks were alkyl C-H peaks, with one exception: the 840 cm^{-1} peak. This peak can be linked to both CH2 rocking and C-O stretching, and showed the most extreme variation in intensity, as visualized in Figure 28. Finally, the twin peaks at 940 cm^{-1} and 960 cm^{-1} (both attributed to alkyl CH2 rocking) showed changes in both intensity and peak ratio. Both the 960:945 peak ratio and the combined intensity of both peaks are presented in Figures 29 and 30.

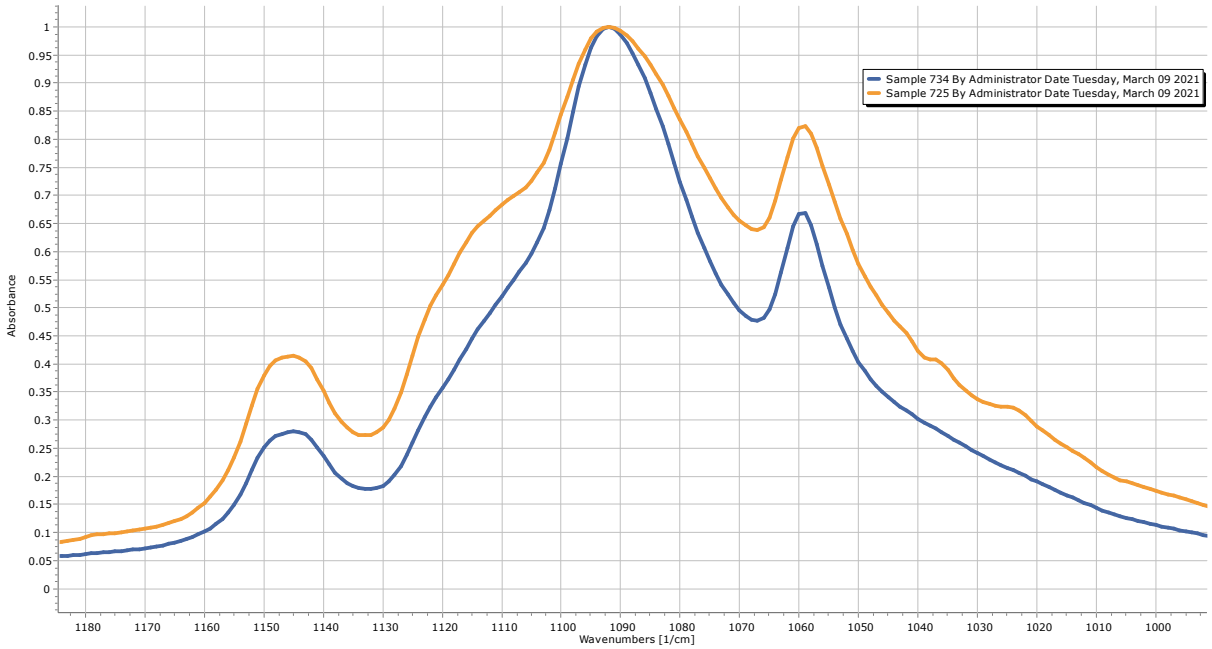

Figure 26. Broadening in the C-O triple peak. The birefringent edge of a 9779 psi sample (orange) shows broader peaks than the edge region of a 1,000 lb_f sample (blue). Not that peaks remain distinct and discrete, indicating weak broadening.

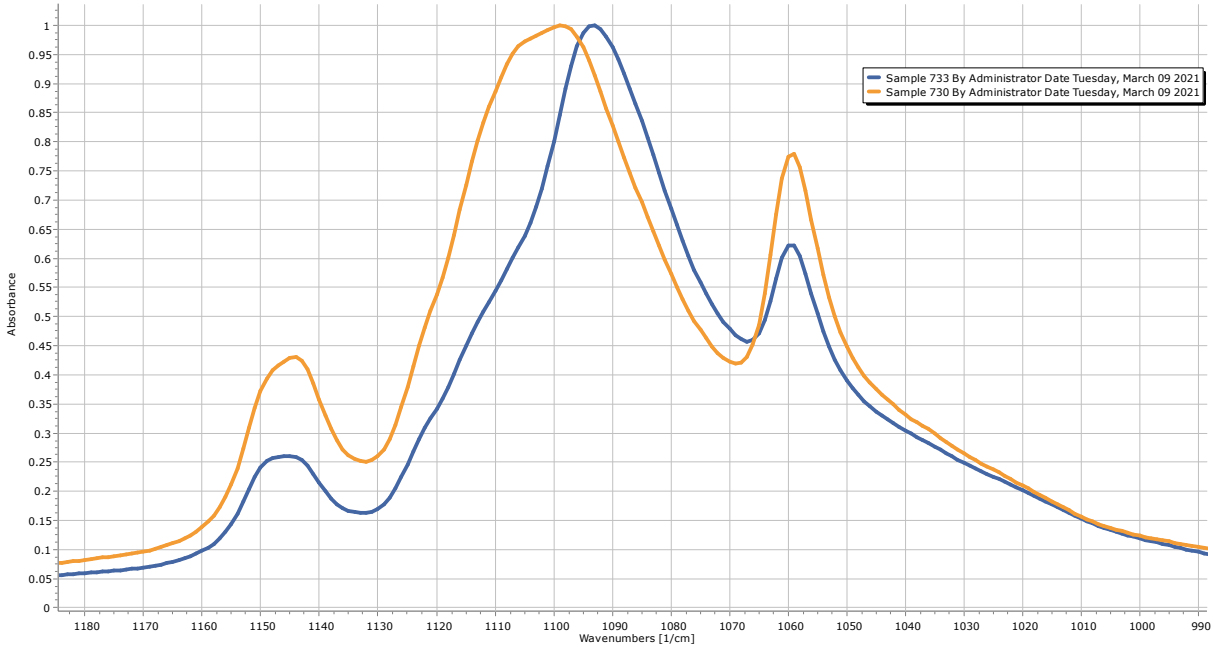

Figure 27. Blue shift of the 1090 peak. The birefringent edge of a 3663 psi sample (orange) shows a distinct upward shift in wavenumber compared to the edge of a 1,000 lbf sample (blue).

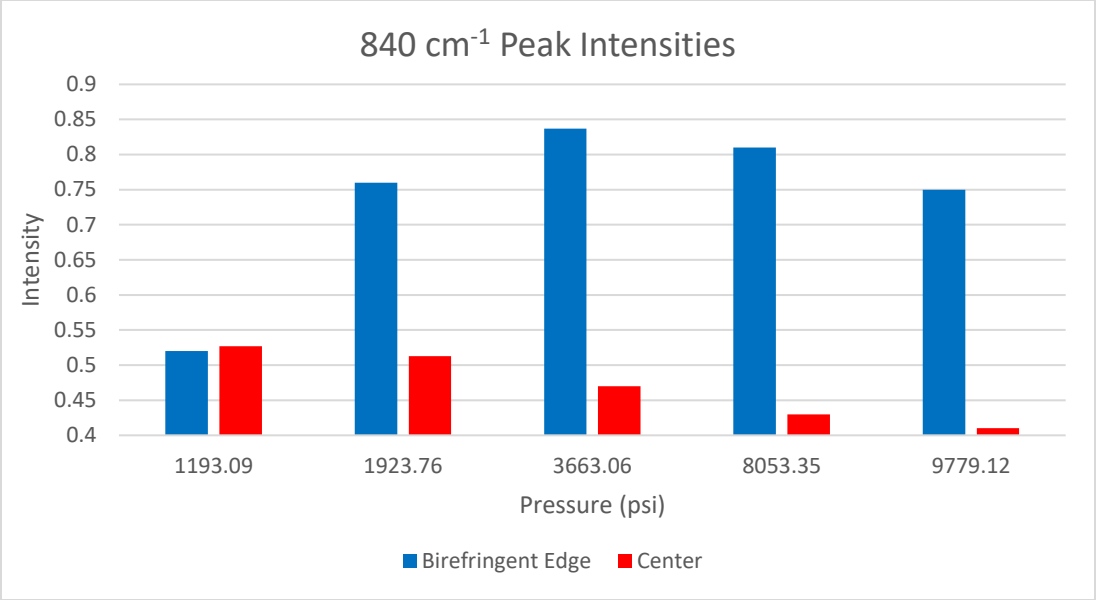

Figure 28. Normalized peak intensities of the 840 cm^{-1} peak in both center and birefringent edge samples.

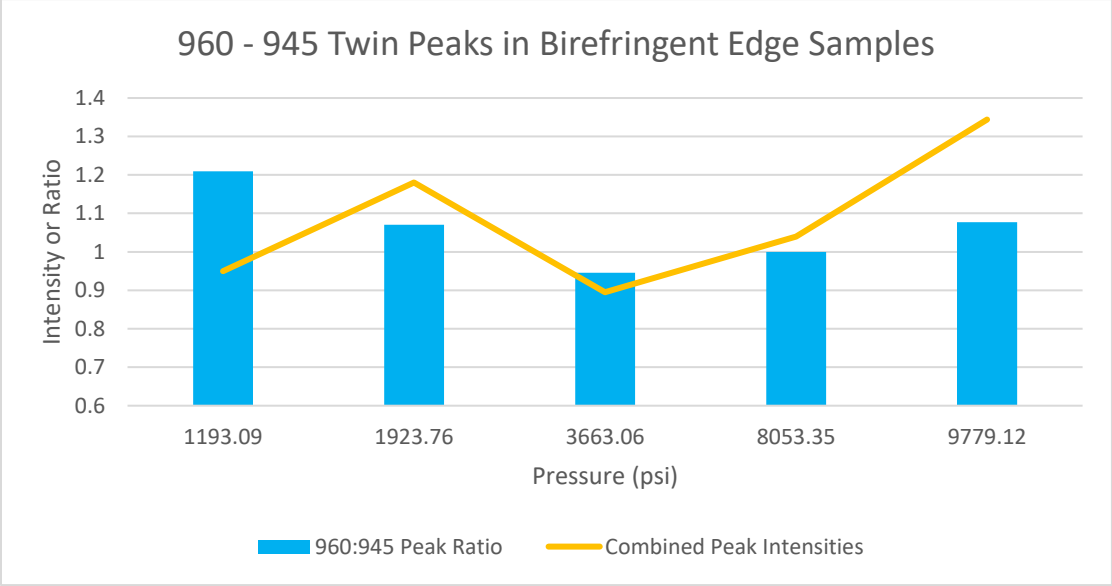

Figure 29. Normalized peak ratio and combined peak intensity of the 960-945 cm^{-1} twin peaks in birefringent edge samples.

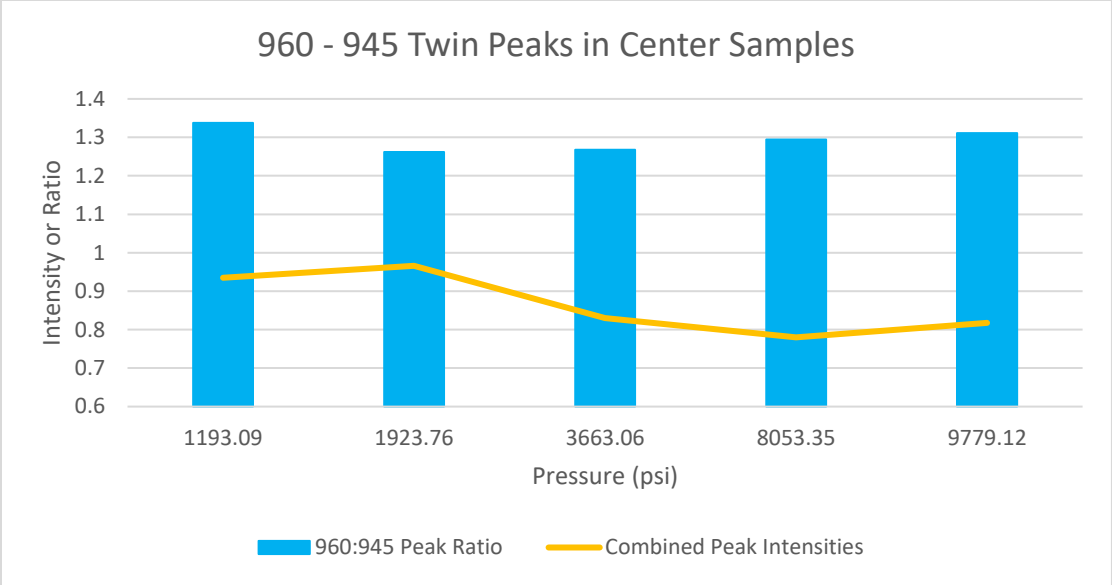

Figure 30. Normalized peak ratio and combined peak intensity of the 960-945 cm^{-1} twin peaks in center samples.

It is interesting to note the difference in these peak characters not only between pressures, but also between regions of the samples. The center region shows no change in the 960-945 twin peaks (Figure 30), with a gradual decline in 840 peak intensity (Figure 28). Meanwhile, the birefringent edge samples show several notable changes with pressure: the 840 peak rises and falls, peaking in intensity at 3663 psi (Figure 28), while showing the opposite pattern with twin peak ratios (Figure 29). Additionally, the combined peak intensity changes significantly while not showing a consistent pattern. These findings would suggest that something is happening in the samples at the edges where birefringence is noted.

While these findings are interesting, nothing concrete can be concluded from them alone. These FTIR phenomena will have to be linked to conformational or structural features of the samples using other analytical methods, such as DSC or XRD. However, the existence of these phenomena at least demonstrates that heat and pressure treatment of PEO has detectable morphological effects.

X-ray Diffraction

The samples analyzed via XRD were not the same samples that were analyzed in previous sections. Previous sections involved the analysis of PEO processed at 60 C and a variety of pressures between 1193 psi and 9779 psi. The samples analyzed here were processed with 20,000 lb_f of force, significantly higher, and a range of temperatures from 25 C to 62 C.

XRD spectra consistently showed two strong crystal peaks between samples, at 2theta values of 19.3 and 23.5. These peaks correspond to the (120) and (032) crystal planes, respectively. Additionally, a third crystal plane is known in PEO: the (110) plane, at a 2theta value of 15. [28] However, this plane did not present a strong peak in any samples, instead showing a weak twin peak. These peaks are shown and labeled in Figure 31.

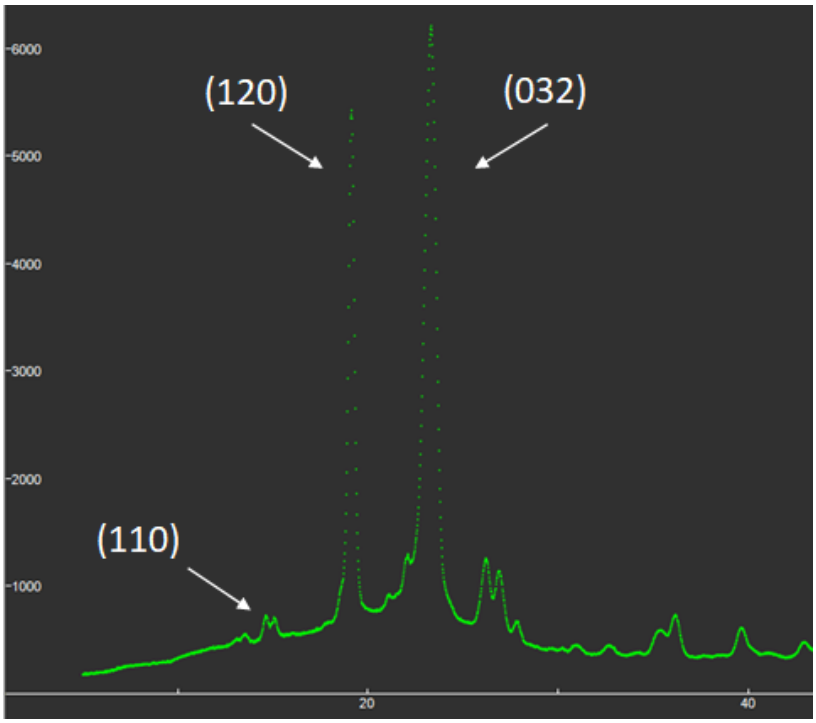

Figure 31. XRD spectrum of unprocessed PEO. Crystalline peaks are labeled with miller indices for crystal planes.

In addition to spectra like the one shown in Figure 31, XRD measurements also provide imagery of the diffracted wave intensities. Images taken from samples are compiled in Figure 32.

Two major paradigms were seen in these images: two thin rings, and two alternating thin bands. Thin rings are a traditional crystalline paradigm, while alternating thick bands would be evidence of mesophase formation; condis crystal, specifically. However, these bands are thin, which instead suggests orientation of the crystalline phase. A short comparison of different XRD paradigms is provided in Figure 33.

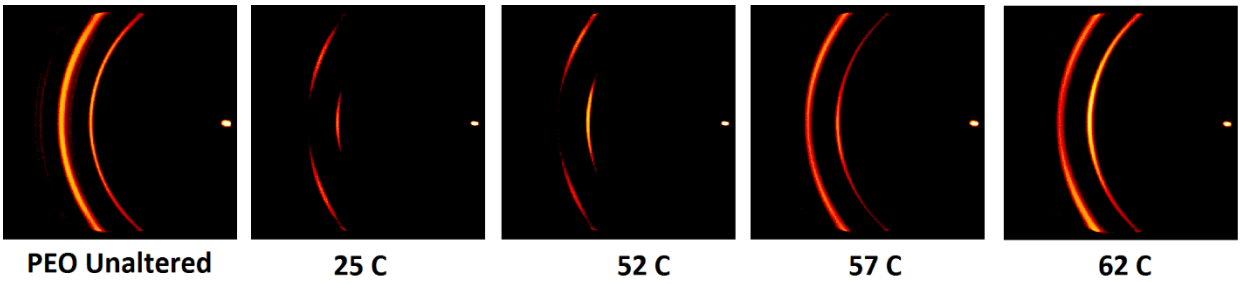

Figure 32. Images from XRD of samples pressed at 20,000 lb_f and varying temperatures.

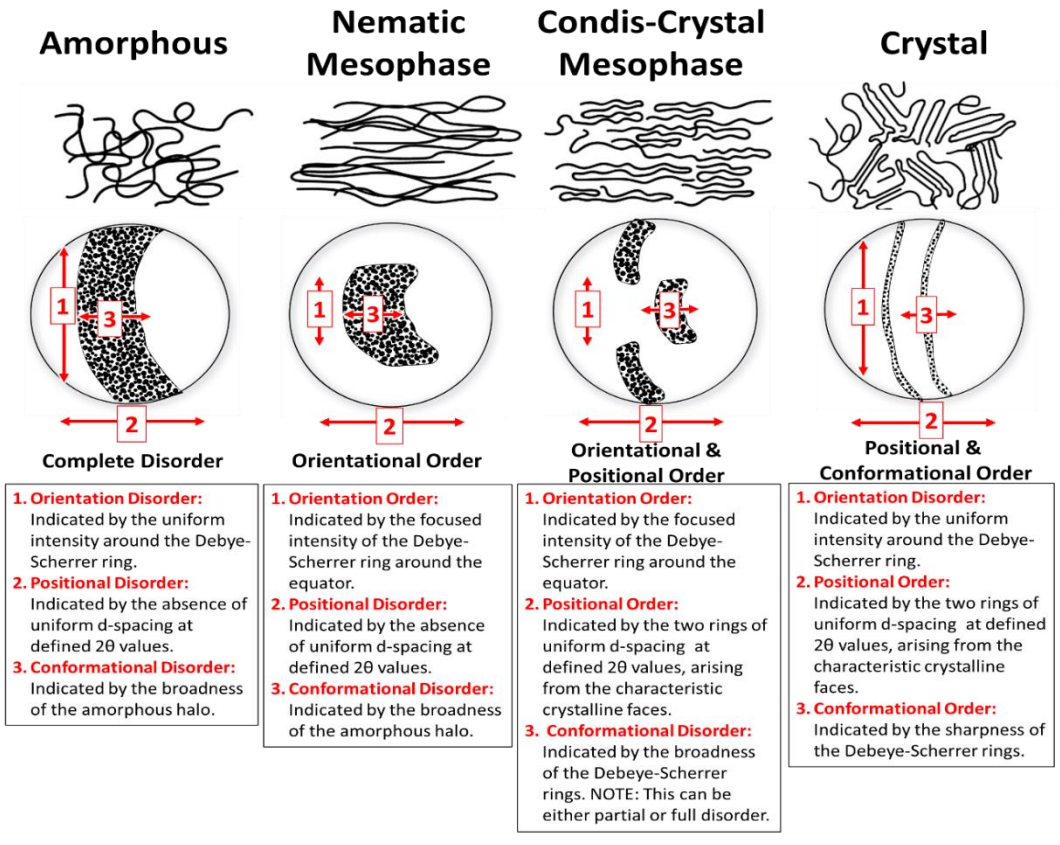

Figure 33. A summary of different XRD paradigms and their conformational significance. Provided by Cameron Baptista from the Mathiowitz Lab at Brown University.

Traditionally, crystalline peaks are expected to adopt a gaussian shape, with non-gaussian peaks indicating either multiple overlapping amorphous peaks or, potentially, mesophase formation. As such, the shapes of these peaks needed to be characterized. The main crystalline peaks of these samples showed a non-gaussian shape, as demonstrated in Figure 34. If this non-gaussian shape were only present in treated samples, which could potentially form a mesophase, then the peaks' shape could serve as evidence of this phase forming during treatment. However, Figure 34 also shows an example of the peaks in an untreated PEO sample, with an almost identical non-gaussian shape. Since PEO is non-mesogenic and cannot form a mesophase without induction processes, this non-gaussian shape cannot be evidence of mesophase formation and is instead evidence of either overlapping amorphous peaks or non-standard peak character.

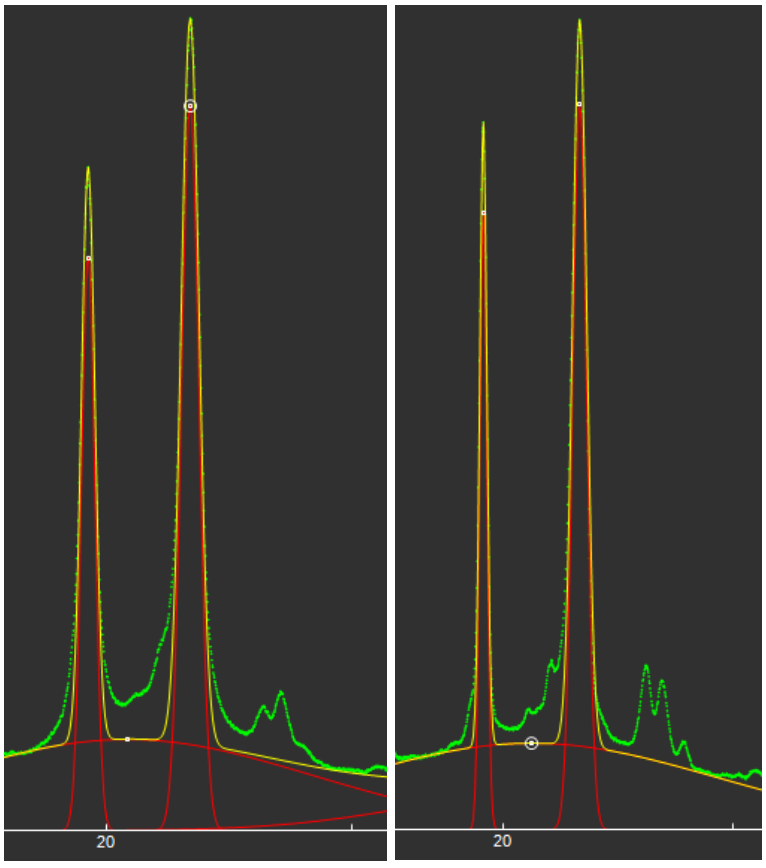

Figure 34. Comparison of heat- and pressure-treated (left) and untreated (right) PEO samples in XRD, in green. Gaussian deconvolution peaks are red, with deconvolution composites in yellow.

In addition to peak shape, several other properties can provide insight into the phase composition of polymers. Figure 35 shows the calculated "full width at half-maximum" (FWHM) values of the two major peaks in each sample. FWHM measures the width of an XRD peak halfway up the height of the peak, providing a simple quantification of the width of a given peak. Typically, crystalline materials have peaks with low FWHM values, and amorphous materials have peaks with high FWHM values. Meanwhile, mesophase formation increases the FWHM value by 2 or 3. In the case of these PEO samples, FWHM values did increase, but only by values of about 0.2 at most. This means the FWHM values are not strong indicators of any morphological change in the samples.

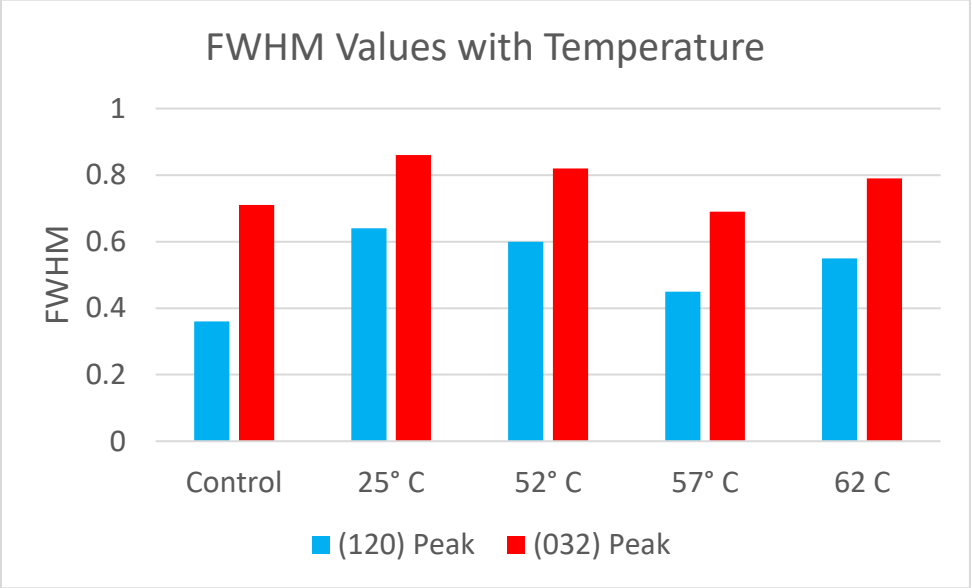

Figure 35. Graph of major peak FWHM values with processing temperature.

A much larger difference was seen in other properties of the two major peaks: peak intensity and peak intensity ratio. As operating temperatures increased, the (120) peak increased in intensity while the (032) peak decreased, resulting in the peak ratio flipping. However, once the crystalline and amorphous peaks of the sample deconvolutions were summed and the degree of

crystallinity in each sample was calculated, no change in crystallinity was seen. A combined graph of the peak intensities and DOC is presented in Figure 36.

Normally, mesophase formation would be accompanied by an increase in DOC due to the mesophase peaks contributing to the deconvoluted crystalline peaks. Once mesophase content would be determined, those peaks could then be singled out and mesophase content could be calculated, allowing for a full phase composition of the material to be known. Since the calculated DOC values in these samples remain consistent, it would be unlikely for the phase composition to be changing in this way. Instead, the change in peak ratio suggests that the crystal phase of the polymer is being reoriented to a different plane, changing from the (032) plane to the (120) plane.

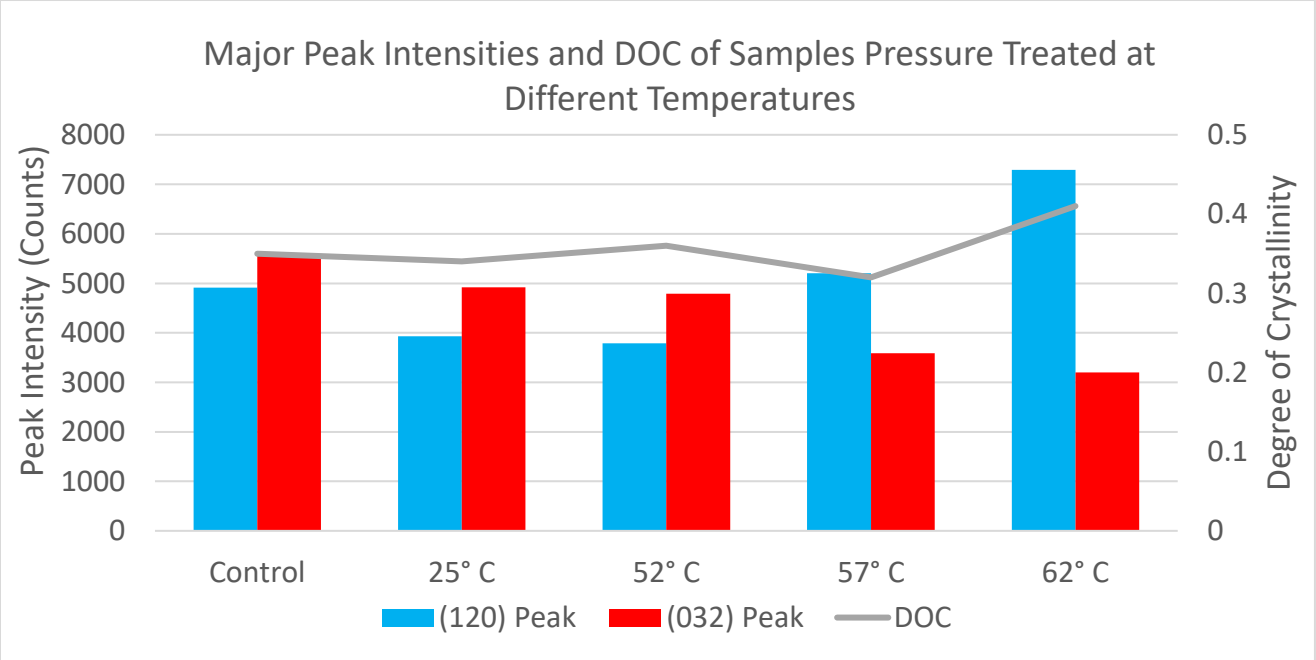

Figure 36. Major peak intensities and degree of crystallinity with temperature.

In addition to the data reported above, a series of "hot stage" XRD measurements were taken. Hot stage XRD measurements are taken as the sample changes in temperature, allowing for a material to be measured at a wide range of instantaneous temperatures. This way, if the phase composition were to change as the material heated up (for example, due to a glass transition), this

change could be measured. However, in the case of these samples, no changes were seen in hot stage measurements with temperature. This makes sense: the PEO used in this work has a glass transition of -67 C, and no other thermal phenomena were found using DSC. Since the hot stage XRD could not operate at temperatures near that glass transition, the only thermal phenomenon to be encountered would be the melting point. In fact, melting was seen in the hot stage XRD measurements, as shown in Figure 37. Above the melting point, the material began to become fluid, as shown in the fuzziness of the data points and the amorphous nature of every deconvolution peak. This stood in contrast with the same sample below the melting point, which had clear crystalline peaks and finer data points.

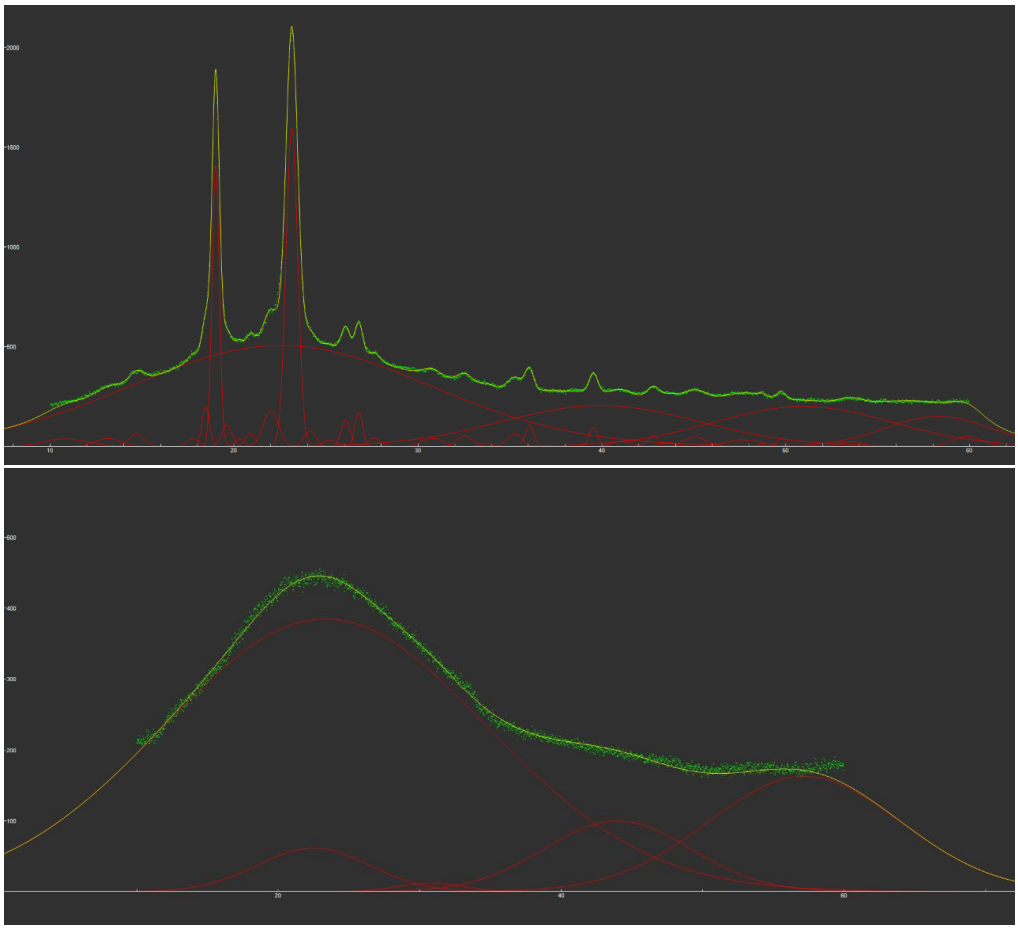

Figure 37. A hot stage XRD sample measured below (top) and above (bottom) the melting point. Original data is green, with deconvolution peaks in red and deconvolution composites in yellow.

All put together, this data suggests that heat and pressure treatment alters the morphology of PEO by forcing a reorientation of the material's crystalline phase to favor the (120) plane. Additionally, no thermal phase phenomena were seen between 25 C and 65 C, which was expected. However, no evidence of mesophase formation was found. Since XRD was only performed on samples processed at 20,000 lb_f, it remains possible that lower pressures could still induce a mesophase in the polymer.

Summary of Results

Polarized microscopy showed that PEO developed a consistent pattern of birefringence that intensified with increasing compression, such that higher pressures resulted in nearly uniform birefringence across the samples. Birefringence indicates elevated crystallinity, as well as sometimes implying the formation of mesophases. However, spherulite formation, a key indicator of crystallinity, was not seen, most likely due to the thickness of the films. Additionally, unprocessed PEO samples also showed birefringence that seemed to follow the pattern seen in samples processed at higher pressures, despite lower-pressure samples not exhibiting this pattern.

Differential scanning calorimetry showed that the heated compression technique caused a marked shift in the samples' melting points, as well as the heats of fusion, indicating that the samples became more crystalline. However, the glass transition, an expected feature of the material, was not identifiable. Instead, the material demonstrated no structural changes at the expected temperatures. Interestingly, scans instead showed a sharp spike when cooling near the glass transition temperature. This may have been an artifact caused by the machine's cooling system.

Infrared spectroscopy showed several interesting phenomena. Blue shifting and peak broadening were found in the 1050-1150 cm^{-1} triple peak associated with ether bonds, although with no clear pattern. A peak at 840 cm^{-1} showed interesting changes in intensity with pressure depending on the region of the sample being measured, with birefringent edges showing significantly more change than sample centers. A similar difference was noted in a pair of peaks at 960-945 cm^{-1}, which showed notable changes in both peak ratio and combined peak intensity with pressure at birefringent edges, but not sample centers.

X-ray diffraction of 20,000 lb_f-processed samples showed strong evidence for a reorientation of the polymer's crystalline phase to favor the (120) plane when processed at high pressures and varying temperatures, as seen in the ratio of peak intensities for the material's major crystal peaks. Additionally, no conformational changes were seen when samples were heated below the melting point. Finally, no samples demonstrated mesophase formation, based on the crystal peak shapes, FWHM values, and calculated crystallinity values.

Future Considerations

While polarized microscopy, differential scanning calorimetry, and FTIR are all useful tools for investigating polymer morphology, X-ray diffraction would produce a much more in-depth analysis for the samples produced in this work, providing insight on several key elements of the structure, such as planes of crystallinity and chain orientation. Quantifying the prominence of the material's crystalline planes would greatly clarify the changes in crystallinity of the samples. Meanwhile, understanding the chain orientation of the samples would be a major step forward for answering the question of mesophase formation. PLA and PCL have already been demonstrated to generate mesophases using the heated compression technique via XRD, but PEO has not, as shown here. It was hypothesized that this could be a result of the pressure used in those PEO studies, and so XRD analysis of the samples produced for this work, processed across a range of pressures, would provide clarity on the matter. Once the equipment is available for use again in the near future, these questions can be answered.

In addition to more fully analyzing the samples produced in this work, it may also be useful to produce additional samples processed at different parameters. The non-XRD results presented in this work were obtained for samples processed at 60°C. This temperature was initially chosen due to its optimal induction of birefringence and crystal formation, but XRD analysis of previous samples suggests that a lower temperature, such as 55°C, may prove more fruitful when investigating mesophase induction.

Conclusion

Polyethylene oxide, as a material, has already proven itself useful in multiple areas. Even better, it has also shown great potential for future utility through new processing techniques. Characterizing and quantifying the changes heat and pressure treatment induce in the material's morphology could result in many advances in PEO-reliant technologies. Additionally, it is important to determine whether this treatment process can induce one or several of the mesophases in PEO's structure, due to the effects these phases can have on a polymer.

This work served to demonstrate several of the effects of heat and pressure treatment on high molecular weight PEO. This treatment process confers birefringence and increased crystallinity to PEO proportionally to the pressure exerted, when processed at temperatures slightly below the melting point, but has not been proven to induce mesophase formation in the material.

More analysis and experimentation is required to confirm whether this process can induce mesophase formation in PEO samples. A wider range of pressure and temperature combinations should be used with this treatment protocol. Additionally, the samples produced for this work should be analyzed using x-ray diffraction for deeper understanding of the morphological effects of the treatment.

While there is much work left to be done to determine the benefits of heat and pressure treatment on PEO, this technique has already shown great potential in mesophase induction of other non-mesogenic polymers. If a mesophase can be formed in PEO using this technique, its potential utility would be greatly improved across many applications.

References

[1] Y. Tong, Y. Lin, S. Wang and M. Song, "A study of crystallisation of poly(ethylene oxide) and polypropylene on graphene surface," *Polymer,* vol. 73, pp. 52-61, 2015.

[2] University of Cambridge, "DoITPoMS - TLP Library Crystallinity in polymers - Spherulites and optical properties," 2020. [Online]. Available: https://www.doitpoms.ac.uk/tlplib/polymers/spherulites.php.

[3] J. R. White, "Polymer ageing: physics, chemistry, or engineering? Time to reflect," *C. R. Chimie,* vol. 9, pp. 1396-1408, 2006.

[4] B. Wunderlich, "A classification of molecules, phases, and transitions as recognized by thermal analysis," *Thermochimica Acta,* no. 340-341, pp. 37-52, 1999.

[5] S. Ran, X. Zong, D. Fang, B. S. Hsiao and B. Chu, "Studies of the mesophase development in polymeric fibers during deformation by synchrotron SAXS/WAXD," *Journal of Materials Science,* vol. 36, pp. 3071-3077, 2001.

[6] C. M. Baker, A. Azagaury and E. Mathiowitz, "Effect of pressure on poly-l-lactic acid morphology," *Polymer,* vol. 99, pp. 250-262, 2016.

[7] Alfa Aesar, "25322-68-3 - Polyethylene oxide, M.W. 300,000," 2021. [Online]. Available: https://www.alfa.com/en/catalog/042237/.

[8] L. Ma, L. Deng and J. Chen, "Applications of poly(ethylene oxide) in controlled release tablet systems: a review," *Drug Development and Industrial Pharmacy,* vol. 40, no. 7, pp. 845-851, 2013.

[9] Z. Xue, D. He and X. Xiaolin, "Poly(ethylene oxide)-based electrolytes for lithium-ion batteries," *Journal of Materials Chemistry A,* no. 38, 2015.

[10] C. Baptista, A. Azagury, H. Shin, C. M. Baker, E. Ly, R. Lee and E. Mathiowitz, "The effect of temperature and pressure on polycaprolactone morphology," *Polymer,* vol. 191, 2020.

[11] Encyclopaedia Britannica, "Polarization," 2021. [Online]. Available: https://www.britannica.com/science/polarization-physics.

[12] Polymer Science Learning Center, "Differential Scanning Calorimetry," 2021. [Online]. Available: https://www.pslc.ws/macrog/dsc.htm.

[13] Humboldt University of Berlin, Faculty of Mathematics and Natural Sciences, Investigation of Polymers with Differential Scanning Calorimetry, 2021.

[14] A. Ausili, M. Sanchez and J. C. Gomez-Fernandez, "Attenuated total reflectance infrared spectroscopy: A powerful method for the simultaneous study of structure and spatial orientation of lipids and membrane proteins," *Biomedical Spectroscopy and Imaging,* vol. 4, pp. 159-170, 2015.

[15] J. Epp, "4 - X-ray diffraction (XRD) techniques for materials characterization," in *Materials Characterization Using Nondestructive Evaluation (NDE) Methods,* Woodhead Publishing, 2016, pp. 81-124.

[16] Millipore Sigma, "Poly(ethylene oxide) average Mv ~ 300,000, powder," 2021. [Online]. Available: https://www.sigmaaldrich.com/catalog/product/aldrich/182001?lang=en&region=US.

[17] M. F, ""Spectragryph - optical spectroscopy software", Version 1.2.15," 2020. [Online]. Available: http://www.effemm2.de/spectragryph/.

[18] J. M. Marentette and G. R. Brown, "Polymer Spherulites: I. Birefringence and morphology," *Journal of Chemical Education,* vol. 70, no. 6, pp. 435-439, 1993.

[19] P. Phulkerd, S. Arayachukeat, T. Huang, T. Inoue, S. Nobukawa and M. Yamaguchi, "Melting Point Elevation of Isotactic Polypropylene," *Journal of Macromolecular Science, Part B,* vol. 53, no. 7, pp. 1222-1230, 2014.

[20] Mettler Toledo, "Determination of Crystallinity," 2021. [Online]. Available: https://www.mt.com/us/en/home/supportive_content/matchar_apps/MatChar_HB404.html.

[21] J. L. Thelen, X. C. Chen, S. Inceoglu and N. P. Balsara, "Influence of Miscibility on Poly(ethylene oxide) Crystallization from Disordered Melts of Block Copolymers with Lithium and Magnesium Counterions," *Macromolecules,* vol. 50, no. 12, pp. 4827-4839, 2017.

[22] J. C. Dyre, "Colloquium: The glass transition and elastic models of glass-forming liquids," *Reviews of Modern Physics,* vol. 78, no. 3, pp. 953-972, 2006.

[23] Millipore Sigma, "IR Spectrum Table & Chart," 2021. [Online]. Available: https://www.sigmaaldrich.com/technical-documents/articles/biology/ir-spectrum-table.html.

[24] Y.-l. Su, J. Wang and H.-z. Liu, "FTIR Spectroscopic Investigation of Effects of Temperature and Concentration on PEO-PPO-PEO Block Copolymer Properties in Aqueous Solutions," *Macromolecules,* vol. 35, pp. 6426-6431, 2002.

[25] S. Rajendran, R. Kannan and O. Mahendran, "Ionic conductivity studies in poly(methylmethacrylate)-polyethylene oxide hybrid polymer electrolytes with lithium salts," *Journal of Power Sources,* vol. 96, pp. 406-410, 2001.

[26] H. K. Koduru, Y. G. Marinov, G. B. Hadjichristov and N. Scaramuzza, "Characterization of polymer/liquid crystal composite based electrolyte membranes for sodium ion battery applications," *Solid State Ionics,* vol. 335, pp. 86-96, 2019.

[27] W. Thitisomboon, Q. Gu, L.-T. Weng and P. Gao, "Surface confinement induced amorphization of polyethylene oxide in hgh-performance porous polyethylene films," *Polymer,* vol. 217, 2021.

[28] Y. Wu, L. Li, S. Chen, J. Qin, X. Chen, D. Zhou and H. Wu, "Sythesis, characterization, and crystallization behaviors of poly(D-lactic acid)-based triblock copolymer," *Scientific Reports,* vol. 10, 2020.

Appendices

Appendix A: Pressure Calculations

Films were elliptical in shape, so surface areas were calculated using the long and short diameters. Pressure was then calculated using the resulting surface area and the prescribed absolute force value of the press during sample treatment.

Table 9. Expanded pressure calculation values.

Sample Force (lb_f)	Diameters (mm)	Surface Area (mm^2)	Surface Area (in^2)	Pressure (psi)
0	14.75 x 15	173.77	0.26934	0
1000	25.5 x 27	540.75	0.83816	1193.09
2000	28 x 30.5	670.73	1.03963	1923.76
5000	32.5 x 34.5	880.63	1.36498	3663.06
10000	30 x 34	801.11	1.24172	8053.35
15000	35 x 36	989.6	1.53388	9779.12

Appendix B: Differential Scanning Calorimetry

Below are all calculated values used in this work based on DSC results:

Table 10. Sample melting parameters as calculated via DSC.

Sample (lb_f)	First Melt (°C)	First Melt ΔH (J/g)	First Melt DOC	Second Melt (°C)	Second Melt ΔH (J/g)	Second Melt DOC
0	66.96	175.0543	81.04366	64.46	157.3868	72.86426
1000	69.41	184.2173	85.28579	65.2	153.3253	70.98394
2000	68.46	181.1657	83.87301	64.61	147.3338	68.21009
5000	69.59	183.3616	84.88963	64.74	147.933	68.4875
10000	70.75	179.9989	83.33282	65.7	150.7417	69.78782
10000	69.39	186.3231	86.26069	65.71	158.0216	73.15815
15000	69.23	189.2385	87.61042	64.82	159.2195	73.71273
Mean	**69.11285714**	**182.76563**	**84.61372**	**65.03429**	**153.4231**	**71.02921**
STD	**1.078871292**	**4.2543313**	**1.969598**	**0.473523**	**4.549342436**	**2.106177**

Table 11. Sample crystallization parameters as calculated via DSC.

Sample (lb_f)	Cooling (°C)	Cooling ΔH (-J/g)
0	38.26	148.4075
1000	40.11	150.5828
2000	39.79	151.0021
5000	39.17	146.0526
10000	40.38	149.5483
10000	39.81	150.8146
15000	40.35	150.6224
Mean	**39.69571**	**149.5758**
STD	**0.699752**	**1.667205**

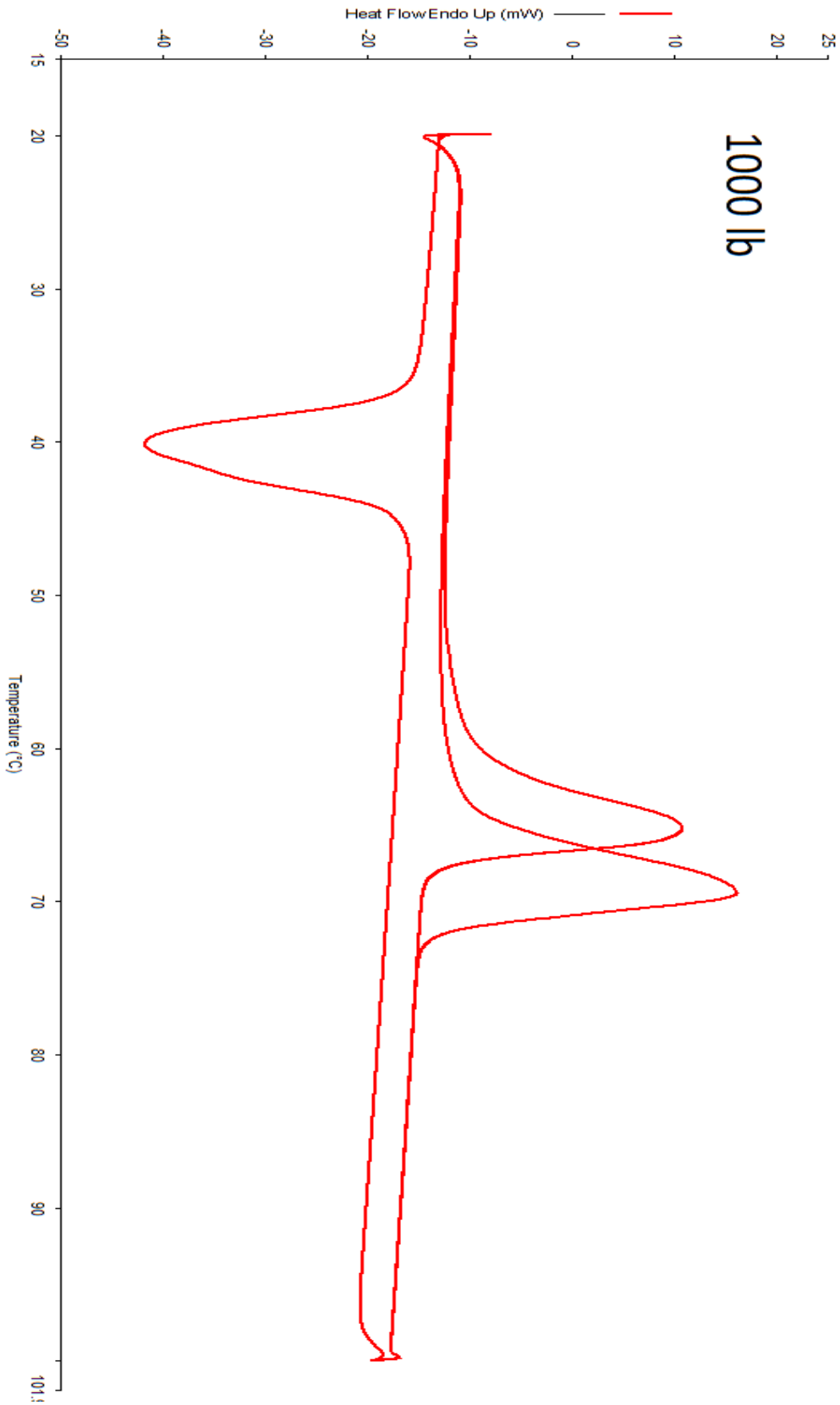

Figure 38. 1000 lb_f sample (1193 psi) DSC run from 20 C to 100 C at 10 C/min. Includes two melts and one cooling curve.

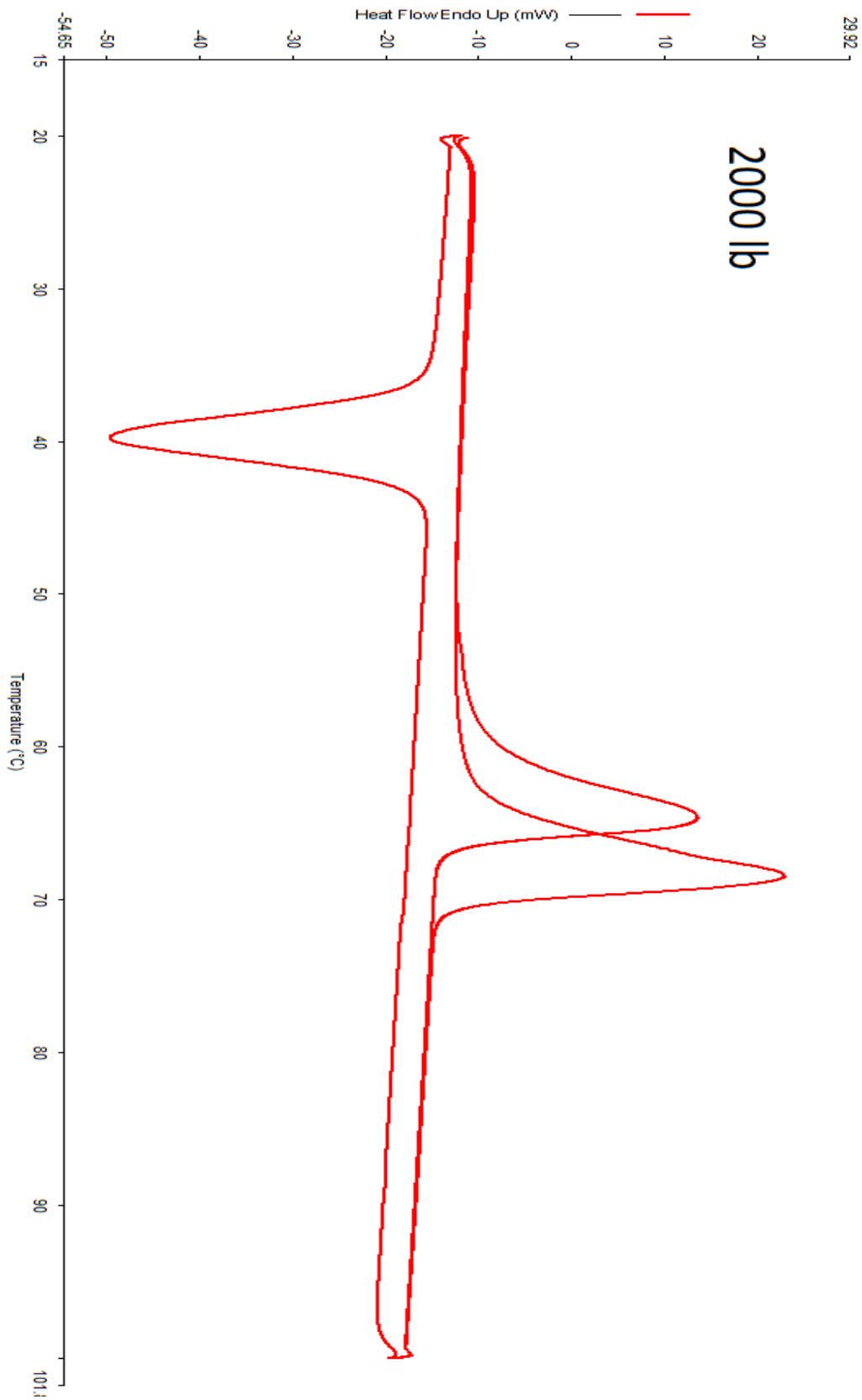

Figure 39. 2000 lbf sample (1924 psi) DSC run from 20 C to 100 C at 10 C/min. Includes two melts and one cooling curve.

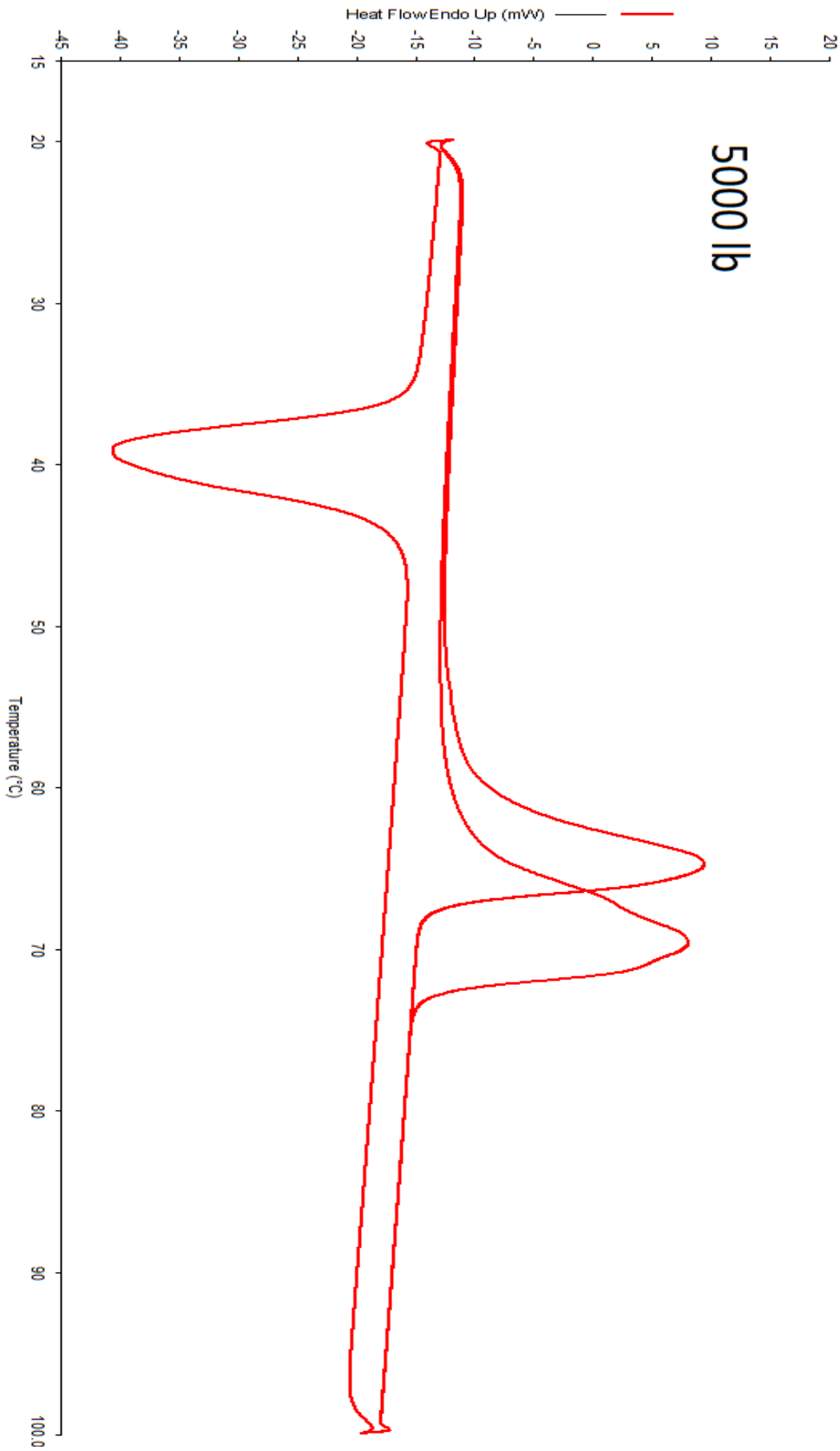

Figure 40. 5000 lbf sample (3663 psi) DSC run from 20 C to 100 C at 10 C/min. Includes two melts and one cooling curve.

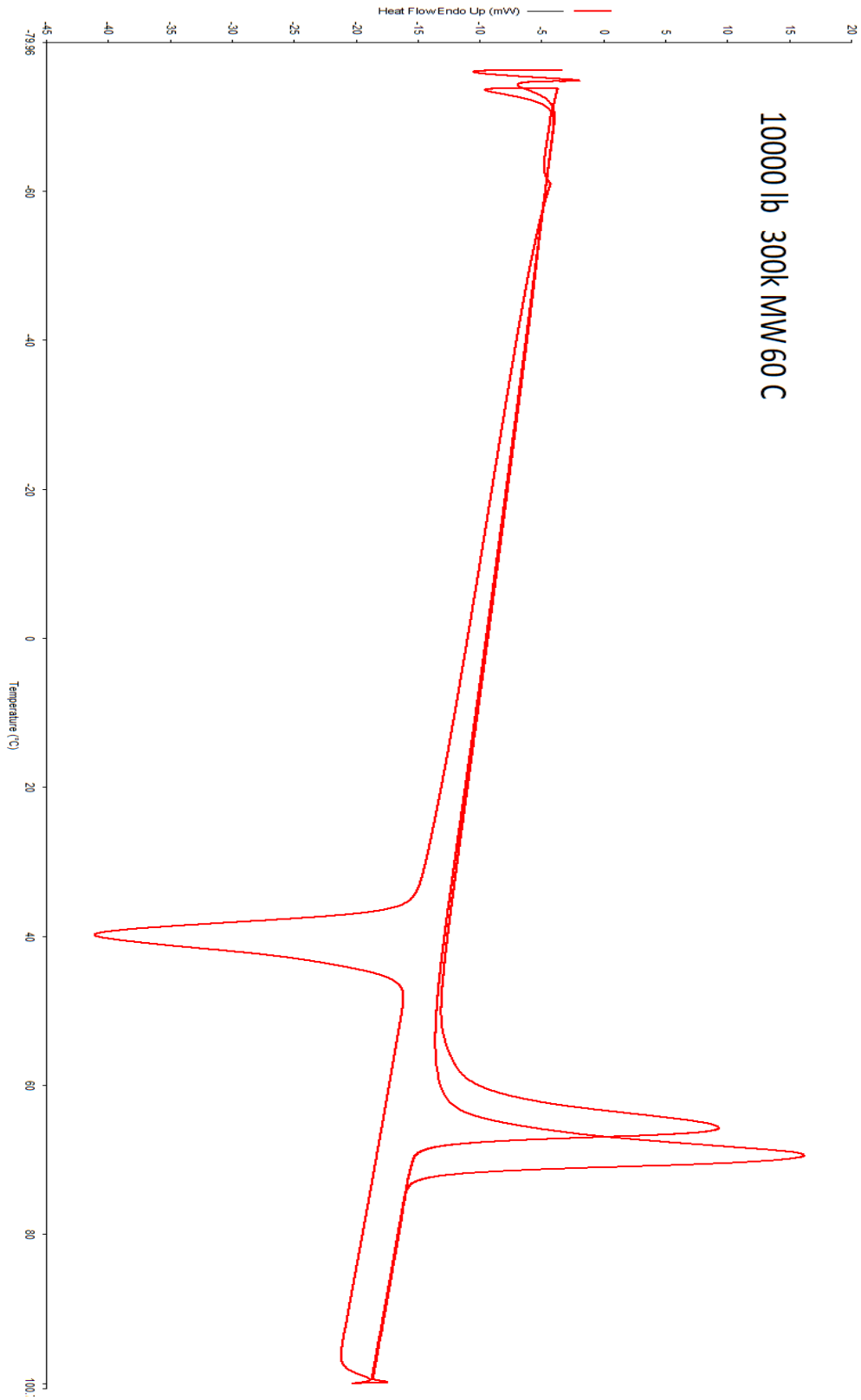

Figure 41. 10000 lbf sample (8053 psi) DSC run from -75 C to 100 C at 10 C/min. Includes two melts and one cooling curve.

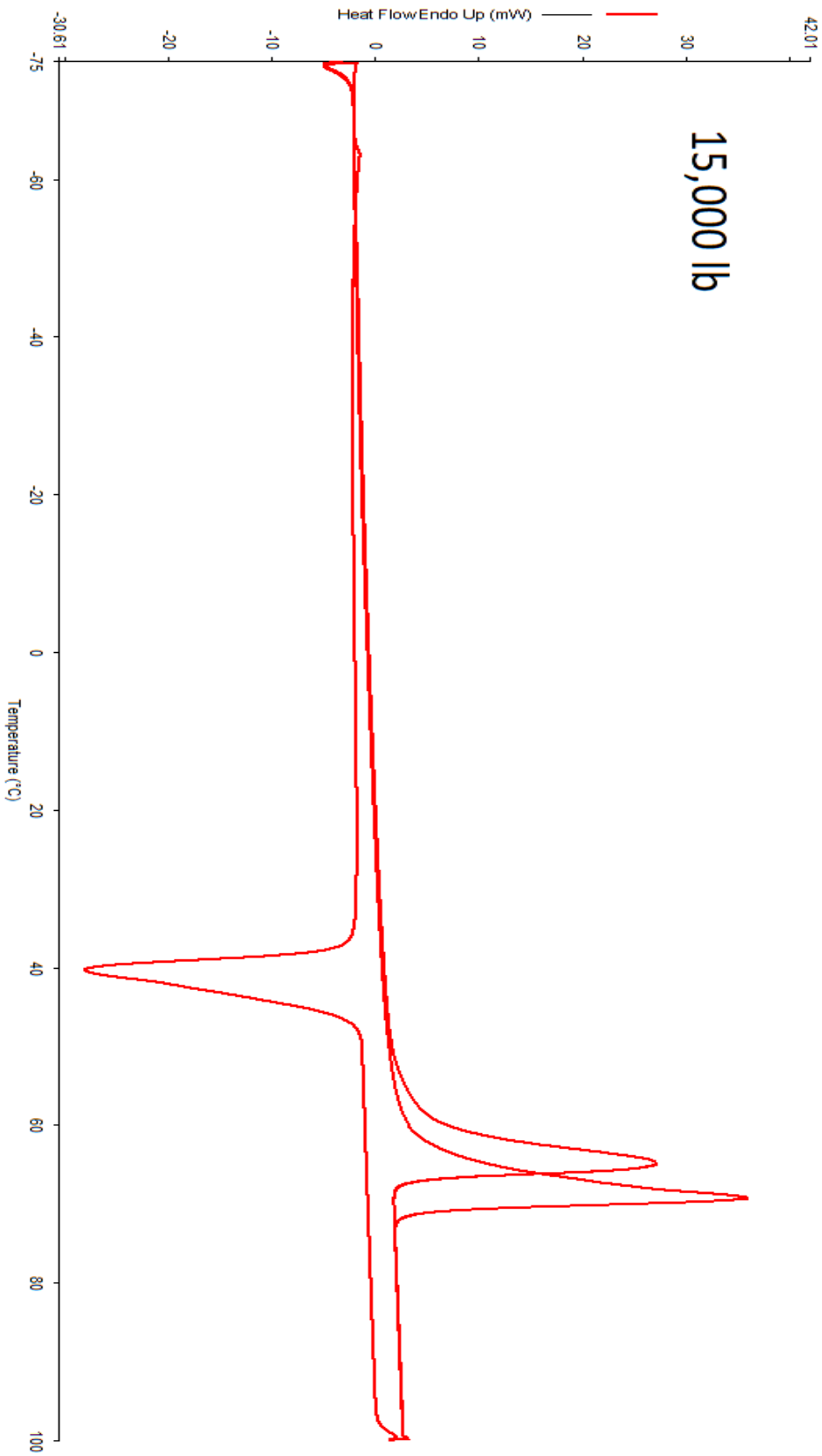

Figure 42. 15000 lbf sample (9779 psi) DSC run from -75 C to 100 C at 10 C/min. Includes two melts and one cooling curve.

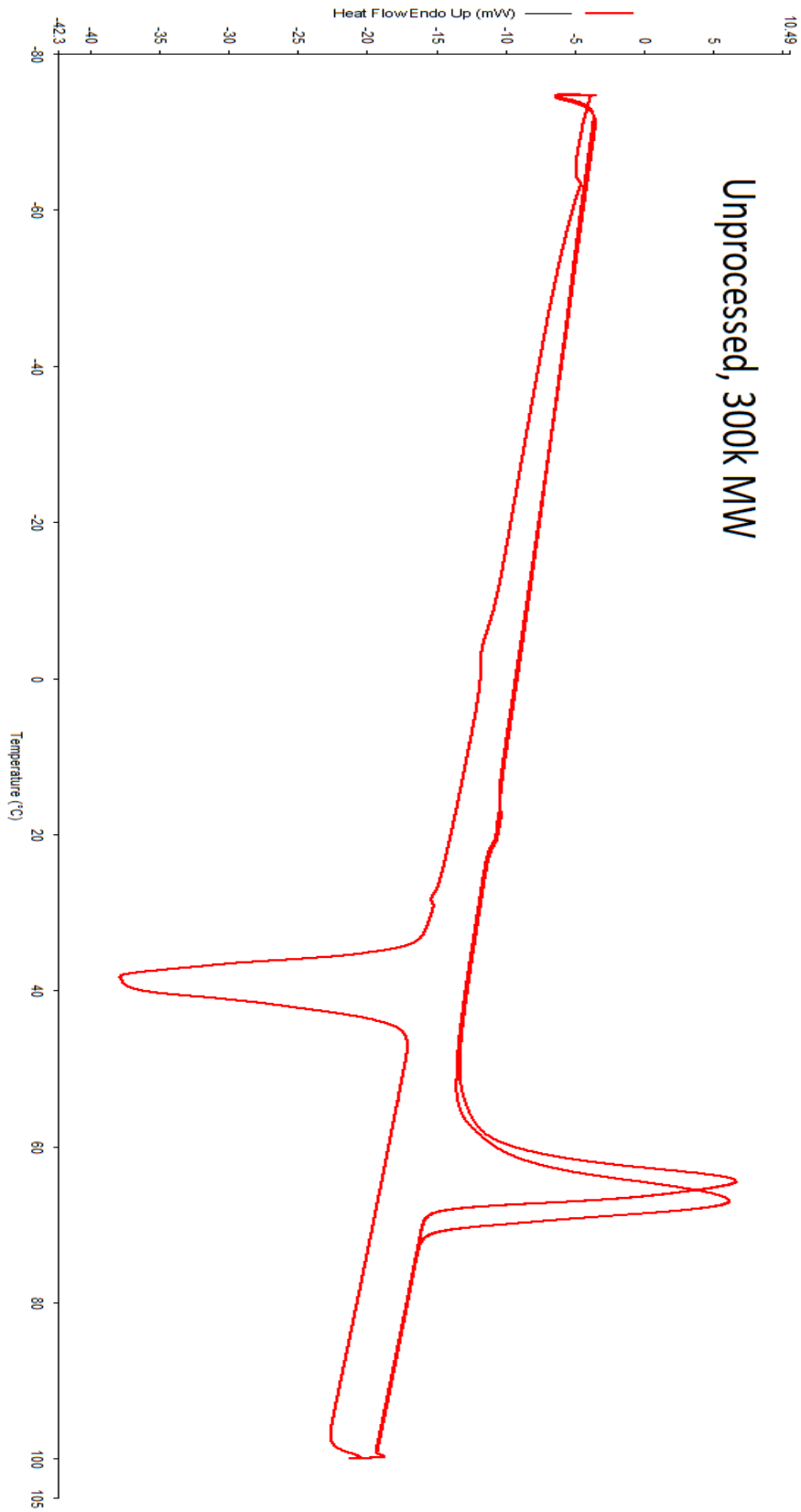

Figure 43. Untreated sample (0 psi) DSC run from -75 C to 100 C at 10 C/min. Includes two melts and one cooling curve.

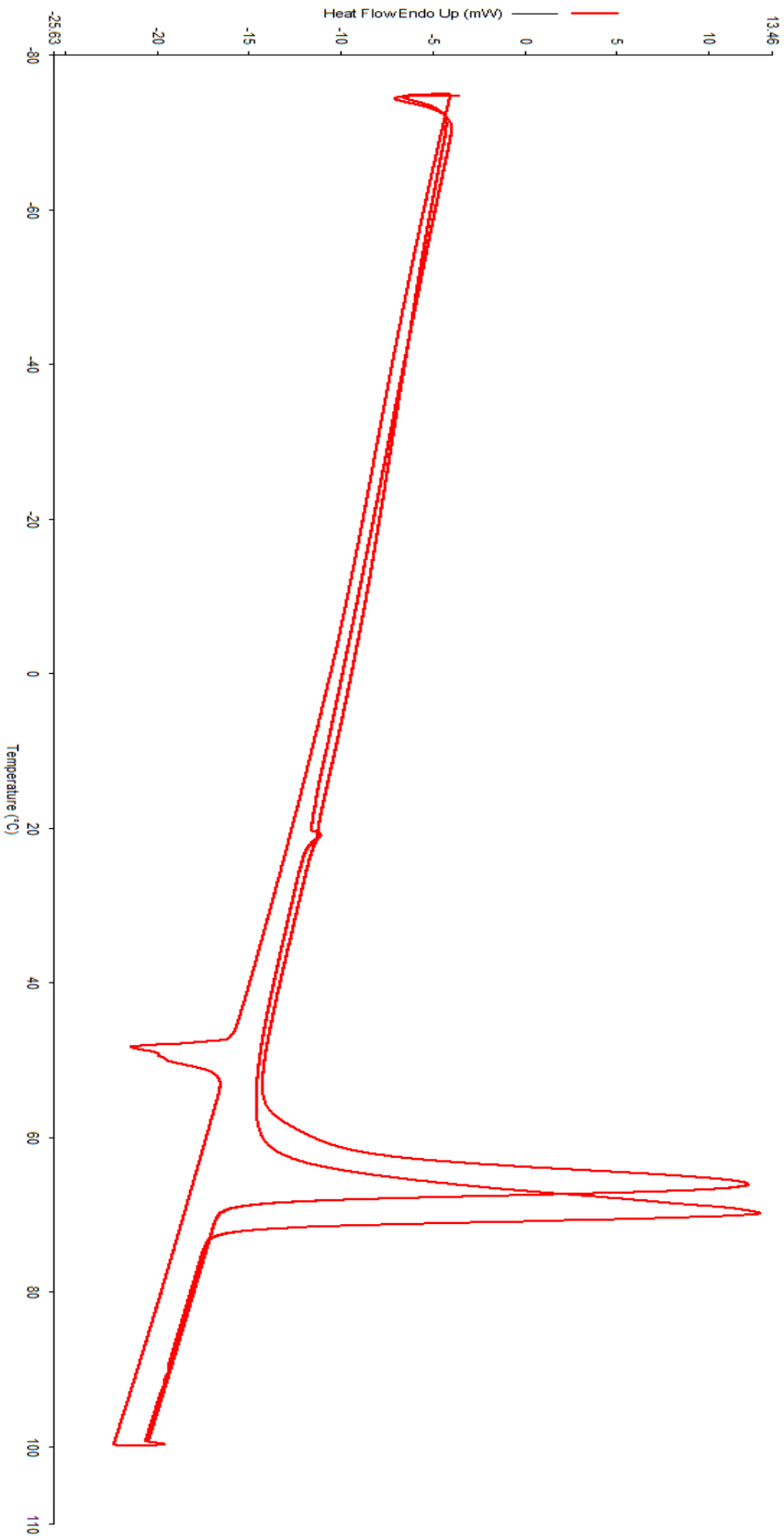

Figure 44. 15000 lbf sample (9779 psi) DSC run from -75 C to 100 C at 1 C/min. Includes two melts and one cooling curve.

Appendix C: X-ray Diffraction

Non-Hot Stage XRD Analysis

Below are tables of non-hot stage deconvoluted peaks for each sample by temperature and region. Values given are 2theta values for the XRD spectra. Bold values are the two major peaks, corresponding to the (120) and (032) crystalline planes.

For table 12, blank values are 2theta values where no peak was found during deconvolution.

Table 12. Non-hot stage XRD deconvolution peak 2theta values.

Control	25 C Center	25 C Outer	52 C	57 C	62 C
13.5	13.5	13.6	13.7	13.6	13.8
14.7	15	15	15	14.7	14.9
15.1				15.2	15.3
19.1	**19.3**	**19.3**	**19.3**	**19.3**	**19.4**
21.1		21.3	21.4	21.2	21.3
22.1				22.2	22.3
23.3	**23.4**	**23.4**	**23.5**	**23.4**	**23.5**
26.2	26.4	26.4	26.4	26.3	26.4
26.9	27.2	27.2	27.1	27.1	27.3
27.8					28
30.1	31.1	31.1	31.1	31.1	31.1
32.6	32.8	32.8	32.8	32.8	32.8
34.2					34.5
35.44	35.5	35.7	35.7	35.6	35.6
36.13	36.4	36.4	36.3	36.3	36.4
39.7	39.9	39.9	39.8	39.8	39.9
41.2					41.5
43	43.1	43.1	43.1	43.1	43.1
45.1	45.3	45.3	45.2	45.3	45.3
47.2		48.9		48.9	49
48.8					
49.8	50.1	50.1		50	50.1
53.5					
54.3					
55.5					
57.2					

Table 13. XRD analysis parameters for non-hot stage samples, calculated using deconvolutions.

	Control	25 C Center	52 C	57 C	62 C
R^2	0.99579	0.99727	0.99840	0.99615	0.99772
Peak 1	4374.53	3448.98	4593.27	2575.21	6577.84
Peak 2	4900.89	4049.14	3018.89	2399.25	2285.07
Ratio	0.8925991	0.85178087	1.52151	1.07334	2.878616
DOC	0.224155	0.218165	0.21597	0.151266	0.218147

The following figures are visual representations of the deconvolution process for each sample. Each figure has two graphs. The upper graph is composed of the raw data (green), deconvolution peaks (red), and the composite deconvolution spectrum (yellow). The lower graph represents the error between the composite deconvolution spectrum and the raw data. The distance between the green line and the white line represents the error (further being less accurate). Most error came from the main crystalline peaks, possibly due to their intensity.

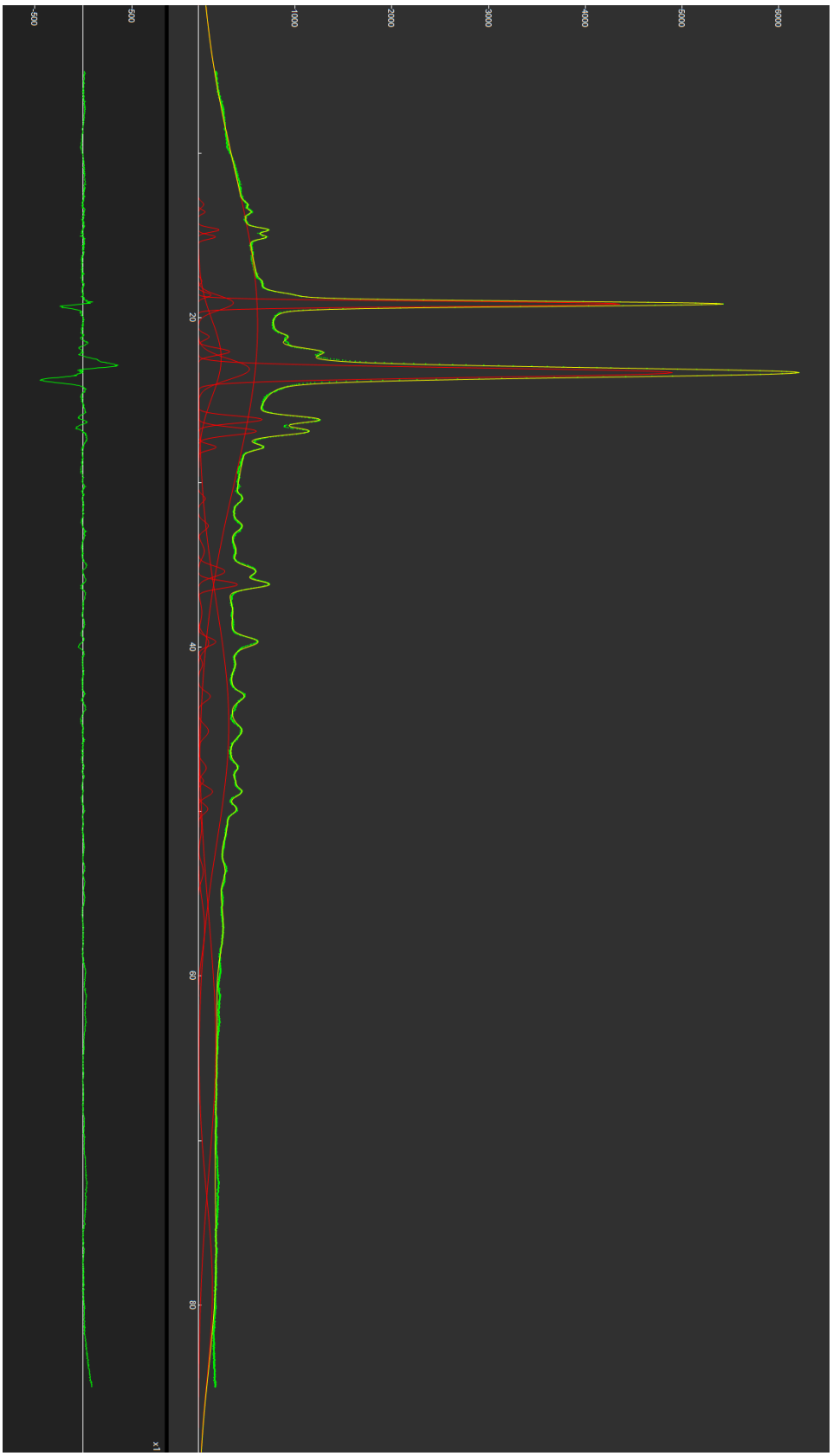

Figure 45. Control (unprocessed) XRD spectrum deconvolution.

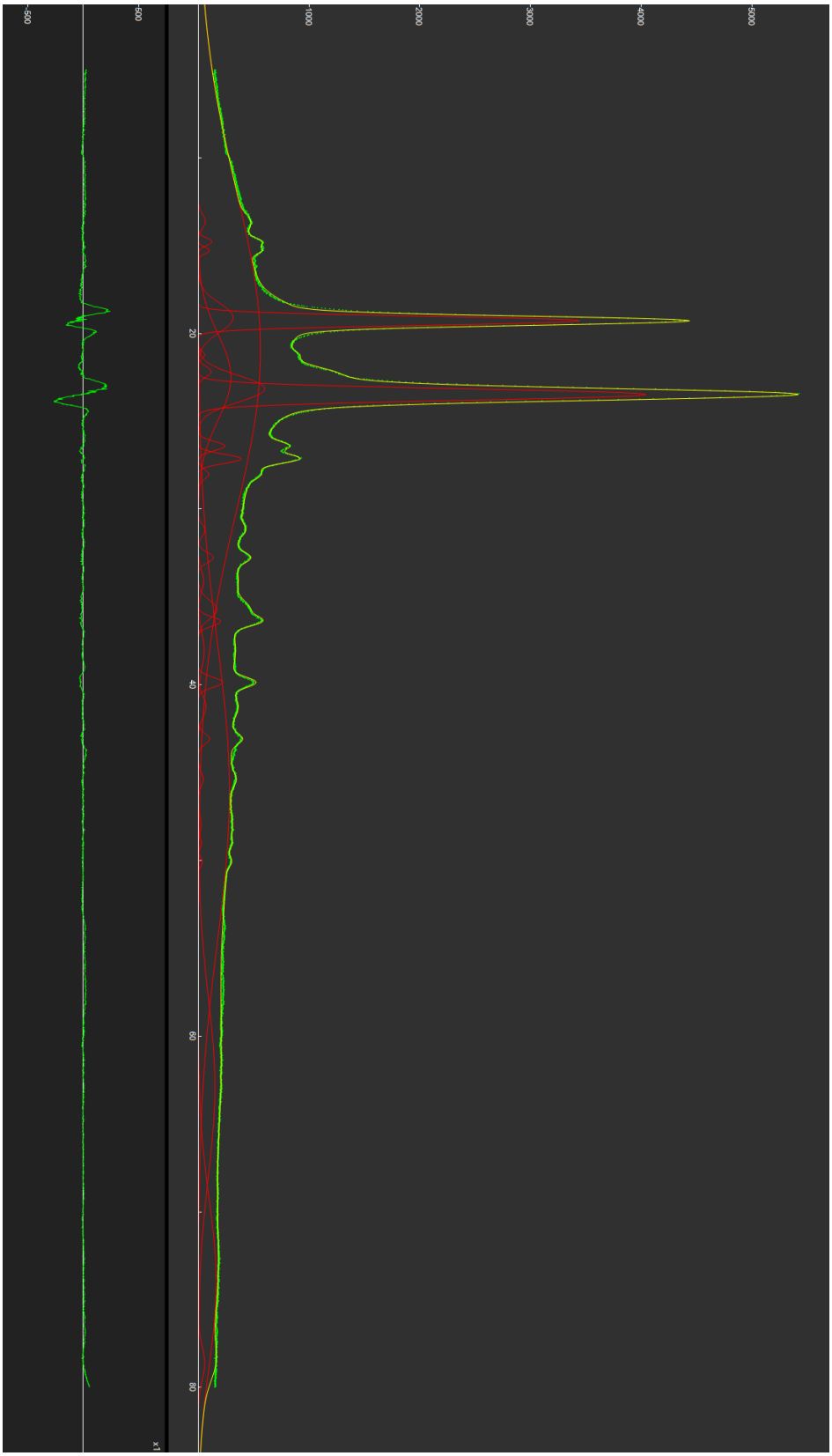

Figure 46. 25 C, 20k lb_f center region XRD deconvolution.

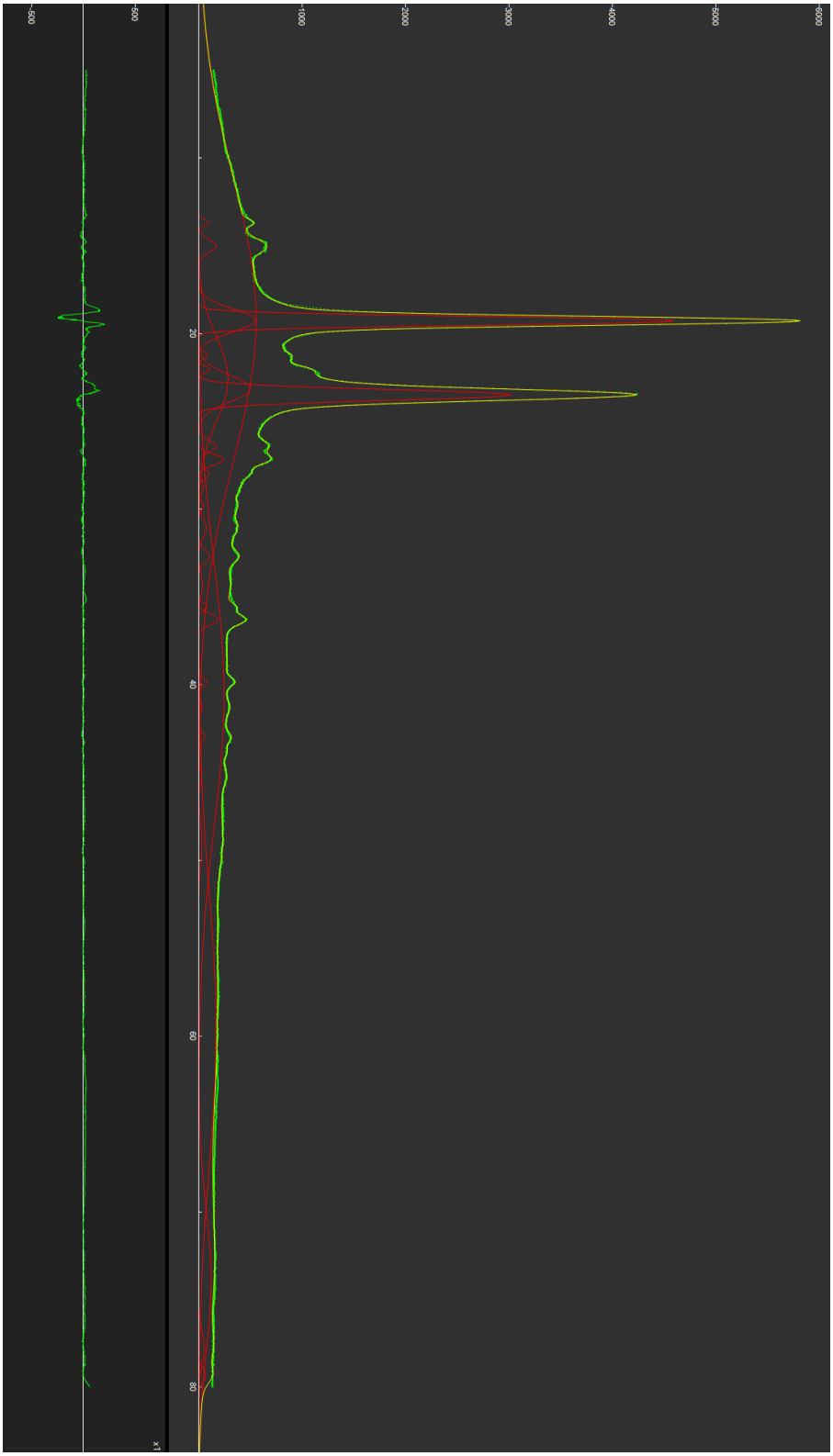

Figure 47. 52 C, 20k lb_f sample XRD deconvolution.

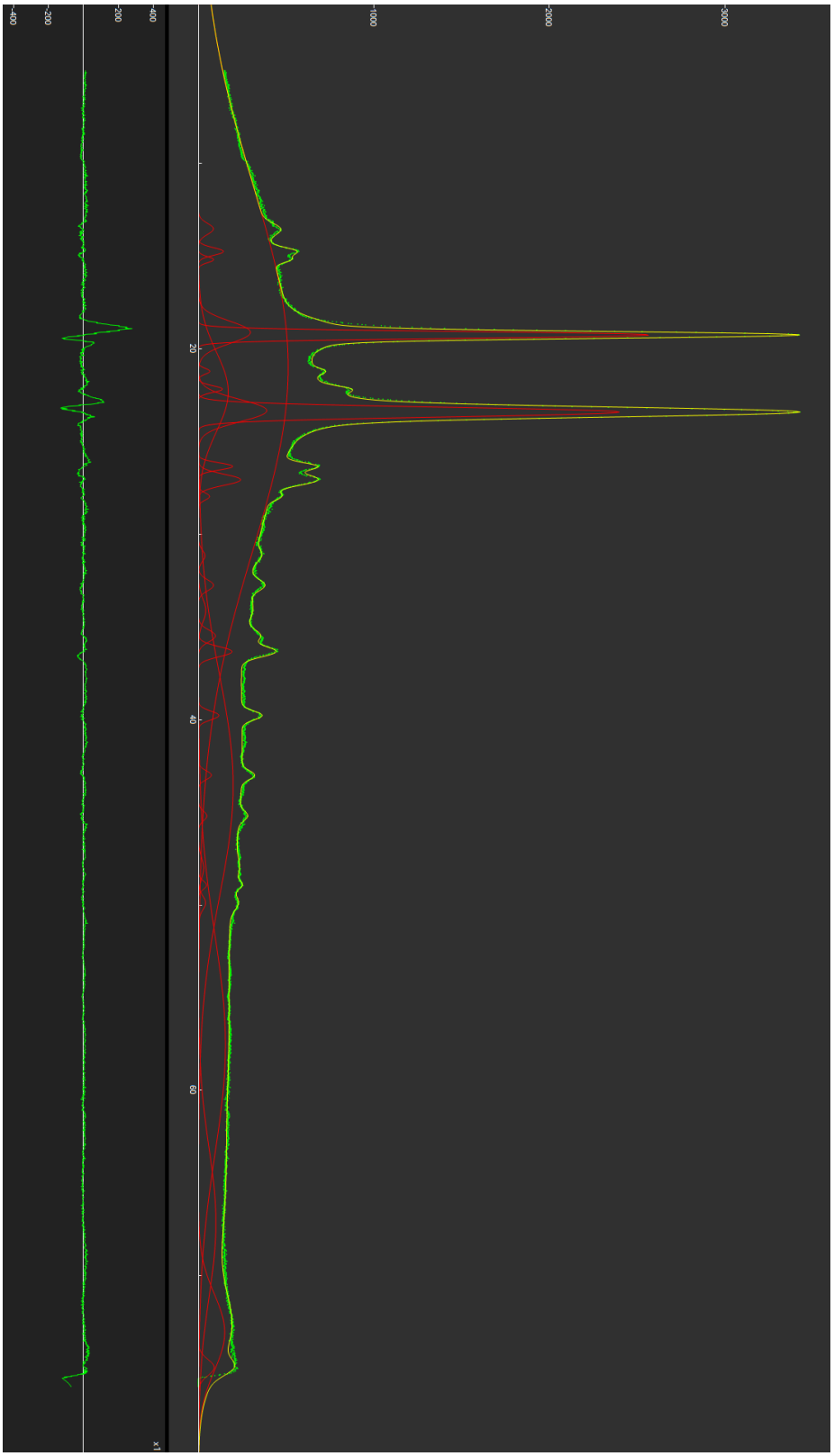

Figure 48. 57 C, 20k lb_f sample XRD deconvolution.

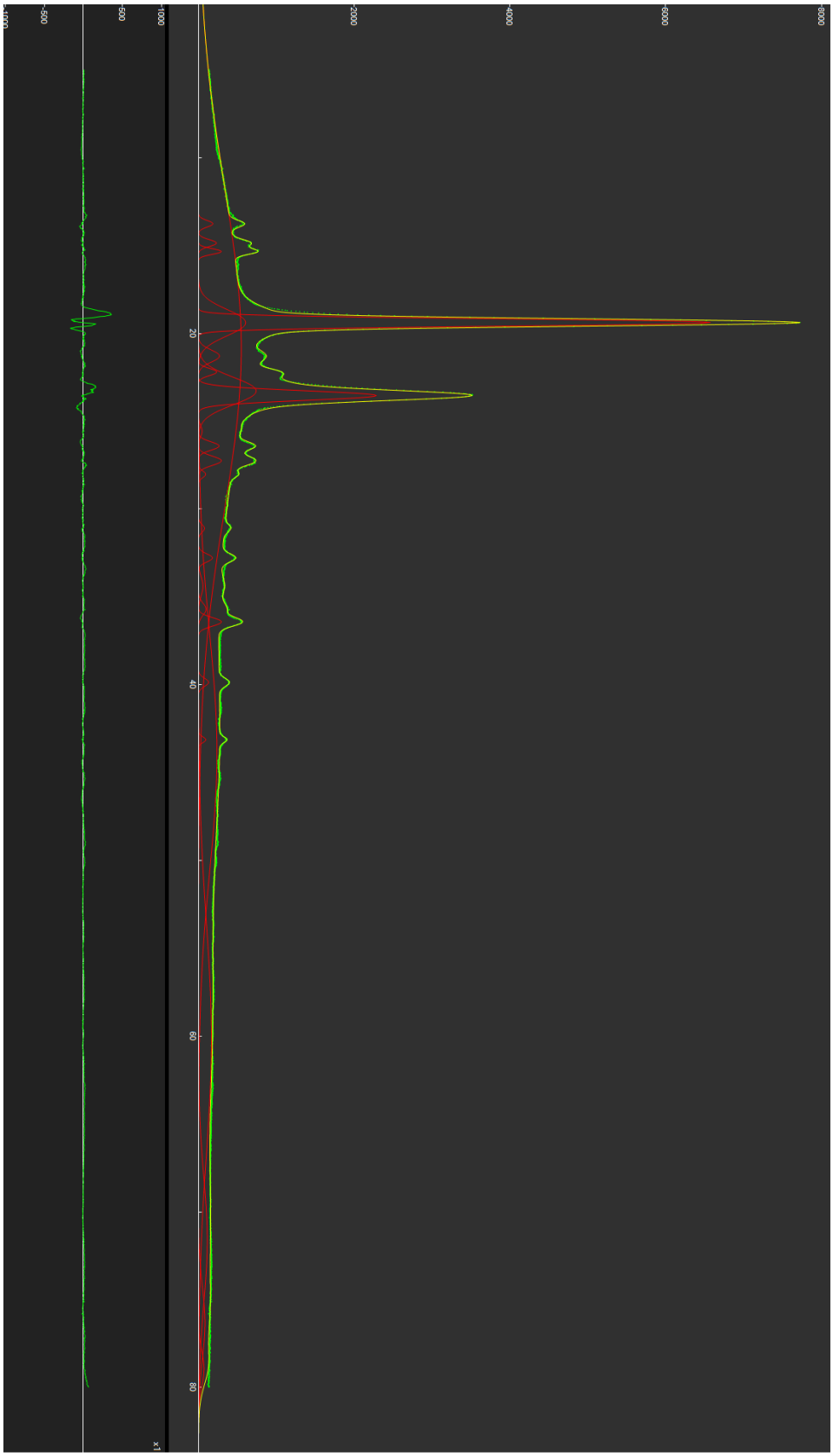

Figure 49. 62 C, 20k lb_f sample XRD deconvolution.

Hot Stage XRD Analysis

Below are tables depicting XRD deconvolution peaks and analytical parameters for three sets of samples: untreated control samples, samples processed at 25 C and 20k lb_f, and samples processed at 55 C and 20k lb_f.

For tables 14, 16, and 18, blank values are 2theta values for which no peak was found during deconvolution.

Table 14. Hot stage XRD deconvolution peak 2theta values for untreated samples. 75 C samples showed no crystalline peaks.

25 C Untreated	45 C Untreated	55 C Untreated	65 C Untreated
13.2	13.3	13.2	13.2
14.5	14.5	14.5	14.5
15	15	15	15
19.1	**19**	**19**	**19**
21.2	21.1	21.1	21
22	22	22	22
23.3	**23.2**	**23.2**	**23.1**
26.2	26.1	26.1	26.1
26.9	26.8	26.8	26.7
27.7	27.7	27.7	27.7
30.8	30.8	30.7	30.7
32.6	32.6	32.7	32.6
35.3	35.2	35.2	35.1
36.1	36.1	36.1	36
39.6	39.6	39.5	39.6
42.9	42.9	42.8	42.9
45	45	44.9	44.9
47.3	47.2	47.2	47.1
48.7	48.7	48.6	48.6
49.8	49.8	49.7	49.7
53.5	53.3	53.3	53.3
	54.2		54

Table 15. Hot stage XRD analytical parameters for untreated samples. 75 C samples showed no crystalline peaks for analysis.

	25 C Untreated	45 C Untreated	55 C Untreated	65 C Untreated
R^2	0.99587	0.99534	0.99278	0.99581
Peak 1	3541.23	3491.19	3454.99	3330.42
Peak 2	3647.21	3647.86	3569.62	3360.23
Ratio	0.97094217	0.957052	0.967887	0.991129
FWHM 1	0.36	0.38	0.36	0.34
FWHM 2	0.72	0.78	0.76	0.74
DOC	0.291303	0.285	0.267699	0.245106

Table 16. Hot stage XRD deconvolution peak 2theta values for samples processed at 25 C and 20k lb_f. 75 C samples showed no crystalline peaks.

25 C	45 C	55 C	65 C
13.4	13.4	13.2	13.4
14.5	14.5	14.5	14.5
14.9	15	14.9	15
19	**19**	**19**	**19**
21	21	20.9	21
		22	22
23.2	**23.1**	**23.1**	**23.2**
26.1	26.1	26.1	26.1
26.8	26.8	26.8	26.8
27.7	27.7	27.7	27.8
30.8	30.8	30.7	30.7
32.6	32.5	32.5	32.6
35.2	35.2	35.2	35.2
36.1	36	36.1	36
39.6	39.5	39.5	39.6
42.8	42.8	42.8	42.9
45.1	45.1	45.1	45
47.2	47.2		47.2
48	47.9		48
48.7	48.7	48.7	48.7
49.8	49.8	49.8	49.8
	53.6	53.6	53.4
			54.1

Table 17. Hot stage XRD analytical parameters for samples processed at 25 C and 20k lb_f. 75 C samples showed no crystalline peaks for analysis.

	25 C RT	45 C RT	55 C RT	65 C RT
R^2	0.99772	0.99808	0.99802	0.99784
Peak 1	1356.75	1368.25	1412.55	1688.2
Peak 2	1588.51	1560.4	1596.68	1885.26
Ratio	0.85410227	0.876858	0.884679	0.895473
FWHM 1	0.44	0.46	0.46	0.4
FWHM 2	0.8	0.74	0.74	0.72
DOC	0.184013	0.192823	0.170922	0.172534

Table 18. Hot stage XRD deconvolution peak 2theta values for samples processed at 55 C and 20k lb_f.

45 C	55 C	65 C	75 C
13.4	13.4	13.4	
14.5	14.5	14.5	
15	14.9	15	14.9
19	**19**	**18.9**	**19**
21	20.9	21	20.8
22	21.9	21.9	22
23.1	**23.1**	**23.1**	**23.1**
26.1	26.1	26.1	
			26.3
26.9	26.9	26.9	
27.7	27.7	27.6	
30.7	30.6	30.6	
32.5	32.4	32.5	
35.2	35.2	35.2	35
36	36	36	36.2
39.5	39.5	39.5	
40.9	41	41	
42.8	42.8	42.8	
45	45	45	
47.1			
48.6	48.6		
49.8	49.7	49.7	

Table 19. Hot stage XRD analytical parameters for samples processed at 55 C and 20k lb_f.

	25 C	45 C	55 C	65 C	75 C
Peak 1	1563.1	1547.28	1539.69	1526.88	619.569
Peak 2	1615.32	1609.95	1585.91	1529.29	479.178
Ratio	0.96767204	0.961073	0.970856	0.998424	1.292983
FWHM 1	0.36	0.38	0.38	0.38	0.36
FWHM 2	0.66	0.66	0.66	0.66	0.72
DOC	0.15243	0.1972	0.142338	0.133262	0.064022

The following figures are visual representations of the deconvolution process for each hot stage sample. Each figure has two graphs. The upper graph is composed of the raw data (green), deconvolution peaks (red), and the composite deconvolution spectrum (yellow). The lower graph represents the error between the composite deconvolution spectrum and the raw data. The distance between the green line and the white line represents the error (further being less accurate). Most error came from the main crystalline peaks, possibly due to their intensity.

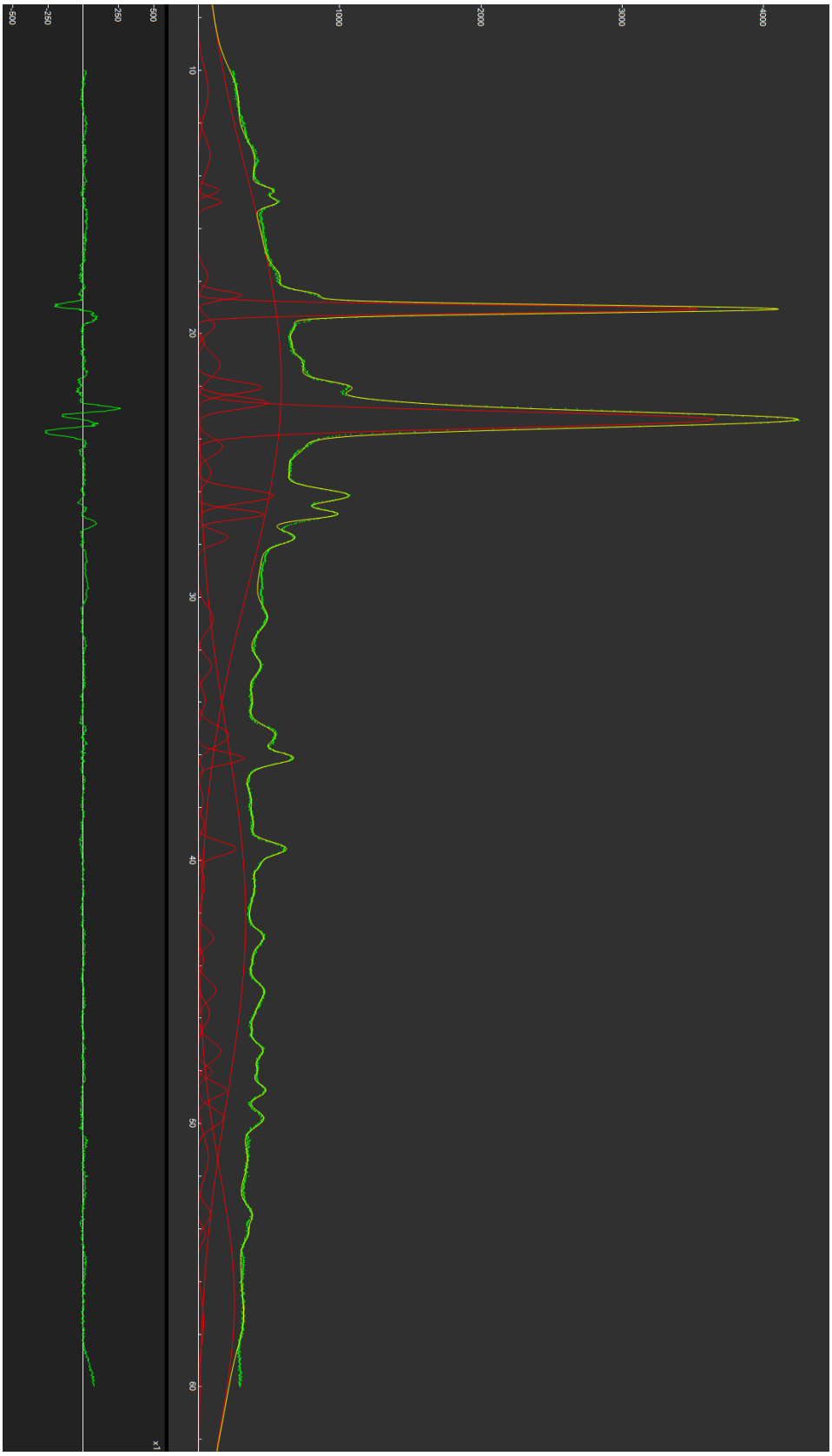

Figure 50. XRD deconvolution of hot stage sample: untreated control at 25 C.

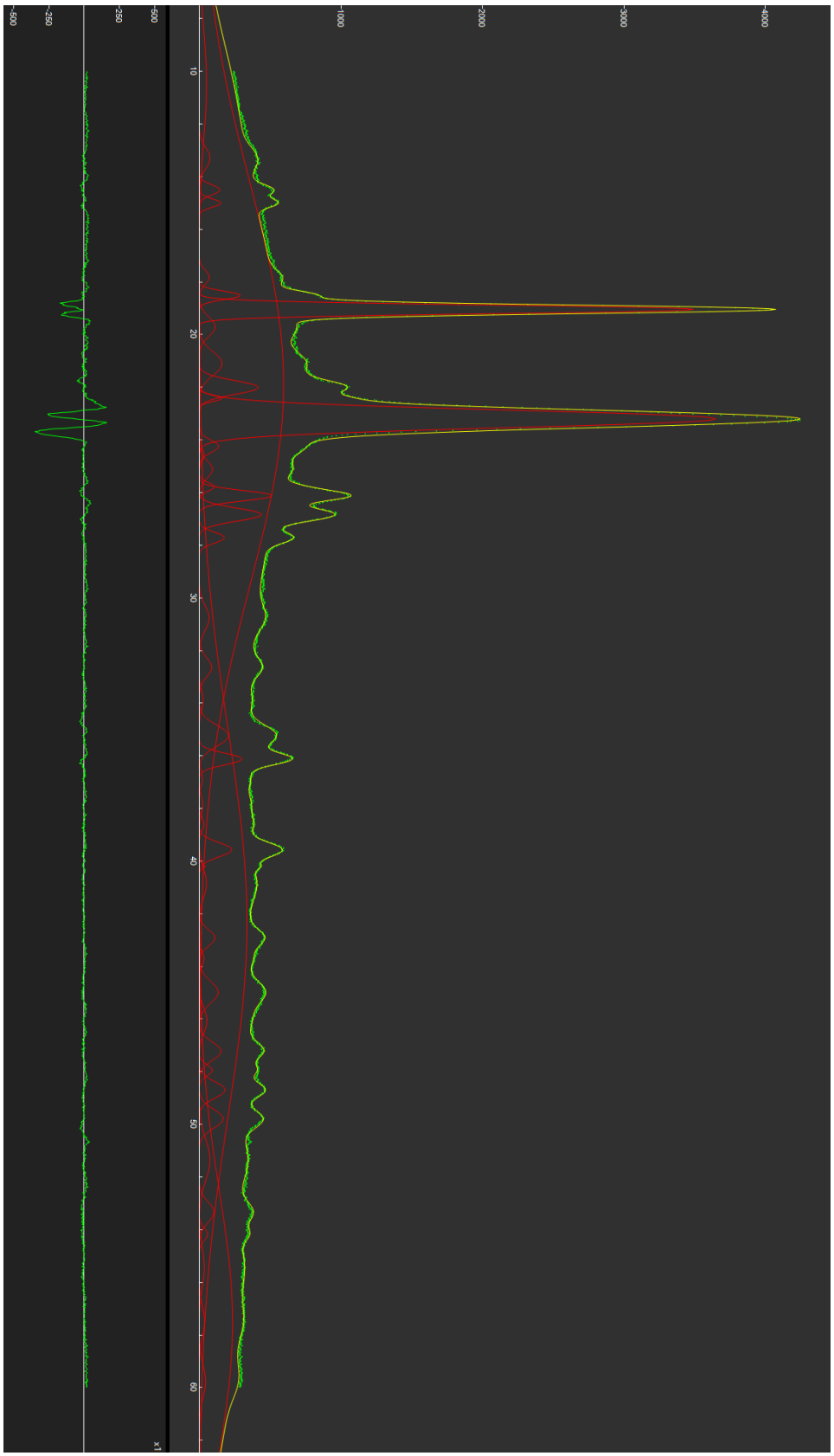

Figure 51. XRD deconvolution of hot stage sample: untreated control at 45 C.

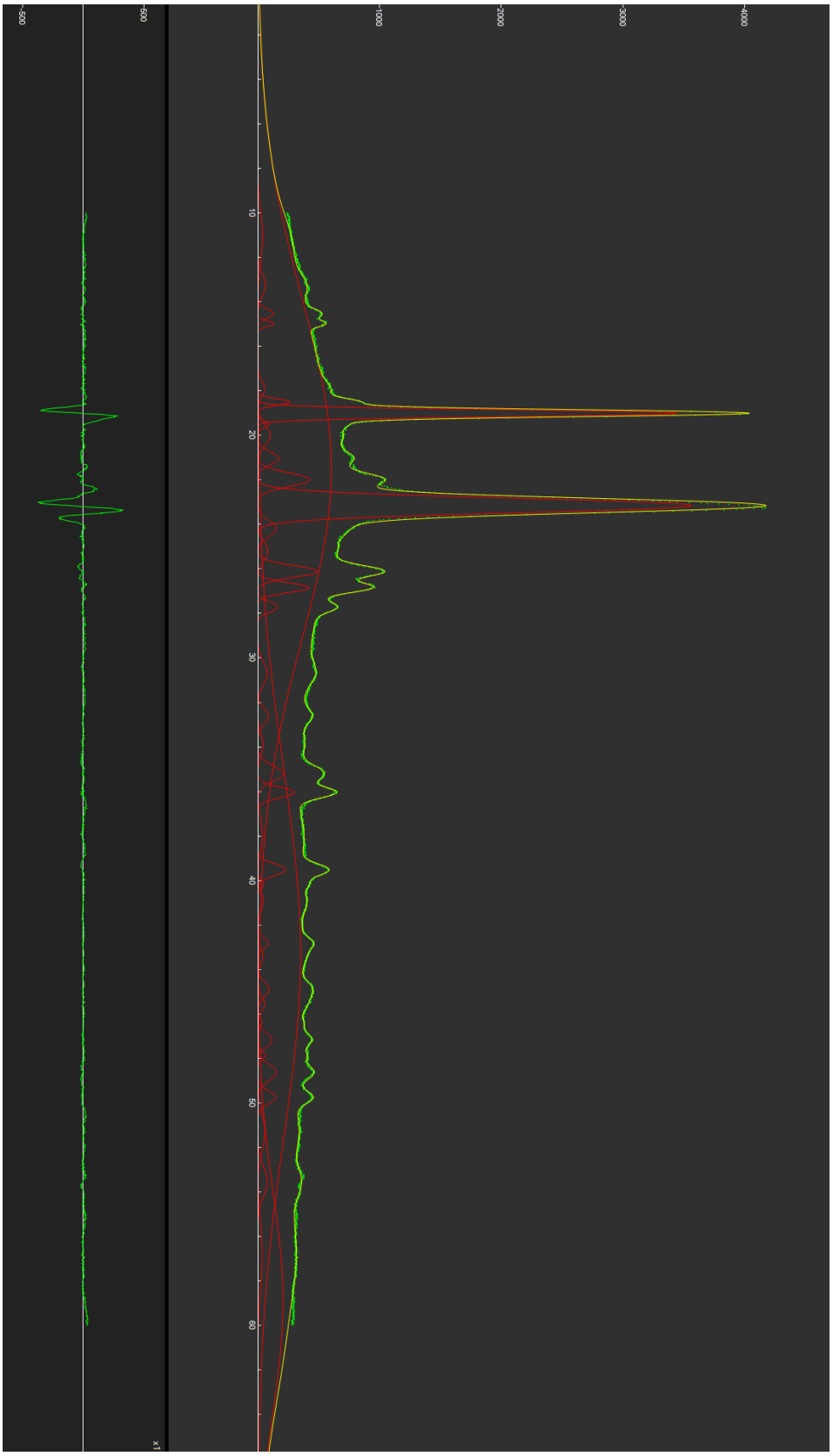

Figure 52. XRD deconvolution of hot stage sample: untreated control at 55 C.

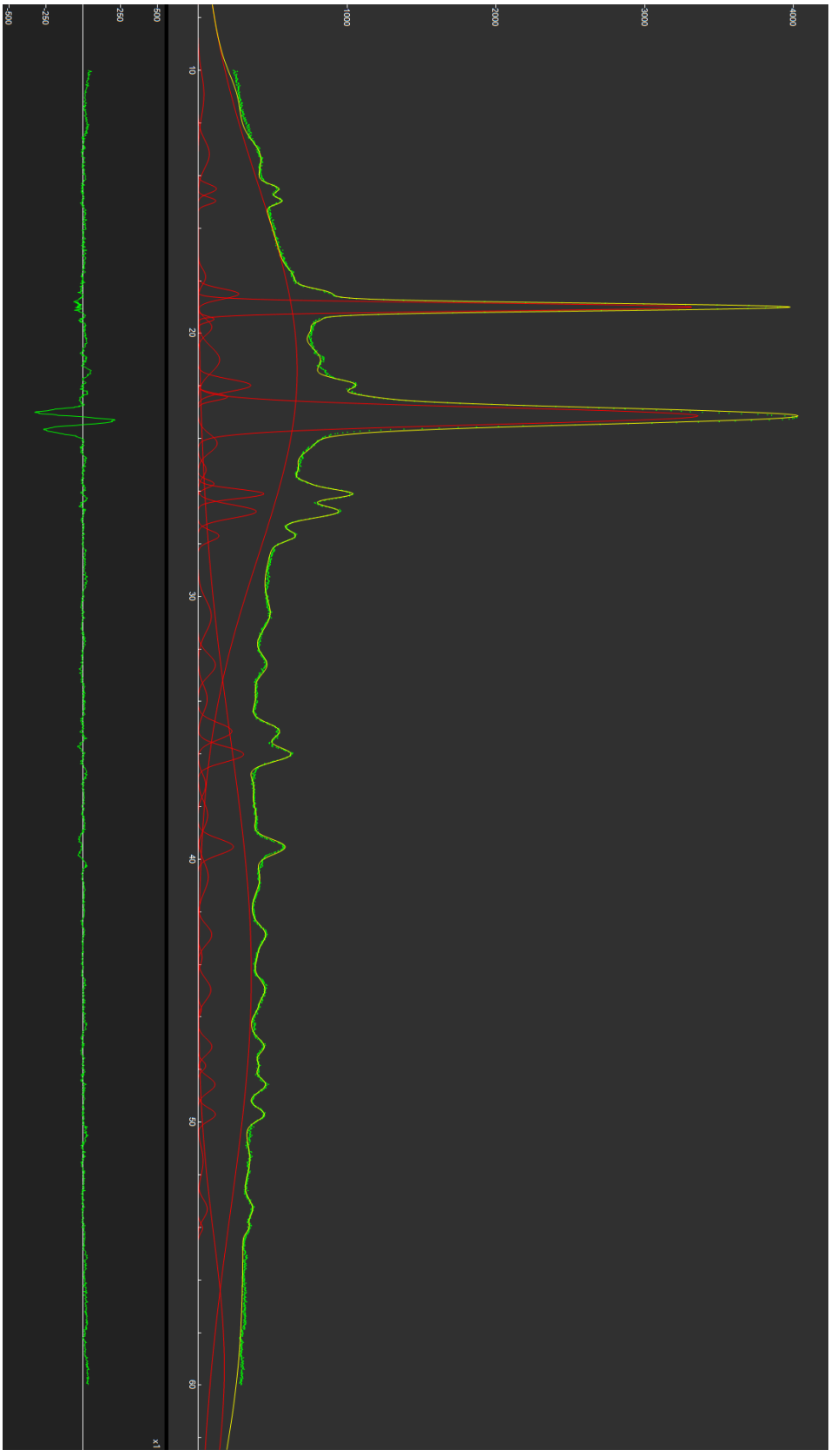

Figure 53. XRD deconvolution of hot stage sample: untreated control at 65 C.

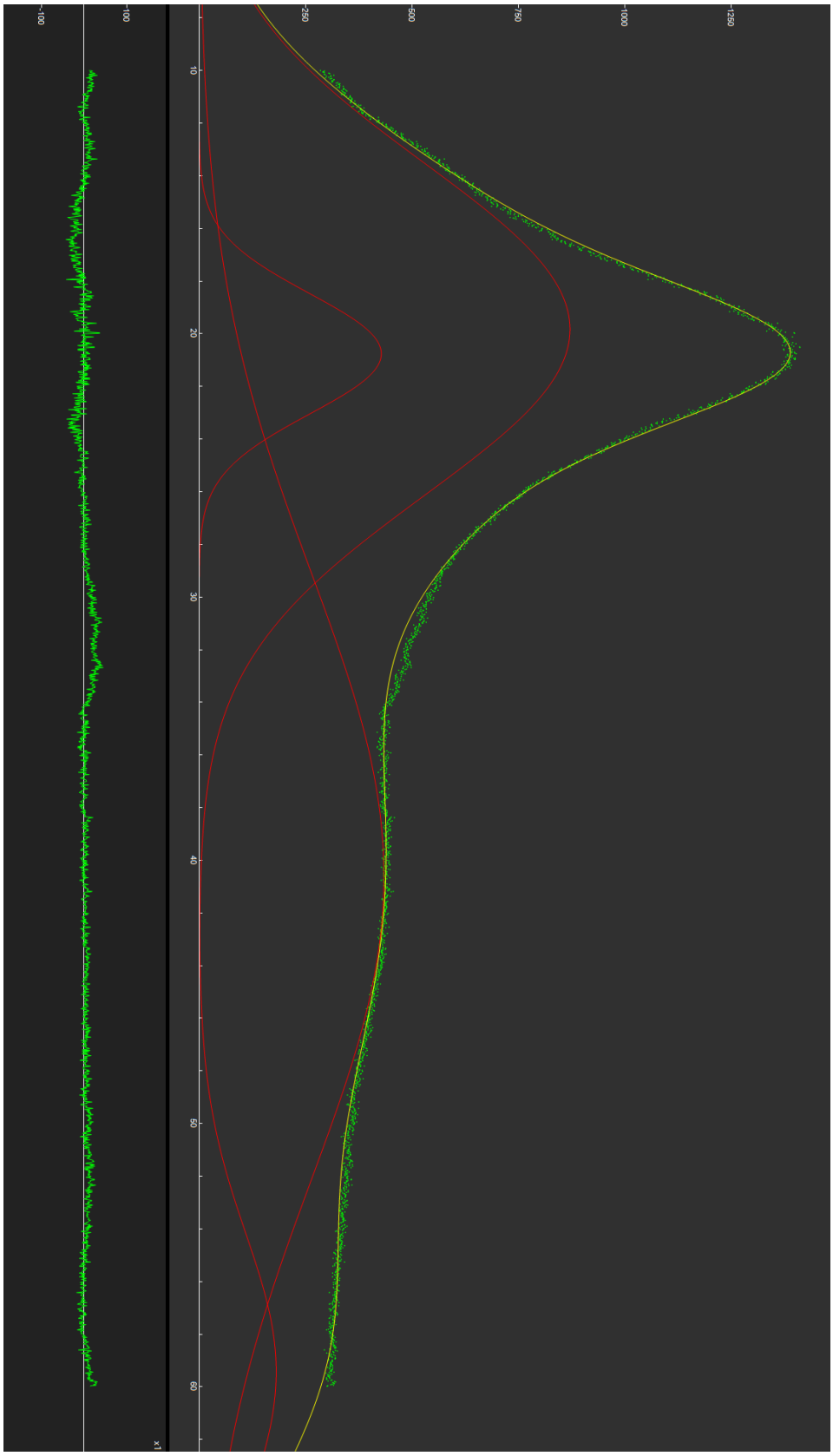

Figure 54. XRD deconvolution of hot stage sample: untreated control at 75 C.

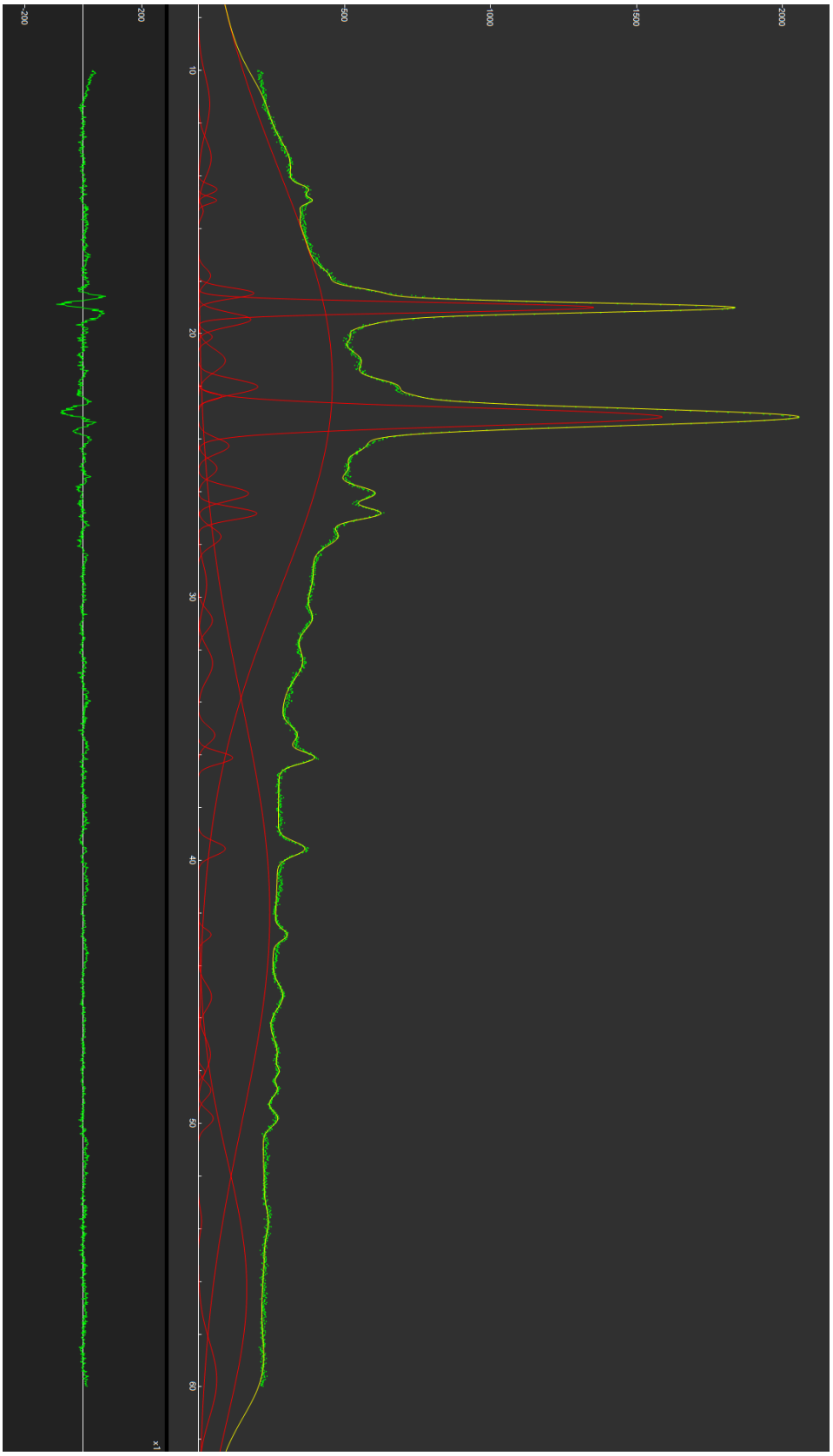

Figure 55. XRD deconvolution of hot stage sample: sample processed at 25 C and 20k lb_f, run at 25 C.

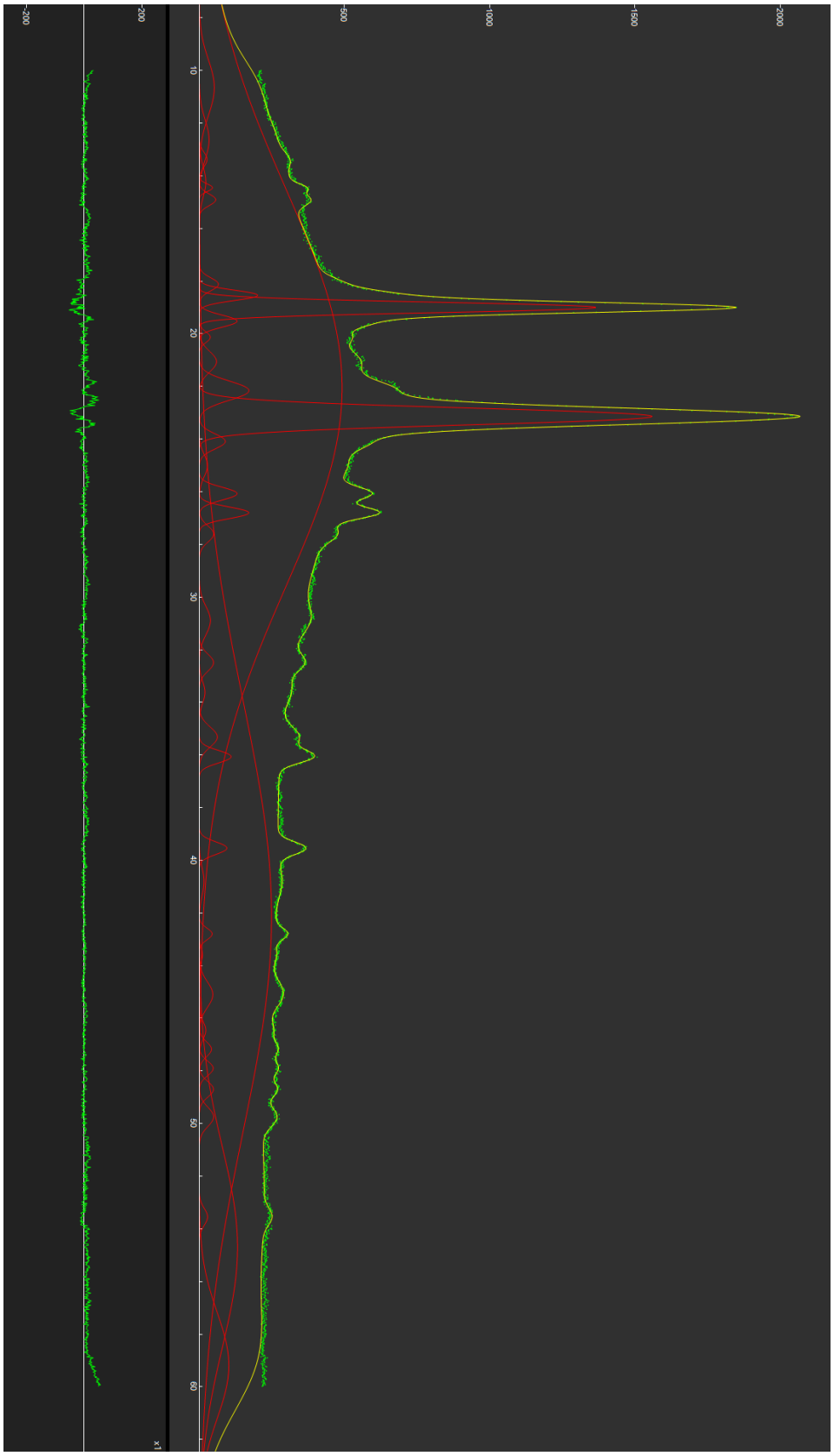

Figure 56. XRD deconvolution of hot stage sample: sample processed at 25 C and 20k lb_f, run at 45 C.

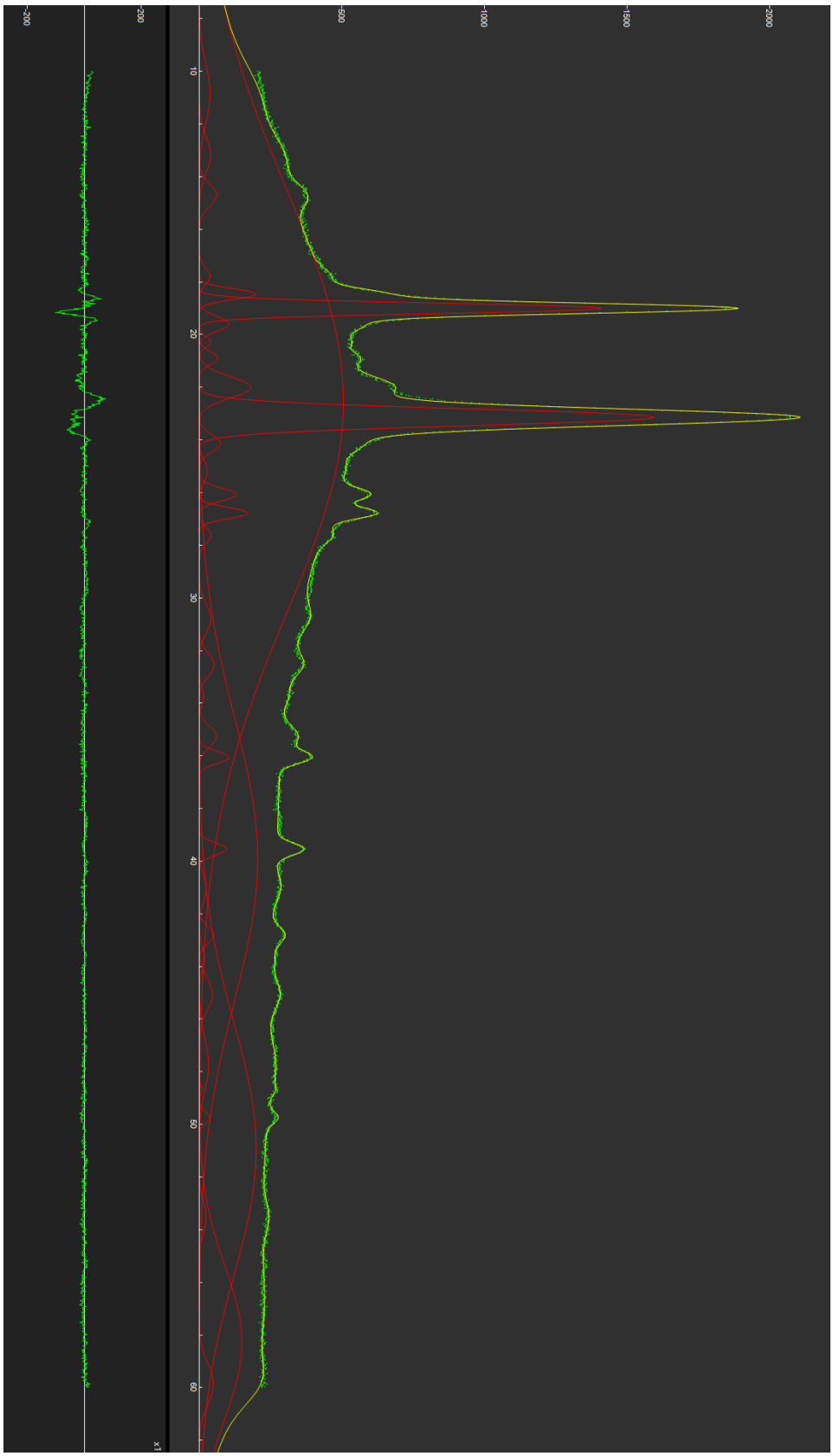

Figure 57. XRD deconvolution of hot stage sample: sample processed at 25 C and 20k lb_f, run at 55 C.

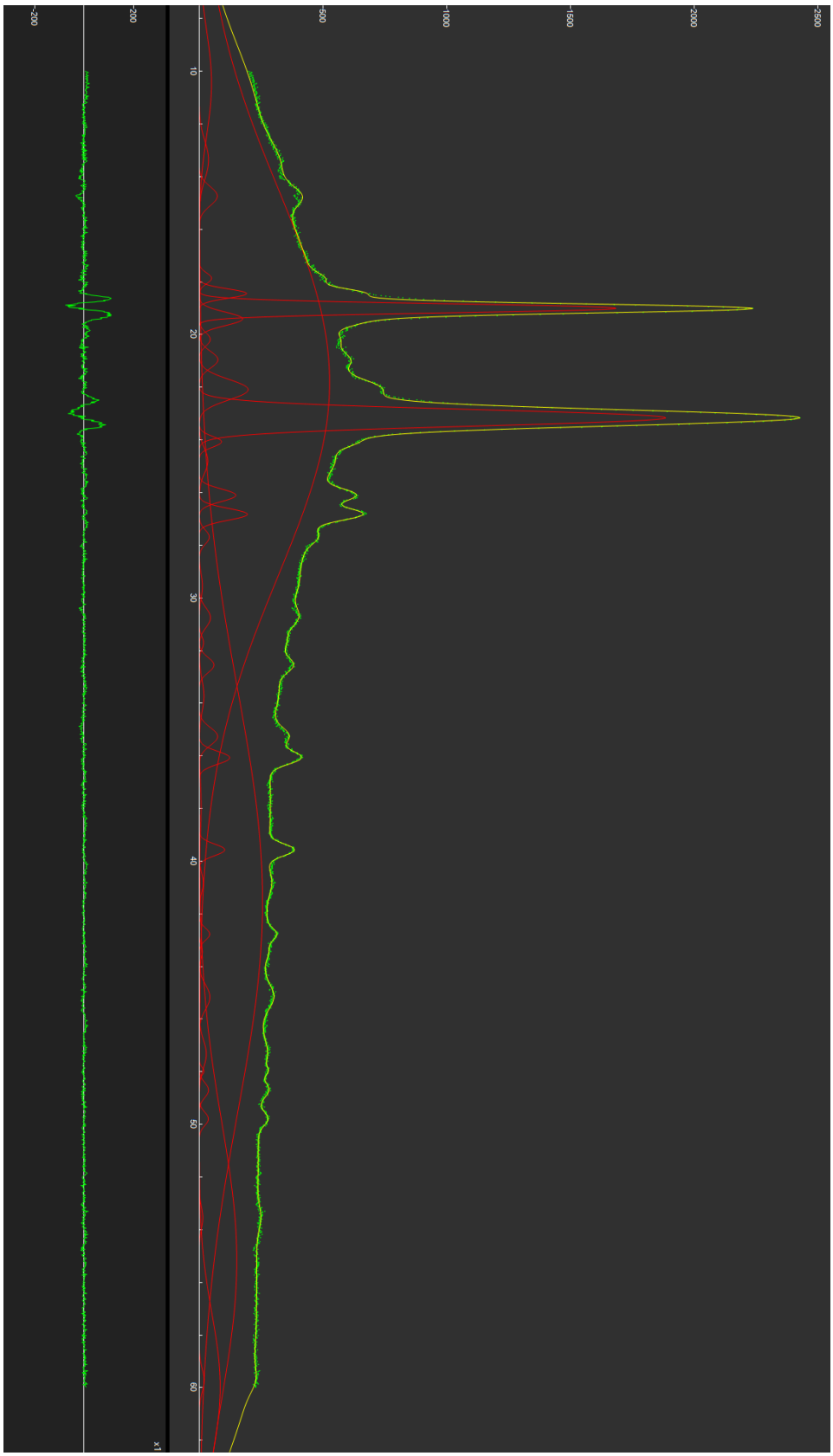

Figure 58. XRD deconvolution of hot stage sample: sample processed at 25 C and 20k lb_f, run at 65 C.

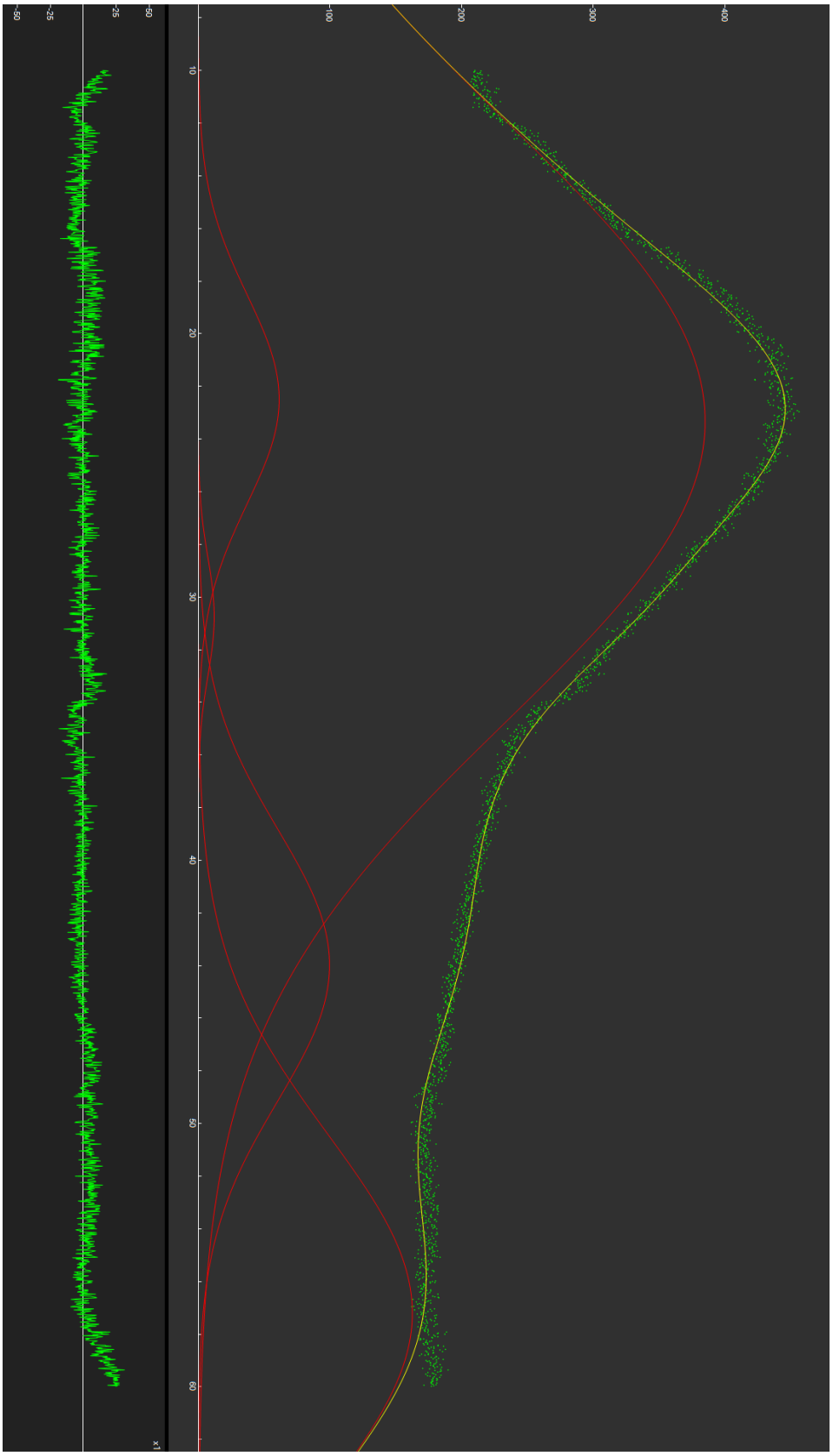

Figure 59. XRD deconvolution of hot stage sample: sample processed at 25 C and 20k lb_f, run at 75 C.

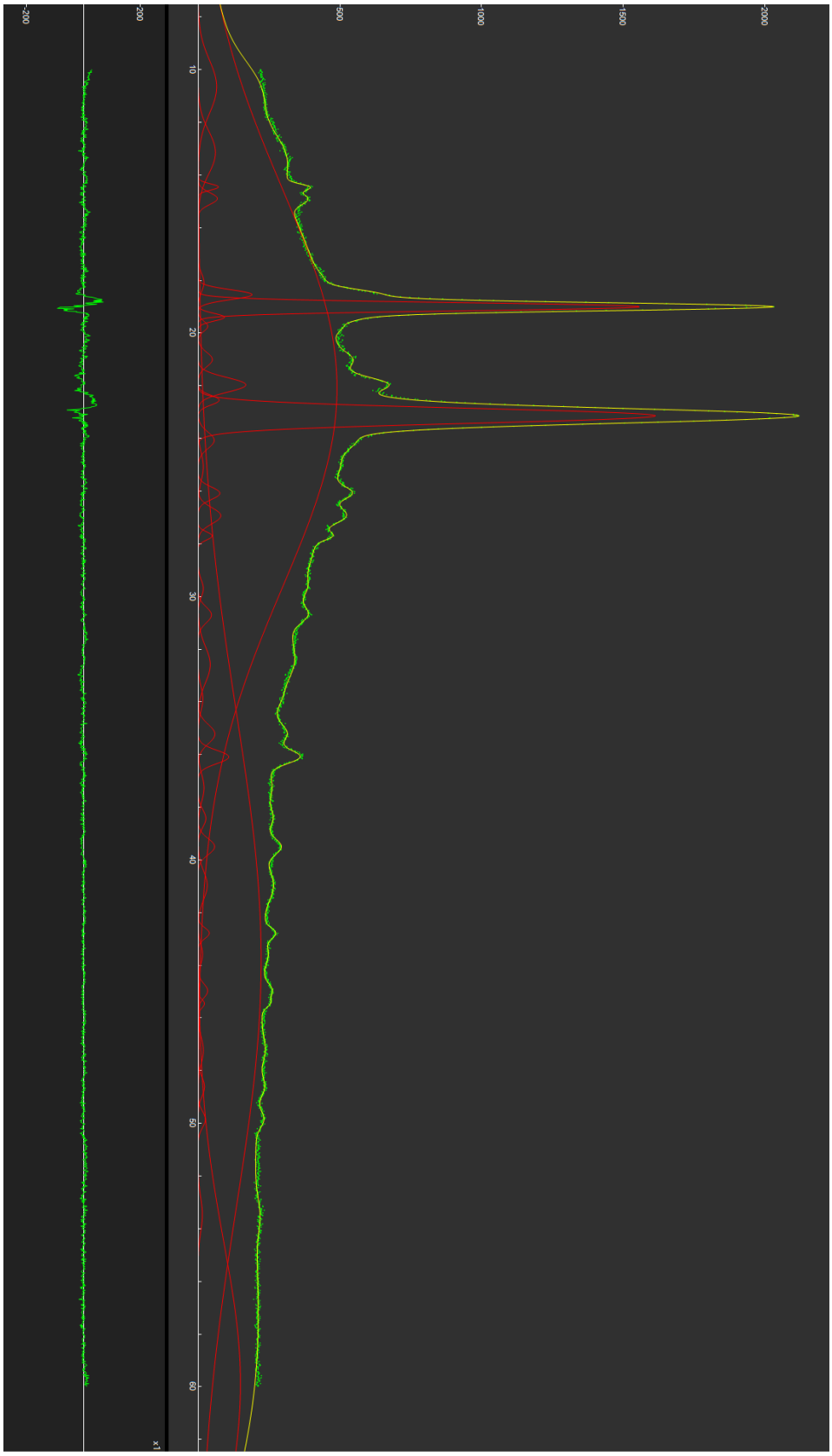

Figure 60. XRD deconvolution of hot stage sample: sample processed at 55 C and 20k lb_f, run at 25 C.

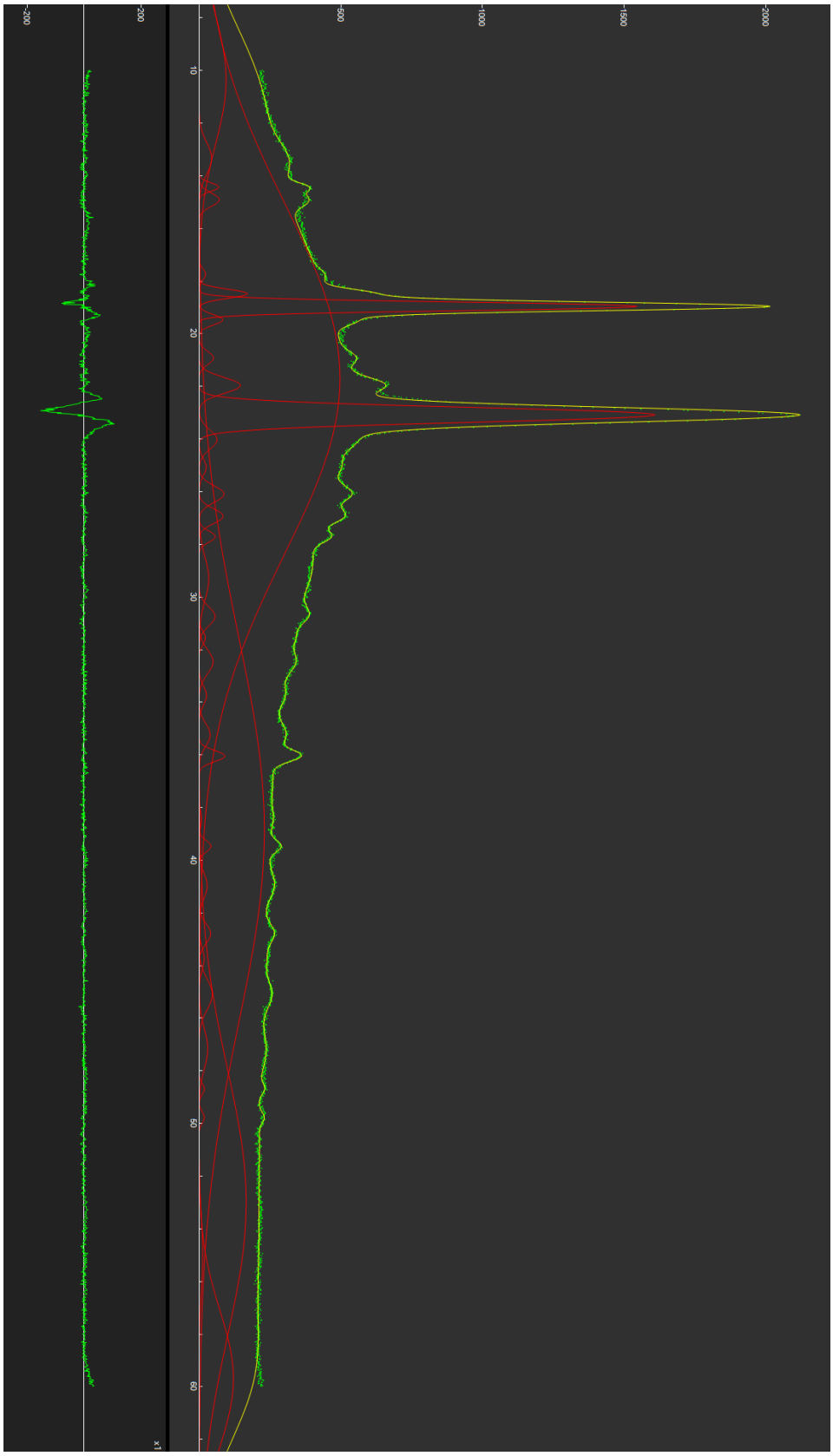

Figure 61. XRD deconvolution of hot stage sample: sample processed at 55 C and 20k lb_f, run at 45 C.

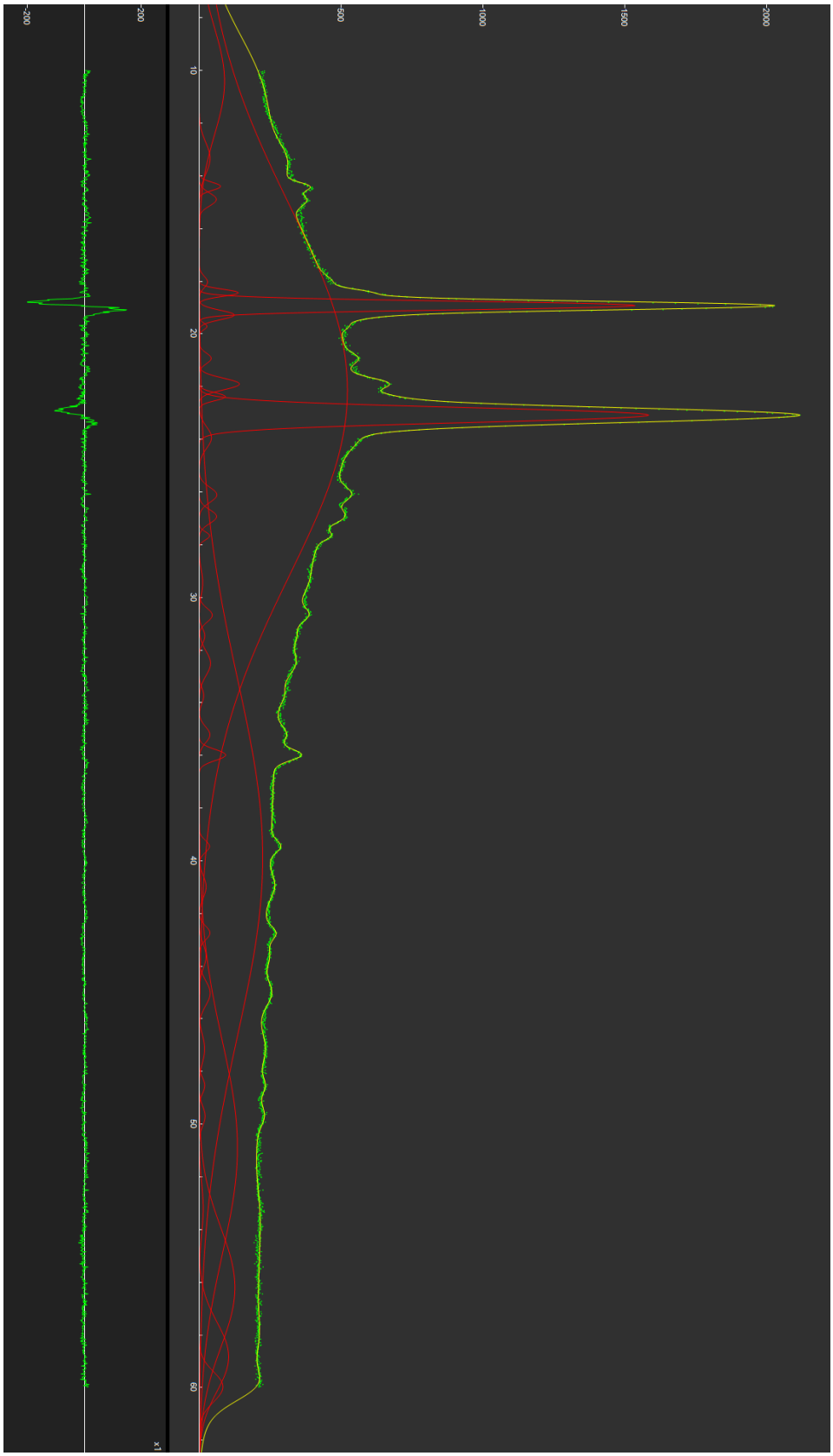

Figure 62. XRD deconvolution of hot stage sample: sample processed at 55 C and 20k lb_f, run at 55 C.

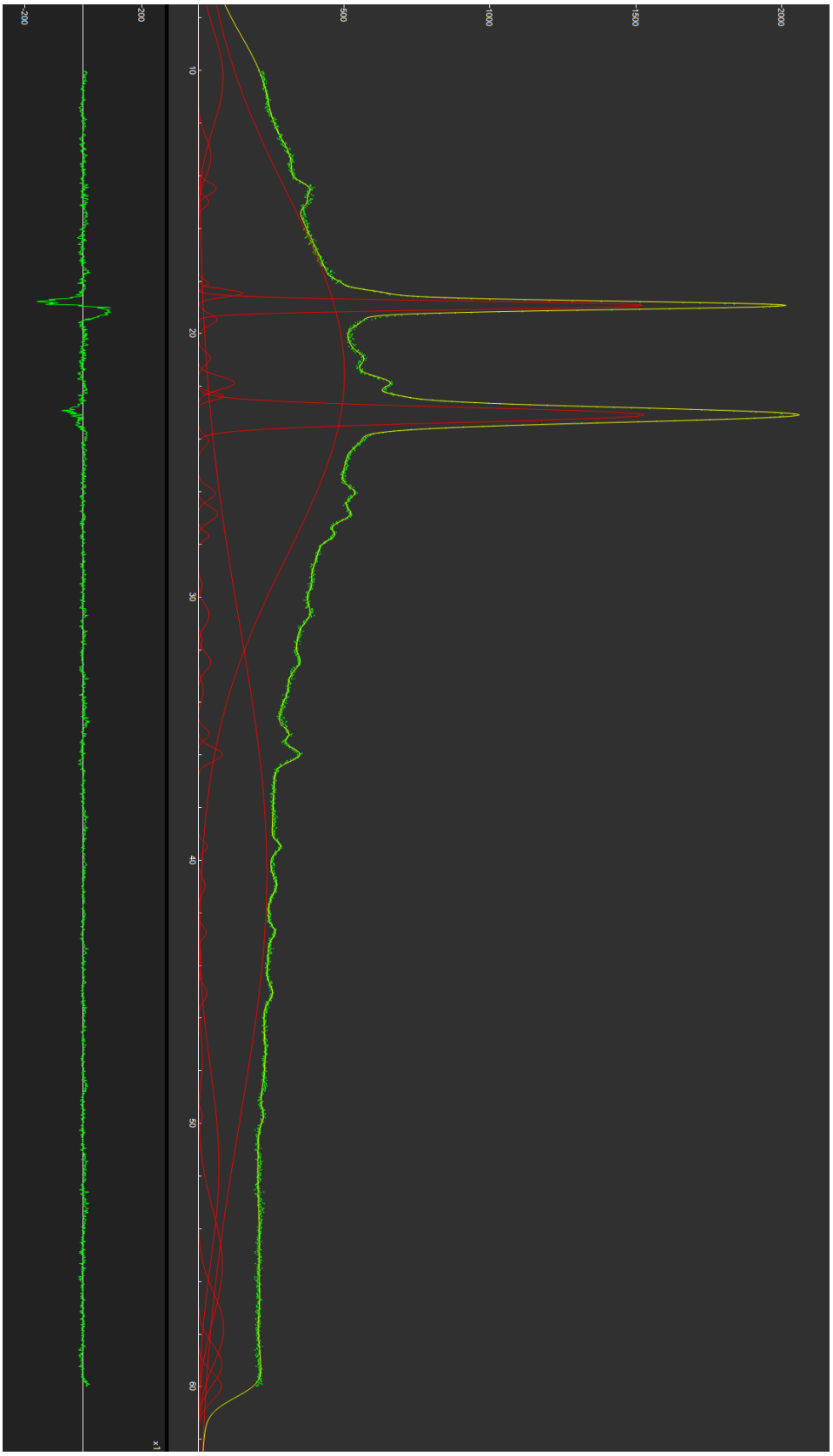

Figure 63. XRD deconvolution of hot stage sample: sample processed at 55 C and 20k lb_f, run at 65 C.

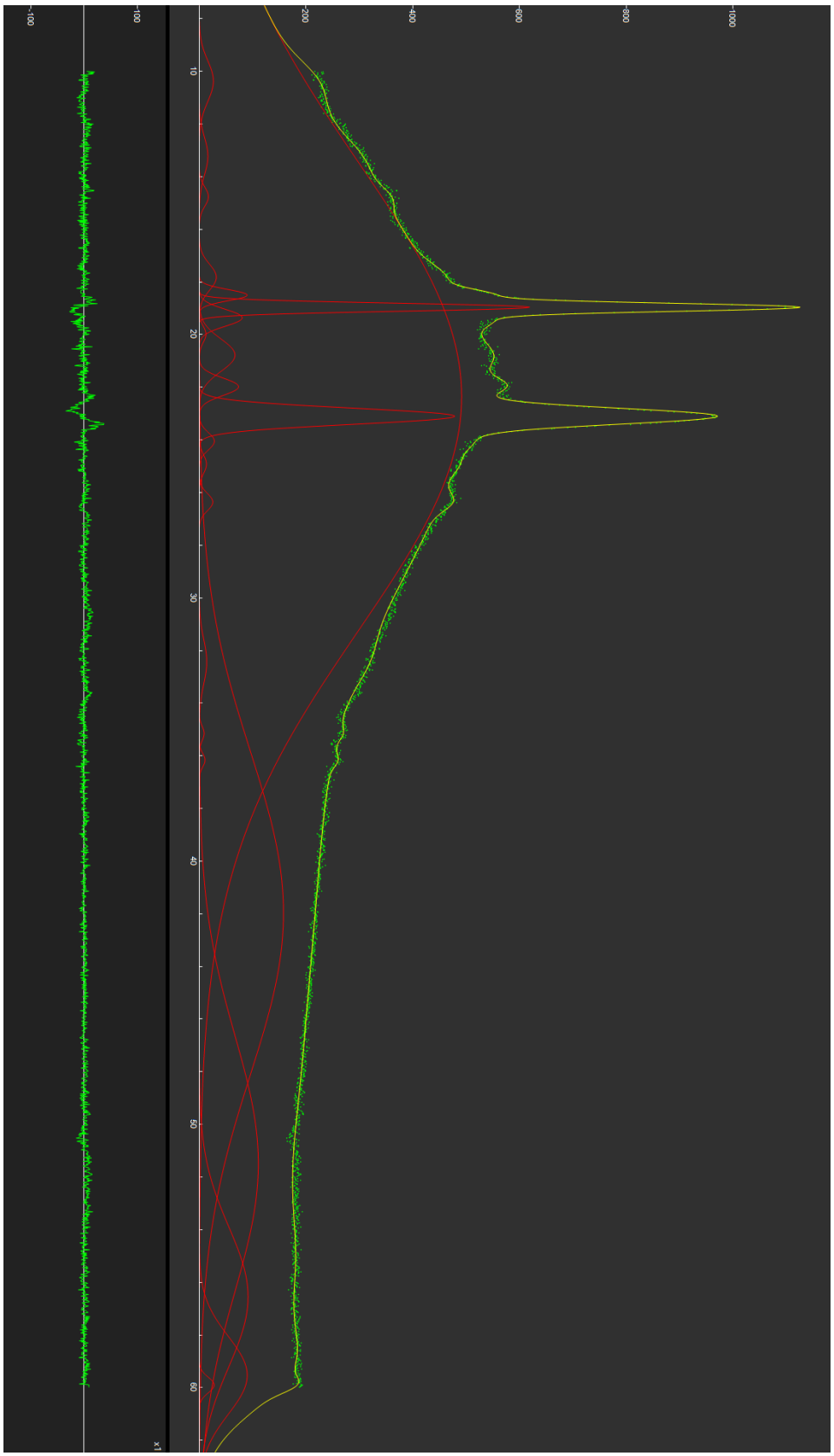

Figure 64. XRD deconvolution of hot stage sample: sample processed at 55 C and 20k lb_f, run at 75 C.

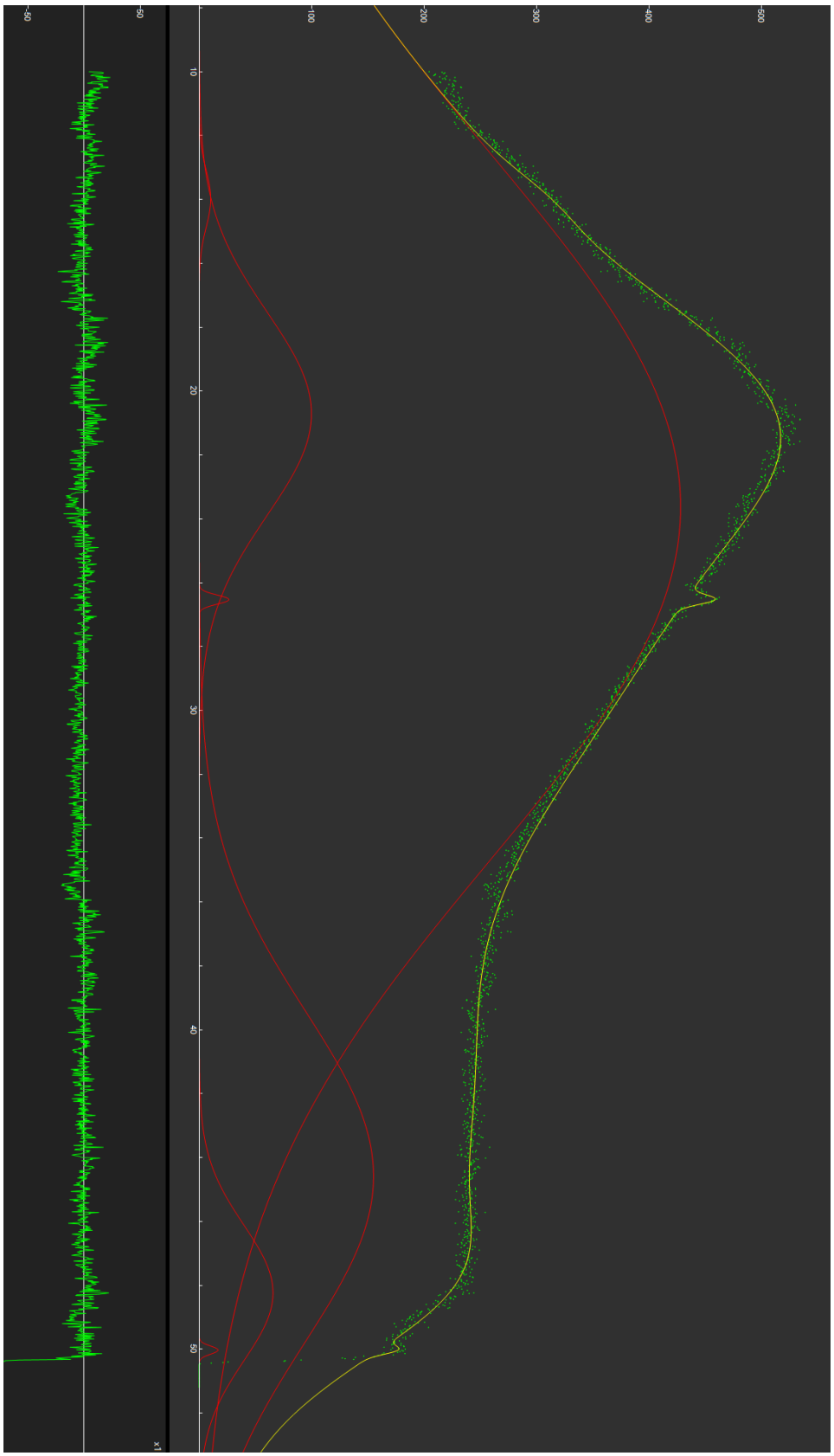

Figure 65. XRD deconvolution of hot stage sample: sample processed at 55 C and 20k lb_f, run at 85 C.